Hybrid perovskite materials : characterization of their electrical properties and stability at the nanoscale

Jaume Llàcer Martínez

Matériaux Pérovskites Hybrides: Caractérisation des Propriétés Électroniques et Stabilité à l'Échelle Nanométrique

Jaume Llàcer Martínez

Thèse soumise pour obtenir le grade de Docteur de l'Université de Lille

Specialité: Électronique, Microélectronique, Nanoélectronique et Micro-ondes

Le jury est composé de:

Prof. Frank Palmino (Femto-ST, Université de Franche-Comté, France), Rapporteur

Dr. Christina Villeneuve-Faure (LAPLACE, Université Paul Sabatier, France), Rapporteur

Prof. Philippe Leclère (University of Mons, Belgique), Directeur de thèse

Dr. Didier Théron (IEMN, CNRS, France), Directeur de thèse

Prof. Michel Voué (University of Mons, Belgique), Examinateur

Prof. Christian Loppacher (IM2NP, Université d'Aix Marseille, France), Examinateur

Prof. Roberto Lazzaroni (University of Mons, Belgique), Invité

Prof. Rony Snyders (University of Mons, Belgique), Invité

Dr. Sophie Barrau (UMET, Université de Lille, France), Invité

Thèse soutenue le 14 Decembre 2020

Hybrid Perovskite Materials: Characterization of their Electrical Properties and Stability at the Nanoscale

Jaume Llàcer Martínez

A dissertation submitted to the Doctoral School: Sciences pour l'Ingenieur

for the degree of

Doctor of the University of Lille

Speciality: Electronics, Microelectronics, Nanoelectronics and Microwaves

Examination Committee:

Prof. Frank Palmino (Femto-ST, Université de Franche-Comté, France), Referee

Dr. Christina Villeneuve-Faure (LAPLACE, Université Paul Sabatier, France), Referee

Prof. Philippe Leclère (University of Mons, Belgium), Promotor

Dr. Didier Théron (IEMN, CNRS, France), Promotor

Prof. Michel Voué (University of Mons, Belgium), Examiner

Prof. Christian Loppacher (IM2NP, Université d'Aix Marseille, France), Examiner

Prof. Roberto Lazzaroni (University of Mons, Belgium), Invited

Prof. Rony Snyders (University of Mons, Belgium), Invited

Dr. Sophie Barrau (UMET, Université de Lille, France), Invited

December 2020

Prologue

This thesis was carried out in a cotutelle between the University of Mons (Belgium) and the University of Lille (France). At the University of Mons, I was part of the *Laboratory for Chemistry of Novel Materials (CMN)*. CMN is a research group focused mainly on modelling, synthesis and characterization of organic materials used for energy applications. The CMN is also founding the Materia Nova Research Center, located in Mons (Belgium). Materia Nova conducts a number of projects directed towards the industry and it allows the CMN department to extend their research activities. I had the opportunity to use the facilities from Materia Nova to synthesize and characterize the perovskite materials, which require an inert environment (usually a N_2-filled glovebox) to work with. On the other side, in France I was working at the *Institut d'Électronique, de Microélectronique et de Nanotechnologie (IEMN)*, located in Villeneuve d'Ascq (France). The IEMN is a research institute working in close collaboration with the University of Lille and the CNRS. Their research goes from nanoscience applications to instrumentation. At the IEMN, I had the chance to use their scanning microwave microscope and to test the perovskite samples previously made at Materia Nova.

Acknowledgements

The results presented in this thesis would not be possible without the help and support from the group of brilliant scientists and people I had the fortune to share my PhD journey. I will name some of the people that influenced me the most through these years.

First, I would like to thank Didier Théron and Philippe Leclère for giving me the opportunity to start this PhD. I offer my sincerest gratitude to Didier, for the sheer amount of knowledge you have imparted upon me. I hope I retained at least half of the things you have taught me. A substantial amount of thanks to Roberto Lazzaroni and Philippe, for all of the help and guidance you have provided me in order to accomplish the best results.

To a couple of guys I very much consider as my co-supervisors, Olivier Douhéret and David Moerman. Olivier, I thank you for the profound insights and conversations we had regarding my studies/results along this ever so long journey. I admire the energy you transmit to people on an everyday basis and I thank you for your patience that I have yet to see exhausted. David, to say that everything I know now about AFM is because of you, thanks for your guidance through my experimental work, you provided me with the tools and support I needed to crystallize this thesis. Also, I extend my gratitude to the all the Materia Nova members as well as to Petr Polovodov, who has been very supportive and helped me with lots of SMM measurements, thank you so much.

To Juan A. Anta and to Lidia Contreras Bernal for giving me the opportunity to work with you at the University Pablo de Olavide. Thank you both for your warm welcome in Sevilla and for teaching me about impedance spectroscopy.

To the friendly crew at the CMN department, while it does no justice to single people out, I will at least mention the people I shared priceless moments and/or trips. In no particular order: Pauline, Nadège, Alex, Séb, Max, Laura, Sinan and Fab, thank you all. I would like also to acknowledge some friendships I've made during my stay in Mons: Wouter, Luc and Mule. We've had some unforgettable moments, I will always treasure our time spent discussing about everything, playing squash, cycling and enjoying music. You were a strong support to me, I would never thank you enough.

To Paula C., doing a PhD in a country far from my friends/family is sometimes tough, but things get always easier with people like you, I am in awe of the support you have given me. A special thank you to my friend Joan, for a call when I needed it most. To Paula G., sharing with you the last 2 years of my PhD was like finding an oasis and will always be with me.

To my family, it would never be enough whatever I tell you here. Distance may separate us, but I always felt as if you were right next to me. I reckon with time you will forget what this paragraph meant so, there it goes: *Tot el que soc és gràcies a vosaltres.*

Abstract

Global warming is one of the main concerns in our society nowadays, year after year the impact and consequences are becoming more visible. The Paris agreement set a target to limit the CO_2 emission, which is mainly caused from the increasing demand for energy based on fossil fuels. Since then, the scientific community has increased their efforts on looking for clean energy sources such as renewable energies. In this regard, solar energy is meant to be one of the main energy sources that could replace fossil fuels. Therefore, photovoltaic technologies have evolved tremendously and, organic-inorganic hybrid halide perovskite materials have been one of the technologies with the fastest growth in solar cell performance. Perovskite materials possess unique properties such as flexibility, low-cost and ease to manufacture. Nonetheless, there are still some issues regarding their stability against atmospheric conditions that need to be understood. This dissertation focuses on the characterization of the electrical properties at the nanoscale of perovskite-based thin films by means of scanning probe microscopies (Conducting AFM, Kelvin Probe Force Microscopy, and Scanning Microwave Microscopy).

In this growing field of research, many perovskite structures, deposition methods, and synthesis routes have been developed and introduced in perovskite-based solar cells. In the first part of this dissertation, the context of perovskite materials is detailed and the methodology used through the thesis is also described. Then, we study and compare the electronic properties at the surface of perovskite materials synthesized following two different routes. Moreover, it is known that device engineering can increase both, the performance, and the stability of perovskite solar cells.

In a second part if the thesis, we show that for a given perovskite structure, the stability upon exposure to controlled small amounts of water can be significantly improved through the synthesis optimization. Finally, we provide a series of conclusions and perspectives that could help to further understand the perovskite behaviour at the local scale and to improve the cell performances.

Résumé

Le réchauffement climatique constitue aujourd'hui une des principales préoccupations de notre société. Année après année, son impact et ses conséquences sont de plus en plus visibles. L'accord de Paris a fixé pour objectif de limiter les émissions de CO_2, principalement issues de la demande croissante d'énergie à base de combustibles fossiles. Depuis, la communauté scientifique a multiplié ses efforts dans la recherche de sources alternatives d'énergie propres telles que les énergies renouvelables. À cet égard, l'énergie solaire est censée être une des principales sources d'énergie susceptibles de remplacer les combustibles fossiles. Par conséquent, les technologies photovoltaïques ont énormément évolué et les matériaux, dont notamment ceux à base de pérovskites hybrides organiques-inorganiques halogénées, ont été parmi les technologies ayant connu la croissance la plus rapide des performances des cellules solaires. En effet, les matériaux de type pérovskite possèdent des propriétés uniques telles que la flexibilité, le faible coût et la facilité de fabrication. Néanmoins, il reste encore quelques problèmes importants concernant leur stabilité face aux conditions atmosphériques. Cette thèse porte sur la caractérisation des propriétés électroniques, à l'échelle nanométrique, des couches minces à base de pérovskite au moyen de microscopies à sonde locale (Conducting AFM, Kelvin Probe Force Microscopy, and Scanning Microwave Microscopy).

Dans ce domaine de recherche en pleine croissance, de nombreuses structures de pérovskite, des méthodes de dépôt et des voies de synthèse ont été développées et introduites dans des cellules solaires à base de pérovskite. La première partie de cette thèse consiste à détailler le contexte des matériaux pérovskites et à décrire la méthodologie utilisée dans le cadre de cette thèse. Ensuite, nous étudions et comparons les propriétés électroniques à la surface de matériaux pérovskites synthétisés suivant deux voies différentes. Il est également connu que l'ingénierie des dispositifs augmentait les performances et la stabilité des cellules solaires en pérovskite. Dans la seconde partie de cette thèse, nous montrons que, pour une structure de pérovskite donnée, la stabilité vis-à-vis de l'exposition contrôlée à des petites quantités d'eau peut être considérablement améliorée par l'optimisation de la synthèse. Pour terminer, nous proposons une série de conclusions et de perspectives qui pourraient aider à mieux comprendre le comportement de la pérovskite à l'échelle locale et à améliorer les performances des cellules solaires.

Scientific activities during candidature

Peer review publication

J. Llacer, D. Moerman, O. Douhéret, X. Noirfalise, C. Quarti, R. Lazzaroni, D. Théron and P. Leclère, ACS Applied Nano Materials, 2020, 3, 8268-8277.

Conference attendance

1. SEPV2018: Stability of Emerging Photovoltaics: from Fundamentals to Applications, Barcelona (Spain).

   Received a grant from StableNextSol COST Members to attend the conference and make an oral presentation.

   Poster and oral presentation:

   ***J. Llacer**, D. Moerman, O. Douhéret, D. Théron and P. Leclère, "Addressing the Perovskite Stability Issue by Scanning Probe Microscopy and Macroscopic Impedance Spectroscopy".*

2. Forum des Microscopies à Sonde Locale, La Rochelle (France).

   Poster presentation.

3. Doctoral School: Excitonics for Photonic Applications, Les Houches (France).

   Poster presentation.

Internship

Research Stay at Universidad Pablo de Olavide, 8th - 19th October 2018, Sevilla (Spain).

Table of Contents

Abstract ..... **i**

Scientific activities during candidature ..... **v**

List of Abbreviations ..... **xi**

Chapter 1: Introduction **1**

1.1 Photovoltaics 2

1.2 Perovskite Properties 7

1.2.1 Crystal Structure 7

1.2.2 Optoelectronic Properties of Perovskites 9

1.3 Working Mechanism of Perovskite Solar Cells 11

1.3.1 Hysteresis 16

1.3.2 Structural Defects in Perovskites 19

1.3.3 Stability of Perovskite Solar Cells 21

1.3.4 Charge Transport Layers in Perovskite Solar Cells 26

1.4 Objectives and Outline of the thesis 28

References 30

Chapter 2: Materials and Methods **41**

2.1 Frabrication Process 42

2.2 Characterization Techniques 47

2.2.1 X-ray Diffraction 48

2.2.2 X-ray Photoelectron Spectroscopy 49

2.2.3 UV-Visible Spectroscopy 50

2.2.4 Atomic Force Microscopy 50

2.2.5 Conductive AFM 53

2.2.6 Kelvin Probe Force Microscopy 55

2.2.7 Scanning Microwave Microscopy 60

References 74

Chapter 3: Local Electronic Heterogeneities on the $CH_3NH_3PbI_3$ Perovskite Surface 78

3.1 Introduction 79

3.2 Characterization of the $CH_3NH_3PbI_3$ surface 81

3.4 Alternative $CH_3NH_3PbI_3$ surface 90

3.5 Conclusions 93

References 93

Chapter 4: $CH_3NH_3PbI_3$ Perovskite Thin Film Capacitance Study at the Nanoscale 99

4.1 Introduction 100

4.2 Topography Crosstalk 101

4.3 Calibration for Capacitance Measurements 104

4.4 Local Capacitance 105

4.5 Conclusions 111

References 112

Chapter 5: Early Stage Stability on the $CH_3NH_3PbI_3$ Perovskite Surface 115

5.1 Introduction 116

5.2 Sample Preparation for Tests 117

5.3 Impact of Small Amounts of Water on the $CH_3NH_3PbI_3$ perovskite surface 118

5.4 Tracking the Structural Evolution at the Early Stage of Water Degradation 121

5.5 Conclusions 128

References 129

Chapter 6: Conclusions and Outlook 132

6.1 Conclusions 133

6.2 Outlook 134

References 135

Abbreviations & Symbols

AFM	Atomic force microscopy
AM1.5G	Air mass 1.5 global
C-AFM	Conductive atomic force microscopy
CB	Conduction band
CIGS	copper-indium-gallium-diselenide
CZTSSe	Copper-zinc-tin-sulfide-selenide
CdTe	Cadmium telluride
DSSC	Dye sensitized solar cells
DMF	Dimethylformamide
DMSO	Dimethyl sulfoxide
E_b	Binding energy
E_c	Conduction band energy
E_F	Fermi level energy
E_g	Bandgap energy
ETL	Electron transport layer
E_{top}	Energy at the top
F	Fermi Dirac distribution
FA	Formamidiunium
FF	Fill factor
GW	Gigawatts
HOPG	Highly oriented polygraphite
HTL	Hole transport layers
ITO	Indium tin oxide
J_0	Saturation current density
J_{mpp}	Maximum power point

J_{sc}	Short circuit current density
k_B	Boltzmann constant
KPFM	Kelvin probe force microscopy
MA	Methylammonium
MAI	Methylammonium iodide
N	Density of states
n	electron density
N_c	Effective density of states
OPV	Organic photovoltaic
PCE	Power conversion efficiency
PEDOT:PSS	Poly(3,4-ethylenedioxythiophene) poly(styrenesulfonate)
P_{in}	Input power
P_{max}	Maximum electrical power
P_{out}	Output power
PSC	Perovskite solar cell
PV	Photovoltaics
Q	Charge of an electron
QD	Quantum dots
SMM	Scanning microwave microscopy
T	Temperature
TW	Terawatts
UV-Vis	Ultraviolet-visible absorption spectroscopy
VB	Valence band
V_{oc}	Open circuit voltage
V_{mpp}	Maximum voltage point
wt%	Weight percent
XPS	X-ray photoelectron spectroscopy
XRD	X-ray diffraction

Chapter 1

Introduction

This chapter serves as an introduction to the evolution of photovoltaic technologies and specifically to hybrid perovskite materials used as solar cells. An overview of the perovskite properties, their performances in solar cells and the main concerns in the community is also included. Finally, the outline is provided along with the objectives of this thesis.

1.1 Photovoltaics

Energy is at the centre of the human civilization. We, as humans, rely on energy for every aspect in our life, and this trend increases with the civilization development. Energy can be produced from fossil fuels or from renewable energies. Unfortunately, the energy production is mainly made from fossil fuels, which result in the emission of carbon dioxide (CO_2). This CO_2 has a greenhouse effect that drastically modifies the Earth's climate, resulting in what nowadays we know as the "global warming" effect. The global warming is in particular causing sea levels to rise, resulting in flooding and erosion of coastal and low-lying areas.

For this purpose, renewable energies have captured much of the attention; they can produce energy from clean (and renewable) sources. In fact, for many years renewable energies were the only source of energy.[1] Nonetheless, it was with the discovery of cheaper energy sources such as fossil fuels or nuclear energy, renewable energies were put aside. CO_2 emissions are growing since the industrial revolution, with fossil fuels becoming the 66.8% of the total electricity production in 2017. The main countries contributing to the global warming are China (28% of the total fossil fuel emissions), United States (14%) and India (7%).[2] Now we start to see the consequences and renewable energies are gaining interest again. The main sources of renewable energies are wind, hydroelectric, geothermal, tides and sunlight. While wind and hydroelectric sources are the main renewable technologies generating power, the power generation capacity from solar photovoltaics (solar PV) is expected to increase tremendously by 2040, as in **Fig. 1.1**. Each renewable technology has its own challenges, however, with the technology development of the last years, they are being improved and, at this moment, they are one of the major solutions to global warming.

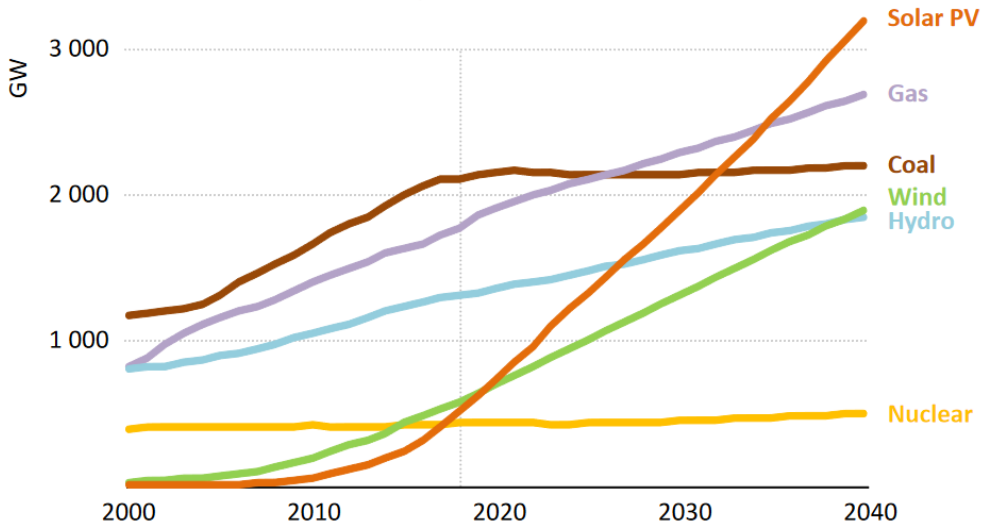

Figure 1.1. *Installed power generation capacity by source in the Stated Policies Scenario, 2000-2040.*[2]

Photovoltaic technologies emerged as one of the simplest energy solutions to implement in order to reduce the effects of the climate change. Solar panels can transform light into energy and can be installed on buildings. They require less infrastructure than other renewable technologies. This makes them a suitable solution for developing countries, especially in regions like Africa where, for instance, wind or hydroelectric technologies are not feasible.

The actual challenge is to substitute fossil fuels, which were providing around 80% of the total energy demand worldwide in 2013.[2] This translates into around 18 TW continuous power in a year. It may seem a huge amount of energy to cover, however, the Earth receives around 0.8 x 10^5 TW of solar power, which could be a sufficient amount in just one hour to supply the whole population for a year. The European photovoltaic industry association represented well the amount of energy that the Earth receives and the capacity of the actual energy technologies, **Fig. 1.2**.[3]

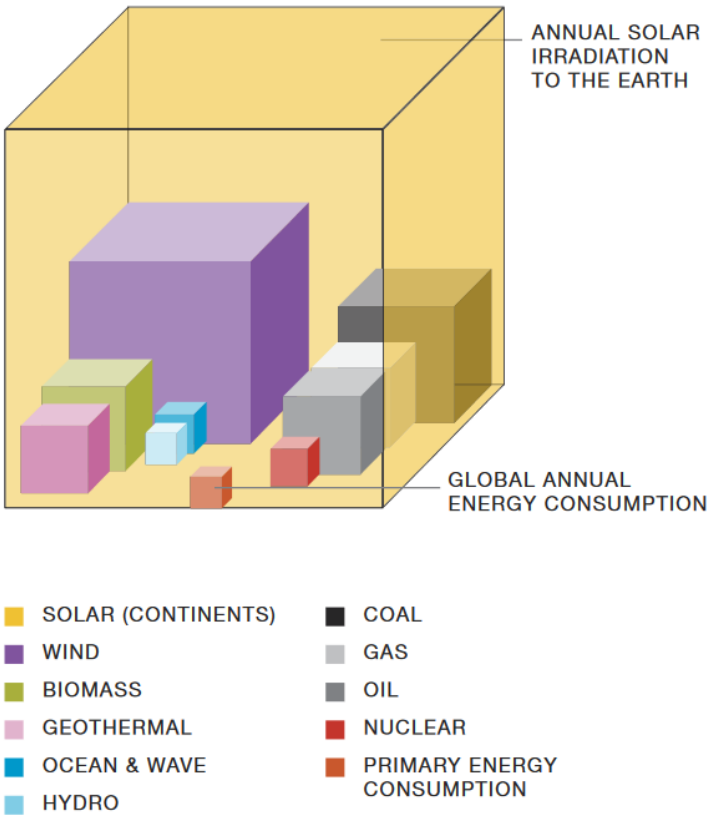

Figure 1.2. *Comparison of the capacity of the actual energy technologies with the amount of energy that the earth receives from sun.*[3]

Nonetheless, nowadays only 23.7% of the energy consumption is coming from renewable energies. From the renewable energies, solar PV contributes just with a 2.2% but as previously mentioned, their capacity of energy generation is expected to increase to more than 1 TW by 2023, **Fig. 1.3**.[4]

Solar PV gained attention since Becquerel discovered the photovoltaic effect in 1839, but it was in 1954 when solar cells stood out.[5] The Bell Laboratories provided a silicon-based solar cell for a space program, with a power conversion efficiency (PCE) of 4.5%.[6] The main characteristic of silicon solar cells consist in a p-silicon and an n-silicon region, forming a p-n junction. The success of that technology depends on the development of materials that allow high power at a minimum cost. The price has been decreasing for the last 30 years, what makes it even harder for renewable energies to be competitive. Even if silicon-based solar cells were traditionally the best performing solar cells with the best silicon-based solar cell now performing at 26.7% efficiency, they have several constraints.[7] Silicon is made through a highly demanding energy process and, together with their lifetime and costs from the solar panels, make it a technology far from ideal.

However, the lower cost of multi-crystalline silicon panels, compared to crystalline devices, made them the preferred source of energy even if their efficiency was slightly lower, with their highest PCE at 23.3%.[8] Regarding their lifetime, silicon solar cells last around 30 years, and their payback time is meant to be around 10 years, what means only 20 years of effective production in a solar plant. Indeed, the expected amount of energy required for the entire world for 2050 is of 30 TW, in order to supply a similar amount of energy just with solar plants (10 km^2 for 1 GW), an area as large as India would be needed.[4] Great advances have been achieved in making them cheaper and more efficient. This allowed the installation of solar panels in conventional houses; however, there is still room for improvement. Pollution could be tremendously reduced if more people had access to solar panels.

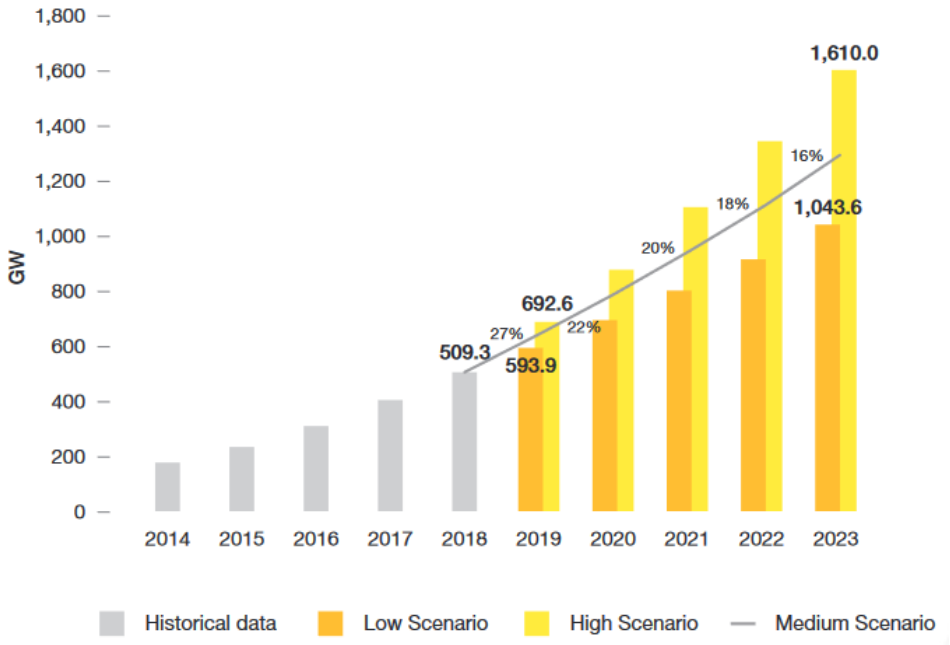

Figure 1.3. *Global total solar photovoltaic market scenario until 2020 predicted by Solar Power Europe.*[4]

With the purpose to overcome these problems, second generation solar cells were developed. Here, solar cells were fabricated with glass or stainless steel as a substrate and thin films were deposited on top (~ 1 µm). The thickness reduction compared to silicon solar cells (~ 100 µm) allowed for a reduction in cost and weight. The main thin film materials used in the second generation include copper-indium-gallium-diselenide (CIGS), cadmium telluride (CdTe), amorphous silicon (a-Si) copper-zinc-tin-sulfide-selenide (CZTSSe). Thin films such as CdTe has a lower efficiency than silicon solar

cells, 22.1%, but their advantage lies in their temperature coefficient.[8] CdTe can stand high temperatures better than silicon; at 65 ºC their efficiency loss is around 8.4 % while the loss for silicon solar cells is of around 18%.[9] CIGS showed high efficiencies in the order of 22-23 %, however, it is necessary to find non-toxic and low cost alternatives for these materials.[10–14] One of the best candidates in second generation solar cells with non-toxic materials is Cu_2ZnSnS_4 (CZTS).[15]

With further efforts to reduce costs and to be competitive against more conventional energy sources, third generation solar cells emerged. This last wave of new technologies gained much attention as their improvements have been done in a short period of time. Materials used in third generation are not used in a conventional p-n junction system to extract charge carriers anymore, instead they have the ability separate carriers by themselves. They are rather sandwiched between a *p* and an *n* material, creating structures such as: p-i-n or n-i-p (they will be further described in the next sections). They can be deposited on flexible surfaces and they are cheaper than the later solar cell generations. Third generation technologies involve dye-sensitized solar cells (DSSC), quantum dots (QD), organic photovoltaic (OPV) and, lately, perovskite solar cells (PSC). Dye-sensitized solar cells were the most popular since the early 90s. Among the typical dyes were ruthenium adsorbed to a mesoporous layer of titanium dioxide (TiO_2) or cobalt (III/II) redox complexes. DSSC efficiency is now around 15%, which is a low efficiency when compared to later generations.[16] The introduction of perovskites as a DSSC did not gain much interest but, when Chung *et al.* used them in solid state (PSC), they increased their efficiency dramatically up to 10.2% and its popularity increased as well.[17] They are now one of the most promising alternatives to silicon solar cells. In this thesis, we focus in perovskite materials, one of the most popular materials not only for third generation PV technologies but also in the energy field.

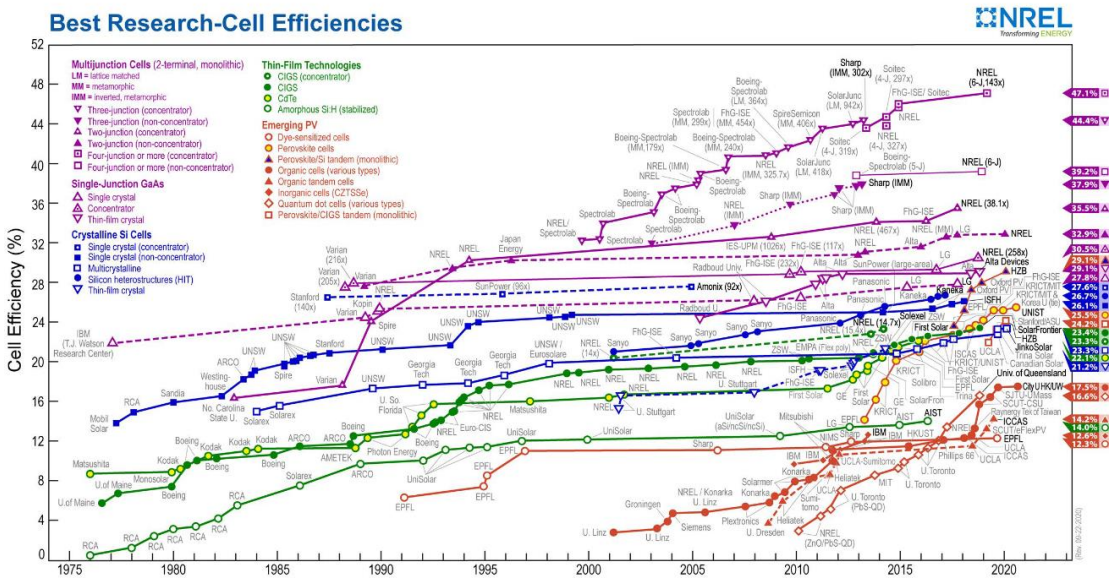

Figure 1.4. *Evolution of the solar cell performance for the different photovoltaic technologies.*[18]

1.2 Perovskite Properties

Perovskites have been found to make highly efficient solar cells. Recent reports have demonstrated that one day they could replace silicon as in their very rapid development, they have reached efficiencies of 25.2%, a level reached by silicon-based solar cells only 20 years ago.[19] Because of their long charge diffusion lengths and low defect densities they have low recombination rates, thus, perovskites enabled a breakthrough in solution processed photovoltaic devices. Besides, perovskite solar cells are manufactured using simple upscalable solution processing methods. As such, this technology presents a really serious alternative to silicon solar cell technology. The prospects seem to be as bright for other optoelectronic applications of the perovskite materials, for example in display technologies.[20,21]

1.2.1 Crystal structure

Perovskites typically have an ABX_3 crystal structure, **Fig. 1.5**, composed of five atoms per unit cell, with metal cation B at the center, cation A at the corners, and six anions X shaping the corners of an octahedron and placed at the center of six planes of the unit cell.

A sites are generally Cesium (Cs) or organic cations, B sites are either Pb or Sn and are surrounded by anion X within a [$BX_{6/2}$] octahedral framework. X sites are usually halides.

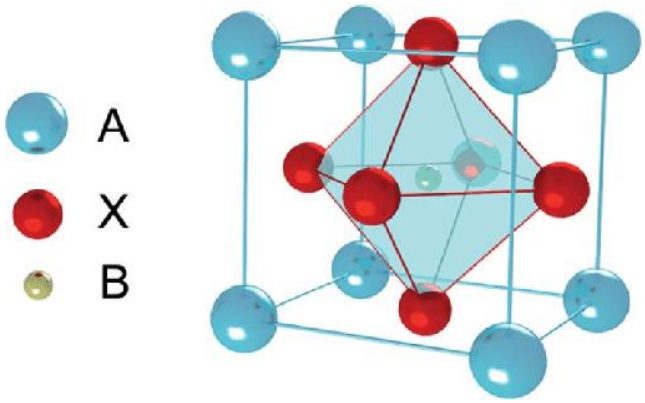

Figure 1.5. *ABX_3 Perovskite crystal structure.*

Perovskite structures can vary depending on the cation in the A site. For instance, $CH_3NH_3PbI_3$ ($MAPbI_3$) can adopt different structures upon heating, see **Table 1**.[22,23] $MAPbI_3$ perovskite is orthorhombic below 161 K, tetragonal from 161 to 330 K and cubic above 330 K.[22] In fact, substituting methylammonium (CH_3NH_3, MA) cation with bigger cations such as formamidinium ($CH(NH_2)_2^+$, FA), ethylammonium ($CH_3CH_2NH_3^+$, EA), butylammonium ($CH_3(CH_2)_3NH_3^+$, BA), guanidinium ($CH_3(NH_2)_3^+$, GA) or combination of cations, can lead to different structures or even form a layered structure instead of a 3D one. The most commonly used ratio to predict the perovskite formation is the Goldschmidt tolerance factor (t), defined as[24]

$$t = \frac{r_A r_x}{\sqrt{2}(r_B + r_x)} \qquad (1.1)$$

Where r_A and r_B are the ionic radius of the A and B cations respectively and, r_x is the ionic radius of the anion. The tolerance factor is used to assess if the A site cation fits in the cavities of the BX_3 framework. Perovskites form between 0.8 and 1, while cubic perovskites form within the range 0.9-1.0, distorted perovskites can be found between 0.8-0.9 due to tilting of the BX_6 octahedra and lowering the symmetry. If we go out of the range say lower than 0.8, the perovskite may be too distorted, if we go around a tolerance factor of 1.1, the A site cation is too large and thus the perovskite cannot be formed. A second parameter used together with the tolerance factor is the octahedral factor (μ), this factor predicts the stability of the BX_6^{-4} octhaedral framework, it is given by

$$\mu = \frac{r_B}{r_x} \qquad (1.2)$$

Table 1: *Phase transitions of $MAPbI_3$ determined from synchrotron X-ray powder diffraction data. Temperatures were equilibrated for approximately 10 minutes after 1 K changes.*[25]

Structural transition	Transition Temperature (K) heating	Transition Temperature (K) cooling
Pm-3m* to *I4/mcm	338	338
I4/mcm* to *Pnma	-	160-165

The octahedral factor values range from 0.44 to 0.90 for a stable structure.[26] It is known that analogues of $MAPbI_3$ made progress in photovoltaic applications and they were introduced in other optoelectronic applications, however, they are moisture sensitive and have low thermal stability.[27] Other A cations showed an improved stability, carrier lifetime and diffusion length in the form of single crystal and solution processed films. In addition, FA^+ has a larger ion radius than MA^+, which leads to a higher tolerance factor that is closer to 1.[28] Cation A can enhance the properties and, a combination of cations could make improvements that are even more significant. Anion X usually is bromine, iodine or chlorine.

1.2.2 Optoelectronic Properties of Perovskites

Organic-inorganic halide perovskites are very interesting for photovoltaic applications due to their optoelectronic properties. They show a very good optical absorption due to their tunable bandgap (see **Fig. 1.6a** and **b**), long diffusion lengths, high carrier mobility and high tolerance to defects.[29–36] In particular, $MAPbI_3$ is the most studied perovskite material in solar cells and its properties are believed to be representative for most of the perovskites. $MAPbI_3$ shows a sharp absorption peak, indicating a direct bandgap of 1.55 eV.[29–34] Indeed, the $MAPbI_3$ absorption coefficient is so high that the absorption in the visible spectrum is still achievable at thicknesses in the order of 300 nm, which is much thinner than the typical thickness (above 1 μm) required for other solar cell active layers. The absorption coefficient below the bandgap shows the Urbach tail or Urbach energy.[37]

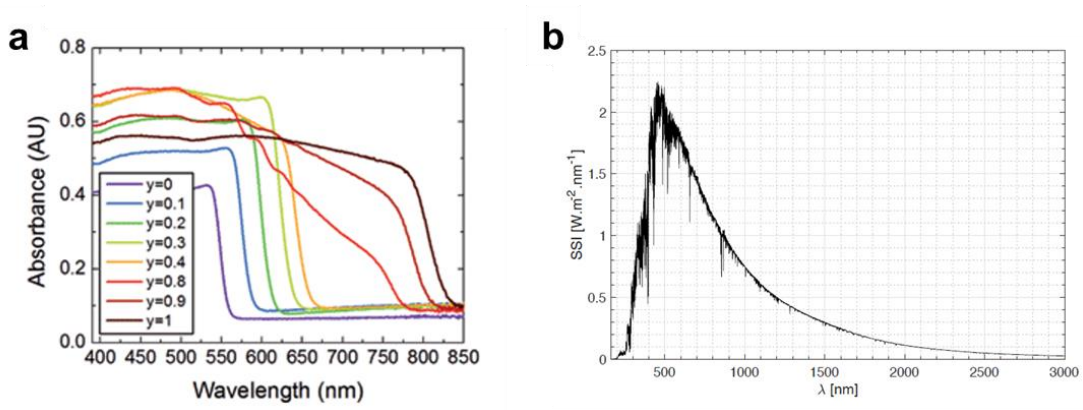

Figure 1.6. *(**a**) UV-Vis absorption spectra of $FAPbI_yBr_{3-y}$ perovskites. (**b**) Solar spectrum recorded on the International Space Station.*[38,39]

The Urbach energy determines the degree of structural and electronic disorder within the material.[40,41] This effect was detected when measuring the absorption of a defective perovskite crystal, defects induce additional states extended a few meV from the sharp band edges, broadening the Urbach tail.[42] The Urbach value obtained for $MAPbI_3$ is as low as 15 meV, explaining the high V_{oc} in perovskite solar cells.[43] Another property in perovskite solar cells is their high charge mobility, around 25 $cm^2/V{\cdot}s$, related to the ionicity of the metal-halide bond.[44] A high mobility and a low non-radiative recombination leads to carrier diffusion lengths are as large as 100 nm for both electrons and holes in $MAPbI_3$. it increases up to 175 nm in $MAPbI_3$ single crystals due to the reduction of defects.[45]

All the above described properties and findings together with a PSC device structure optimization allowed for efficiencies as high as 24.2%.[46] With efficiencies approaching the theoretical maximum efficiency (30.14%), also known as the Shockley-Queisser (S-Q) limit, the question that arises is how to continue reducing the gap.[47] If we take as a reference the reported PSC with 24.2% efficiency, the FF x V_{oc} product is still far from the theoretical value by 25%.[46] This means that research must be directed towards the origin of the FF and V_{oc} lowering effects. So far, the causing effect has been addressed to non-radiative charge recombination and it can be divided in two processes: Shockley-Read-Hall (SRH) recombination and interface recombination.[48] Another typical recombination process is band-to-band recombination but this one is radiative recombination and when there is only radiative recombination, the PSCs efficiencies could theoretically reach the S-Q limit.[47] However, non-radiative recombination processes are still present in perovskites and their origin is mainly due to defects in the

crystal structure. Moreover, defects are not only responsible of lower PSC efficiencies but also they are detrimental for their stability. All these detrimental effects induce hysteresis during I-V scans.

1.3 Working Mechanism of Perovskite Solar Cells

A perovskite solar cell is, in general terms, composed of the perovskite material sandwiched between two electrodes, one of which is transparent to allow the light to pass through and reach the perovskite layer. This layer is commonly covered by a hole transport layer and an electron transport layer, HTL and ETL respectively. Multiple structures have been developed to improve the PCE, however, they can be classified in two major groups: n-i-p structures, where the perovskite is deposited on top of the ETL as in **Fig. 1.7a**; and p-i-n structures, where the perovskite is deposited on top of the HTL as in **Fig. 1.7b**. In n-i-p structures, the most common structure contains a mesoporous TiO_2 layer as ETL. Since the contact area with the photoactive layer was increased, it was believed that it helped with the extraction of charges. Later on, other structures without the mesoporous scaffold showed high efficiencies as well, proving that charges can be transported to the respective electrodes by the perovskite itself.[49] Now, whether the mesoporous TiO_2 layer improves the PCE remains an open question. Both structures, n-i-p and p-i-n, have shown to provide high efficiencies, therefore, the choice of one structure over the other is merely a question of a better stability, a reduced hysteresis (see **section 1.3.2**) or other preparation advantages that one structure may have over other ones.[50–53]

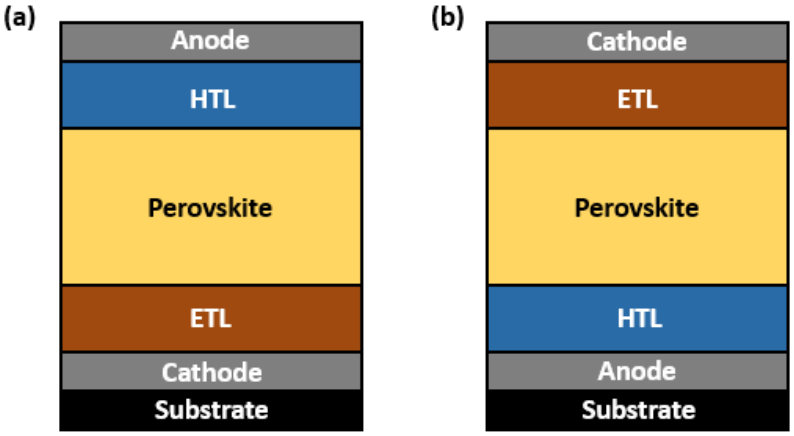

Figure 1.7. *Perovskite solar cells with* ***(a)*** *n-i-p and* ***(b)*** *p-i-n structures.*

Solar cells working principle relies on the absorption of light (photons). The absorption of light produces electrical energy in the form of current and voltage. For that purpose, the photoactive material in the solar cell absorbs the light when the photon energy is higher than the bandgap of the material. Therefore, the bandgap of the active material should be minimized. We expect the efficiency of the solar cell to increase with the light absorption capability, however, when the bandgap energy is much lower than the photon energy, there is an excess of energy which is lost. Bandgap optimization is then a trade-off between photon harvesting and maximization of the energy of extracted charges.

To evaluate the performance of terrestrial solar cells, the light source irradiated into the solar cell is standardized. The irradiation should have an air mass 1.5 global (AM1.5G), with an intensity of 1000 W/m^2.[54] The AM1.5G includes direct and diffuse light only. With a standard procedure and with a solar simulator it is easy to compare the performance of solar cells regardless of the weather.

The light absorption promotes an electron from the ground state to an excited state. The highest energy where the electrons can be found is the valence band (VB) while the lowest energy band where there are not electrons is called the conduction band (CB). The transition of an electron to an excited state in the CB creates an electron (negative charge) and a hole (positive charge) carrier pair, as represented in **Fig. 1.8**. The electron-hole pair (also called an exciton) attracts each other with a binding energy (E_b) of the order of < 5 meV for perovskites.[55] Since the E_b is lower than the thermal energy at room temperature (around 25 meV), the light absorption will create free charges.[56]

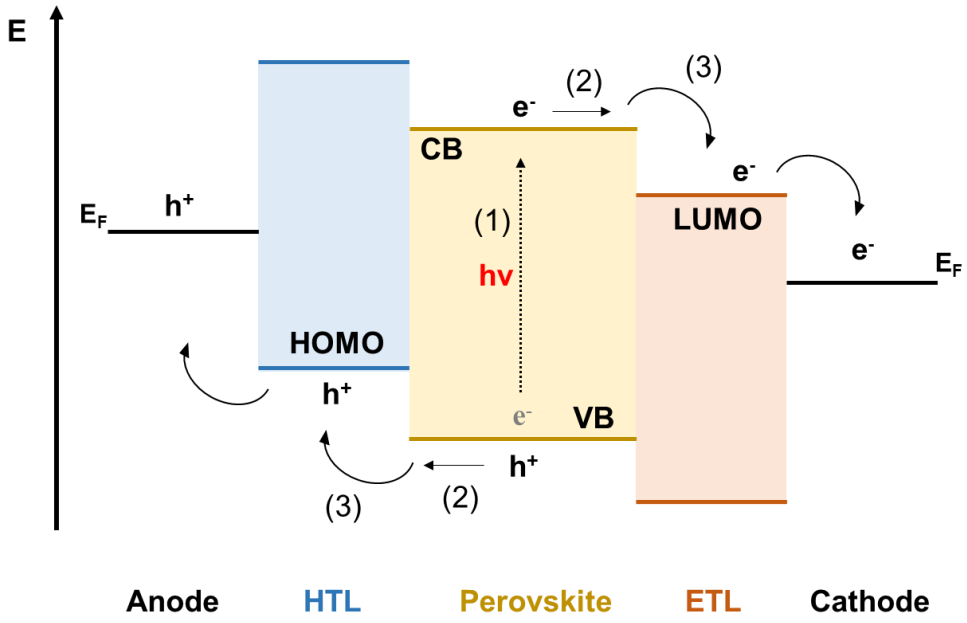

Figure 1.8. *Scheme of the basic mechanism in a perovskite solar cell: (1) light absorption and exciton generation, (2) exciton migration and (3) charge carrier transfer and extraction to the electrodes.*

The photogenerated negative charges need to be separated to the cathode and the photogenerated positive charges need to be collected at the anode (exciton migration), both processes are normally ruled out by drift and/or diffusion. For a better extraction, the layer thickness should be smaller than the charge diffusion length. Once the electron reaches the cathode, it travels through an external electric circuit to return to the anode of the cell. Finally, the charge combines with a positive charge and the absorber returns to the ground state. When scanning the voltage under dark and illuminated conditions, a plot of the current density-voltage (J-V) is obtained as in **Fig. 1.9**.

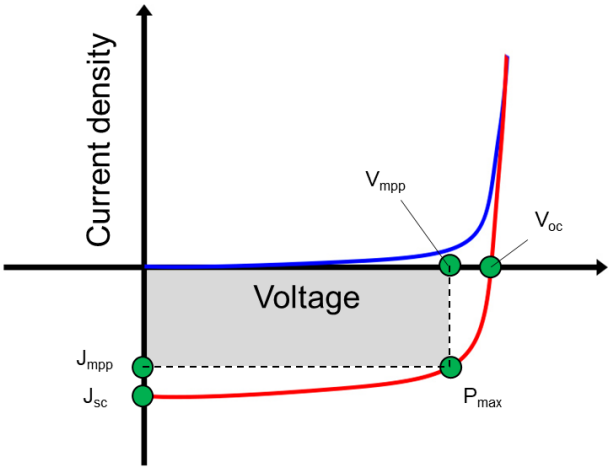

Figure 1.9. *J-V curves of a solar cell under dark (blue curve) and illumination (red curve) conditions with the main points labelled. The grey rectangle represents the fill factor.*

If we consider the number of occupied conduction band (CB) levels from the energy at the bottom of the CB (E_c) to infinite (or the energy at the top, E_{top}), the expression of n is thus given by

$$n = \int_{E_c}^{E_{top}} N(E)\, F(E)\, dE \cong N_C e^{(\eta_e - E_C)/k_B T} \qquad (1.3)$$

where N(E) is the density of states and F(E) is the Fermi-Dirac distribution.[57] Then, following this equation, the electrochemical potential (η_e) of an electron in the CB is

$$\eta_e = E_c - k_B\, T\, ln\frac{N_c}{n} \qquad (1.4)$$

where k_B is the Boltzmann constant, n is the electron density, N_c is the effective density of states (amount available states close to the band edge) and T the temperature. If we then take into account that the electrochemical potentials are quasi-Fermi energies that may be different between the different layers when an external bias V is applied, the concentration of electrons (n) and holes (p) in the conduction band and valence band respectively is given by

$$n = N_c \exp(-\frac{E_c - E_F^n}{k_B T}) \qquad (1.5)$$

$$p = N_v \exp(-\frac{E_F^p - E_v}{k_B T}) \quad (1.6)$$

where E_F^n is the Fermi level of n-type semiconductors and E_F^p is the Fermi level of p-type semiconductors. From **Eq. 1.5** and **Eq. 1.6** and taking into account that the charge of an electron times the photovoltage follows the relationship: $qV = E_F^p - E_F^n$, we obtain

$$np = N_c N_v \exp\left(-\frac{E_g - qV}{k_B T}\right) \quad (1.7)$$

where E_g is the bandgap energy of the perovskite. The probability of an electron to find a hole and recombine is higher in open-circuit condition, as previously discussed, then

$$qV_{oc} = E_g - k_B \, T \ln \frac{N_C N_V}{np} \quad (1.8)$$

where there is a relationship between V_{oc}, *np* product, temperature and bandgap.

The short-circuit current density (J_{sc}) is the maximum photo-generated current that can be achieved. It is the point where no voltage is applied between the anode and the cathode (see **Fig. 1.9**). In fact, for an ideal diode, the photocurrent is

$$J_{ideal} = J_{sc} - J_0 \left[\exp\left(\frac{qV}{k_B T}\right) - 1\right] \quad (1.9)$$

where J_0 is the saturation current. Now, the ideal open-circuit voltage when only radiative recombination is present, can be defined as[58]

$$V_{oc} = \frac{k_B \, T}{q} ln\left(\frac{J_{sc}}{J_0} + 1\right) \quad (1.10)$$

The maximum electrical power (P_{max}) point is the position on the I-V curve where the maximum product between current density (J_{mpp}) and voltage (V_{mpp}) is reached. The fill factor (FF) describes the ideality of a solar cell, that is, how close is the J-V curve to form a rectangle like in **Figure 1.9** and can be expressed as

$$FF = \frac{J_{mpp} \, V_{mpp}}{J_{sc} \, V_{oc}} \quad (1.11)$$

The power conversion efficiency (PCE) determines the performance of a solar cell. It is the ratio between the output and input power, P_{out} and P_{in} respectively.

$$PCE = \frac{P_{out}}{P_{in}} \quad (1.10)$$

Still, the PCE can be hindered by multiple reasons. For perovskite solar cells two of the main issues are the hysteresis in the I-V measurements and the presence of defects within the material.

1.3.1 Hysteresis

Hysteresis in perovskite solar cells refers to the divergence between the I-V curves measured in forward (from short circuit to open circuit) and reverse (from open circuit to short circuit) scan directions and the time scale for this effect is ~ 100 sec.[59,60] Hysteresis has a temporal-dependence behaviour, what means that can be modified with parameters such as scan speed, scan direction or scan range.[61] Altogether, it is an evidence of poor stability.[62,63] A typical hysteretic behaviour was previously shown in **Fig. 1.10** and the general trend is to measure a higher current in reverse scan direction than in forward scan direction.

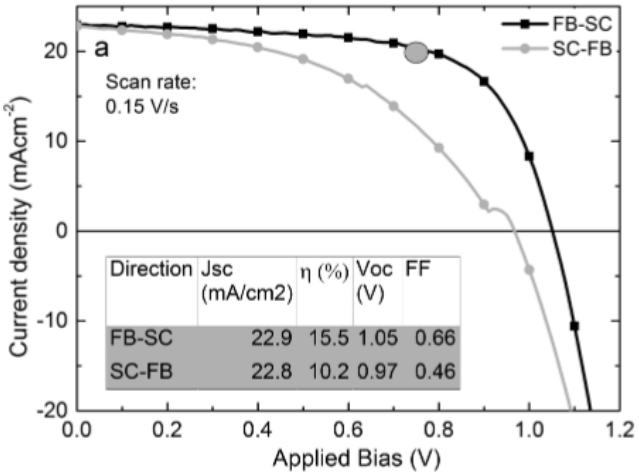

Figure 1.10. *Forward bias to short circuit (FB-SC) and short circuit to forward bias (SC-FB) current−voltage curves measured for the same halide perovskite-based solar cell. The inset table gives the determined performance parameters.*[62]

This means that one or more processes of the solar cell working mechanism (before described) is being disturbed. Considering that carrier generation and carrier transport are rather fast processes, the lower carrier collection seen in forward scan must be attributed to the transport at the interfaces. Although the origin of the hysteresis effect is still a subject of debate, three main approaches have been proposed to be causing it: ferroelectricity, charge trapping/detrapping and ion migration.

Ferroelectricity

Ferroelectricity appears when spontaneous polarization (P), generated from non-centrosymmetric structures, can be switched by an external electric field. Several groups claimed that $MAPbI_3$ exhibits a ferroelectric behaviour despite being a centrosymmetric tetragonal space group of *I4/mcm*.[64,65] Nonetheless, the central MA cation is mobile and can change its orientation, thus decreasing the lattice symmetry.[66] Several ferroelectric domains were detected using Piezoresponse force microscopy (PFM), a tool used for probing local ferroelectric response.[64,67–70] The polarization of these domains alters the band structure at the interface, resulting in a modified I-V performance between forward and reverse scans. Ferroelectric polarization was demonstrated by Wei *et al.*, who proposed a model for this behaviour.[71] With an external field, the MA cation can align to follow the direction of the applied field, resulting in a depolarization of the field. However, P cannot follow the speed of the voltage scan, so the excess polarization generates a transient current state. This excess polarization on forward scan direction is parallel to the internal field, what makes the transient current to be lower than in reverse scan direction. Nonetheless, models such as the one described for the perovskite ferroelectricity are questioned by number of other groups.[67,72,73] Some claim that there is no ferroelectric behaviour in perovskites and some other pointed that even if Wei *et al.* found ferroelectric properties, they are too small to cause the hysteretic behaviour seen by other groups.[71]

Ion Migration

Ion migration being the cause of J-V hysteresis gained more attention than ferroelectricity.[74] Here, under an external electrical field, positive and negative ions are driven towards the respective electrodes. Ions accumulate at the interface between the transport layers and the perovskite, resulting in a change of the polarity and the modulation of the interfacial barrier energies, thus producing hysteresis.[75,76] In a perovskite system, the elements that can diffuse are the organic cations, halide anions and metallic ions. However, heavy metal cations like Pb^{+2} have low mobility and are not considered as a diffusive part. Smaller organic cations will diffuse faster than larger ones and, halides are considered to have the highest mobility compared to its counterparts.[77,78] Regarding the diffusion of organic cations like MA^{+}, it was observed an increase in concentration when poling the sample.[79] They accumulate at the interface and align with

the field, hindering charge extraction.[80] However, the estimated diffusion coefficient of iodide ions in $MAPbI_3$ ranges from 10^{-11} to 10^{-12} cm^2/s, far from the estimated value for MA^+ cations, 10^{-16} cm^2/s.[78] Meanwhile, Li *et al.* detected the migration of iodide anions to the positive electrode, which have an estimated coefficient of diffusion within the range before mentioned.[81] The migration of iodide ions can generate hydrogen ions, impacting the mobile defects.[82] However, these hydrogen ions are not considered to be responsible of the observed hysteresis since their concentration remains low due to the weak acidity of methylammonium.[83] When iodide ions migrate, they leave vacancies, which are driven towards the negative electrode and, Xiao et al. suggested they are responsible for n-doping under an external electric field.[84] The ion migration was proposed to take place by a hopping mechanism. Ions will migrate through vacant sites: MA^+ goes into a vacant cage, and iodide ions move along the Pb-I octahedra.[78] Migration can occur when the PbX_3 framework opens, and the energy required is called the activation energy (E_a). Therefore, iodide ions can migrate through iodide vacancies (V_I) or iodide interstitials (I_i), with a lower activation energy required for migration through vacancies.[85] Therefore, it seems reasonable that hysteresis can be originated from ion migration. However, other groups investigated hysteresis effects with the same $MAPbI_3$ crystal but with other ETLs and HTLs, establishing lower hysteresis features.[86] This behaviour means that ion migration cannot be responsible for the hysteresis effect alone. Instead, a combination of both, ion migration and trap states might be a better explanation.[74,85,87]

Charge trapping/detrapping

Another factor that should be taken into account is the relationship of trap states with hysteresis effects. Trap states have also been proposed as the origin of hysteresis since the existence of traps in perovskites has been widely discussed.[87,88] Trap states may appear with low temperature fabrication processes (solution process) and, ultimately, they affect charge transport, separation and recombination.[88] Among the possible traps, shallow and deep, it is true that perovskites show low Urbach energies, in the order of 20-40 meV, which implies a high structural quality and electronic properties together with high mobilities.[89] On the contrary, deep traps are associated to Shockley-Read-Hall non-radiative recombination and lead to a performance losses.[90,91] A mechanism of trapping-detrapping was described to produce hysteresis.[92] Shallow traps can be filled by charges and then released with changing bias while deep trap states can produce a change in the

electric field, resulting in a hysteresis in J-V performance.[92] Even if perovskites are found to have low trap densities, they are dominantly accumulated at the interface or at the surface where the structure is not as crystalline as the bulk.[56,93] However, these traps can also be driven to the surface due to strong electron-phonon coupling.[94] The accumulation phenomena has been observed by Kelvin Probe Force Microscopy (KPFM) at the interface between the perovskite and the HTL after turning on the light.[95,96] These traps can be passivated by adding additional thin films of fullerene, which was observed to reduce hysteresis.[97,98] Even if these findings suggest that traps are behind the hysteresis effect, the trapping and detrapping effect takes place in the order of ms or ns, which is far from the hysteresis times. The lower trap density in perovskites makes it also hard to believe that hysteresis is only related to the traps.[99,100] Finally, traps should be filled with increasing illumination intensity, thus decreasing the hysteresis, what happens to be the contrary to what it is observed. As a matter of fact, the actual debate is not whether hysteresis arises from trap states or ion migration. It is about how much the hysteresis is affected from ion migration and how much from trap states.

1.3.2 Structural Defects in Perovskites

As previously discussed, defects can create traps and are detrimental for PSC performance, however, there is a big discussion about the role they play in the PSC stability. To understand how defects affect the electronic structure of perovskite materials, the origin of the electronic levels must be clarified.

Energy band structure

In $MAPbI_3$, the electronic levels of the MA cation lie deep within the valence and conduction bands (VB and CB respectively), which means that the band edges are determined by the BX_6 octahedra. Due to the ionicity between the Pb and I atoms in $MAPbI_3$, the CB is determined from the Pb p orbitals. The covalent antibonding coupling between Pb p and I p states is not strong, therefore, the CB energy is just slightly higher than the atomic Pb p states, as in **Fig. 1.11**. However, the VB does have a strong anticoupling bonding between Pb s and I p states, raising the VB energy above the I p orbital level. The electronic states are then affected when substituting the halide, for instance, the bandgap increases from 1.5 eV in $MAPbI_3$ to 2.3 eV in $MAPbBr_3$ due to the smaller size of Br ions, which also originates in a different electronic energy

distribution.[101] Defects induce additional states which could be positioned between the CB and VB, thus, affecting the V_{oc} and device performance. Leijtens *et al.* investigated the high V_{oc} observed in perovskite solar cells and observed that trapped electrons possess long lifetimes, only recombining with free holes over the course of many microseconds. Traps will be filled, thus inducing higher V_{oc}.[102]

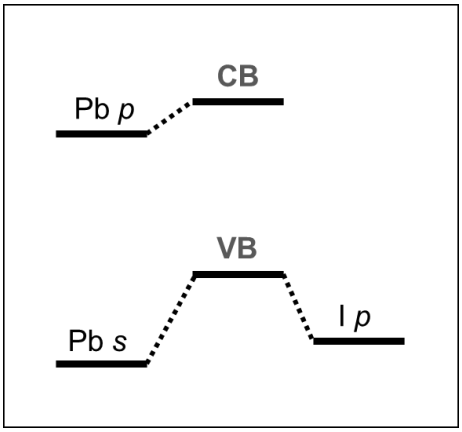

Figure 1.11. *Schematics of the VB and CB in $CH_3NH_3PbI_3$ perovskites.*[103]

Structural defects

Defects are normally addressed in the bulk, however defects present at the surface cause electronic heterogeneities and condition the electronic properties of the perovskite, which are directly involved in the charge extraction.[104] Traps can be classified as shallow or deep, which means they are located either close to the band-edges or close to the mid-gap, respectively. Specifically, the possible point defects in $MAPbI_3$ can be induced by Pb or MA vacancies (V_{Pb} and V_{MA}, respectively), substitution of I atoms at Pb or at MA sites (I_{Pb} and I_{MA}, respectively), substitution of MA ions at Pb sites (MA_{Pb}) and I interstitials (I_i). Calculations on the formation energies of all the possible point defects can be seen in **Fig. 1.12** and revealed that shallow trap states are much more likely than deep traps, and they can be an explanation for the long electron-hole diffusion lengths observed in these materials.[105,106] Among these defects, MA_{Pb}, V_{MA}, and V_{Pb} have low formation energies and correspond to shallow traps. Yet, Du *et al.* reported that I_{MA} and I_{Pb}, considered as deep traps with high formation energies, can transform into V_{Pb}, V_{MA} and I_i.[107] I_i defects have low formation energy (from 0.23 to 1.42 eV compared to 1.85 to 4.24 eV in I_{Pb} and I_{MA}) and create deep trap levels.[105]

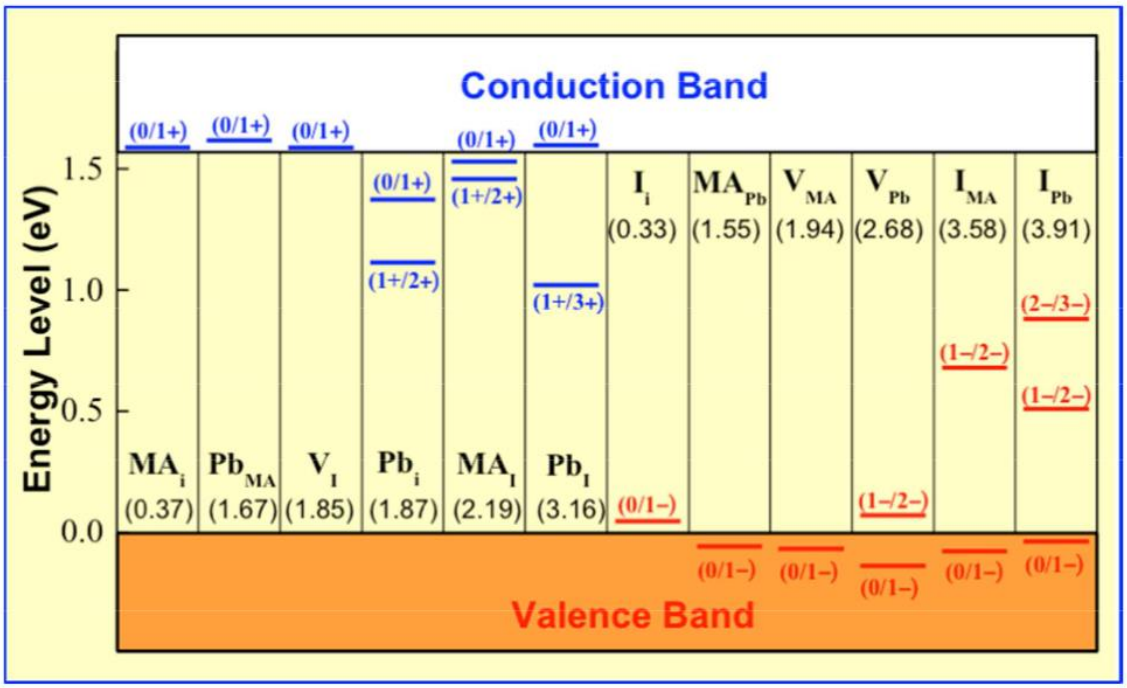

Figure 1.12. *Calculated transition energy levels of donor-like and acceptor-like point defects in $MAPbI_3$. The possible defect charges are noted in parentheses at the band level position. Also in parentheses are the formation energies for the neutral defects.*[103]

All these studies are also pointing out how the type and density of traps at the surface of the perovskite are depending on the growth conditions of the materials along with the anisotropy of the surface properties. In spite of the type of defects present at the surface, their intrinsic role against stability is still under debate. To enhance perovskite stability, it is crucial to understand how these defects affect the bulk properties and how they interact with water molecules, especially at the early stage of degradation. Together with defects, other factors are also causing some concerns in perovskite solar cells. The toxicity of lead, their I-V hysteresis losses and their environmental stability makes them a potential technology to be further improved.

1.3.3 Stability of Perovskite Solar Cells

At atmospheric conditions, perovskite materials suffer degradation from a number of environmental factors. They can be classified in three groups: degradation induced by the illumination, the temperature and/or the moisture. A wide range of stability studies have been performed for each degradation process, however, there is mainly one thing they have in common: the majority of them were carried out using $MAPbI_3$. It is the most

studied perovskite so far and the perovskite studied in this work. Therefore, here there are some of the most remarkable findings concerning stability of PSC.

Prolonged radiation exposure of PSCs, specially UV radiation, is one of the characteristic degradation processes seen in perovskites.[108] Radiation instabilities were first seen at the interface between the mesoporous titanium oxide (TiO_2) and the perovskite. Oxygen vacancies or Ti^{3+} exist in the deep level electron sites of TiO_2, which facilitate the interaction with the oxygen creating a charge transfer complex.[109]

$$CH_3NH_3PbI_3 \xrightarrow{hv} CH_3NH_3PbI_3{}^* \tag{1.13}$$

$$O_2 \xrightarrow{CH_3NH_3PbI_3{}^*} O_2{}^{*-} \tag{1.14}$$

$$CH_3NH_3PbI_3 + \frac{1}{4}\,O_2{}^{*-} \xrightarrow{deprotonation} CH_3NH_2 + PbI_2 + \frac{1}{2}I_2 + \frac{1}{2}H_2O \tag{1.15}$$

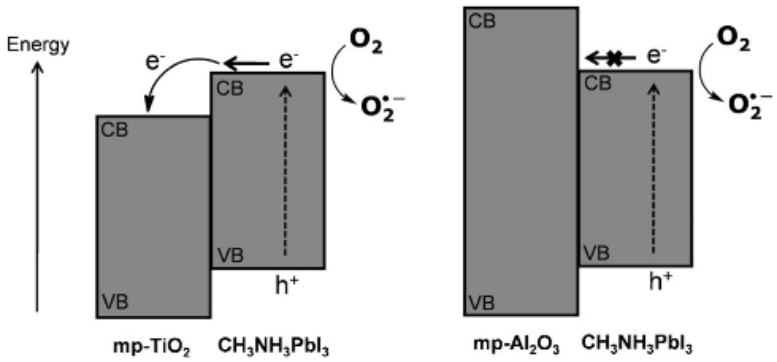

Figure 1.13. *Schematic model showing the capture of excited electron and formation superoxide. Due to favourable energy offset, some electrons can be accepted easily in the case of m-TiO_2 (left) and due to the high energy difference between the perovskite and the mesoporous Al_2O_3, electrons cannot be injected into perovskite instead are captured by molecular oxygen resulting in the formation of superoxide (right).*[110]

After light absorption, an electron-hole pair is created and separated to the CB and VB respectively. The hole at the VB recombines with the electron from the oxygen at the adsorption site, creating an excess of electrons and, at the same time, creating oxygen vacancies in the TiO_2 surface.[111–113]

To overcome this problem, one of the most popular solution was to introduce mesoporous Al_2O_3 to replace the mesoporous layer of TiO_2 as in **Fig. 1.13**.[114–116] **Fig. 1.13** shows the work where the Al_2O_3 mesoporous layer was compared to the TiO_2 mesoporous layer,

showing a better electron blocking.[110] The perovskite suffers also photo-degradation by itself, and even more when it is exposed to oxygen at the same time.[117] Regarding the effects of UV-light illumination in the perovskite layer, the inorganic PbI^{2+} can capture two electrons and result in Pb and I decomposition.[118–120] As a solution it was suggested to add an excess of PbI^2.[121] Altogether, illumination in PSCs may induce a bandgap change and an interfacial geometry change.[122]

Temperature conditions are also an important factor for the PSC performance. When combined with light radiation, the $MAPbI_3$ perovskite starts the degradation process at 75 ºC due to the weak Pb-I bond, which can be broken by incident photons. However, without light influence, perovskite decomposition starts above 85 ºC, specially suffering high decomposition at 95 ºC, following the **Reaction 1.16**.[120,123] The exact degradation mechanism is not well understood, however, the consensus is that perovskites suffer tremendous degradation above 100 ºC.[124]

$$CH_3NH_3PbI_3\ (s) \xrightarrow{\Delta} NH_3\ (g) + CH_3I\ (g) + PbI_2\ (s) \qquad (1.16)$$

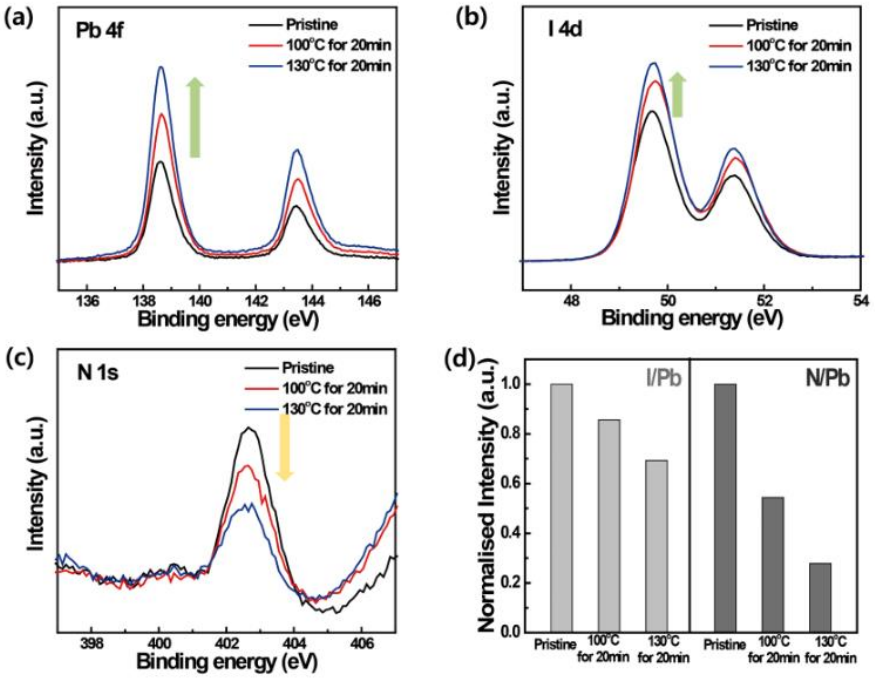

Figure 1.14. *In-situ HR-XPS spectra of both pristine and thermally treated $MAPbI_3$. The graphic shows the iodine to lead (I/Pb) and nitrogen to lead (N/Pb) ratio in both pristine and thermally treated samples.*[124]

Thermal degradation, contrary to light degradation, starts from the perovskite surface and it continues progressively in the bulk, see **Fig. 1.14**.[124] The degradation mechanism is still under debate, with a general consensus claiming that high temperature is enough to degrade the perovskite layer.

Moisture degradation is one of the major concerns in the perovskite community too.[125–130] With an organic cation (like MA^+ or FA^+) in the center of the perovskite structure, it makes the perovskite extremely vulnerable to water interactions. That is why, the PSCs are fabricated in inert atmospheres such as a nitrogen-filled glovebox. This type of degradation is not clearer than the ones described before, that is why many groups are trying to solve this critical issue.[33,127,131–136] One of the first degradation mechanisms proposed was the Grotthuss mechanism, here the proton in the MA^+ cation is transferred to the water molecules. Water molecules transfer the proton to the halide compound, resulting in HI and PbI_2 formation.[132] Then, some groups proposed that with the sole presence of water, the perovskite structure was directly degraded into PbI_2.[33,137]

Most recently, several groups claimed that intermediate hydrated-phases such as $CH_3NH_3PbI_2{\cdot}H_2O$ and/or $(CH_3NH_3)_4PbI_6{\cdot}H_2O$ are formed in the first moments of moisture degradation to finally decompose into PbI_2, **Fig. 1.15**.[127,133,134] Interestingly, they were detected by X-ray diffraction studies.[127,133] These studies were more keen to a degradation mechanism starting with perovskite hydration rather than an acidic-base reaction proposed in the beginning (Grotthuss mechanism). More detailed studies by Leguy *et al.* showed that the hydrated intermediates are reversible upon drying as in the following reaction:[135]

$$4CH_3NH_3PbI_3 + 4H_2O \leftrightarrows 4[CH_3NH_3PbI_3 \cdot H_2O] \quad (1.17)$$

$$4[CH_3NH_3NH_2 \cdot H_2O] \leftrightarrows (CH_3NH_3)_4 + PbI_6 \cdot H_2O + 3PbI_2 + 2H_2 \quad (1.18)$$

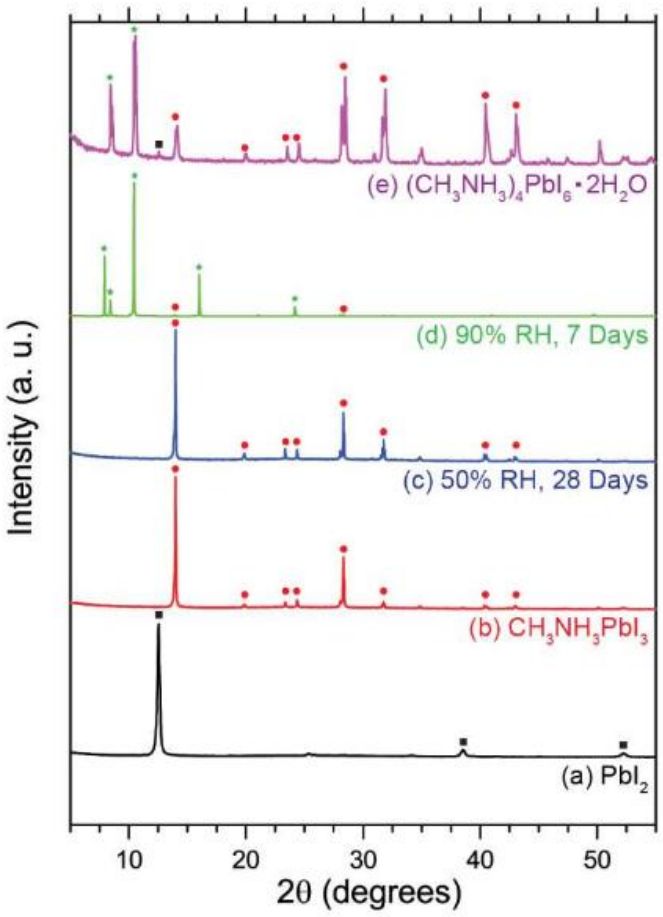

Figure 1.15. *XRD analysis of pristine and degraded $CH_3NH_3PbI_3$. Black squares, red circles, and green stars shows PbI_2, pristine $CH_3NH_3PbI_3$ and hydrated $CH_3NH_3PbI_3$ respectively.*[127]

Later on, Zhao *et al.* suggested that these intermediate phases were not fully reversible.[134] In fact, it was Chen *et al.* who showed that the degradation was reversible in the first 5h of water exposure with a PCE drop of 27%, nonetheless they did not recover the initial PCE after thermal annealing.[121] They went further and degraded irreversibly the PCE by 20% with PbI_2 formation as a result and, after 70 h, it was degraded retaining only 2% of PCE. Mosconi *et al.* showed by DFT calculations the different facets that can be present in the $MAPbI_3$ perovskite surface.[138] They can be either terminated with the methylammonium iodide cation (MAI-terminated) or with the lead iodide octahedra (PbI-terminated), being the later ones more resistant to solvation due to a stronger Pb-I bond.[121,125,138,139] As one can imagine, even if the mechanism behind the moisture-induced degradation is still under debate, there is a general consensus about the presence of intermediate phases appearing before irreversible degradation. Now, the possible

degradation mechanisms can be minimized through the combination of different transport layers, which not only transport charges but also can protect the perovskite from degradation.

1.3.4 Charge Transport Layers in Perovskite Solar Cells

Stability issues can get worse or can be reduced depending on the transport layers in which the perovskite is in contact. There are several options for both, the electron transport layer and the hole transport layer. The most evident important characteristic to pay attention when choosing the transport materials is the energy band alignment.[140] However, other aspects such as stability of the material or their degree of solubility will directly affect the solar cell performance. A degraded transport layer will perturb the carrier collection efficiency and, subsequently, the PCE. Transport materials can be either organic or inorganic ones. For the ETL, suitable compounds should be related to negligible hysteresis, flexibility and easy fabrication at low temperatures.[86,98,141,142] The typical ETLs used in n-i-p structure are TiO_2, SnO_2 and ZnO. It can be used as a compact layer or as a mesoporous layer but it has been in the mesoporous configuration where they showed higher carrier extraction due to its large area of contact with the perovskite.[143] TiO_2 can be deposited in multiple ways. The preferred deposition techniques are spray-pyrolysis, sol-gel, atomic layer deposition and electrodeposition because of the advantage of low temperature processing over other techniques such as radiofrequency sputtering, electron-beam evaporation or thermal oxidation.[144–146] However, from **section 1.3.4** we know the mesoporous TiO_2 layer has a poor stability. In fact the TiO_2 layer can lower the PCE by dropping 10-30% of its initial value after several hours.[147] As a result, alternatives such as ZnO emerged, showing higher electron mobility and the ability to be flexible.[148] Moreover, doping the ZnO with nitrogen or aluminium increased its stability and, at the same time, kept a high PCE.[149] SnO_2 was another alternative to TiO_2 due to its deeper conduction band. As counterparts, its bandgap is wide, which means less UV light absorption.

On the other hand, in p-i-n structure the most common ETL are fullerene derivatives such as [6,6]-phenyl-C61-butyric acid methyl ester (PCBM) or C_{60}, **Fig. 1.16a**.[141] Fullerenes help to passivate the perovskite surface and reduce the effects of deep traps.[150] Most common materials used as HTLs are poly(3,4-ethylenedioxythiophene) polystyrene

sulfonate (PEDOT:PSS), 2,2',7,7'-Tetrakis[N,N-di(4-methoxyphenyl)amino]-9,9'-spirobifluorene (Spiro-OMeTAD) and poly(triarylamine) (PTAA), see **Fig. 1.16a, c, b** and **f** respectively. However, it is worth to mention other materials used as HTL in PSC such as CuSCN or NiO_x, with high stabilities and performances, however, they are not used as much as PEDOT:PSS or Spiro-OMeTAD. PEDOT:PSS is a mixture of the PEDOT polymer with PSS, which makes the PEDOT soluble. PEDOT:PSS is the most used material as HTL in p-i-n structures due to its ease of fabrication by solution process, transparency and appropriate valence band energy with respect to those of perovskites. However, since PEDOT:PSS can accelerate the perovskite degradation, MoO_3 was introduced to improve its stability.[151,152] Spiro-OMeTAD is the most used material as HTL in n-i-p structures because of energy alignment and amorphous character.[153] However, it is doped with Bis(trifluoromethane)sul-fonimide lithium salt (LiTFSI) , **Fig. 1.16e**, which is attracted to water molecules, and, tert-butyl pyridine (TBP), **Fig. 1.16d**, with a low boiling temperature. Altogether, this makes Spiro-OMeTAD an unstable material.[154] An alternative to Spiro-OMeTAD is PTAA, which showed an improved stability against light and temperature.[155] Using buffer layers between the perovskite and the PTAA layer, the Liu *et al.* achieved a PCE of 20.7%.[156]

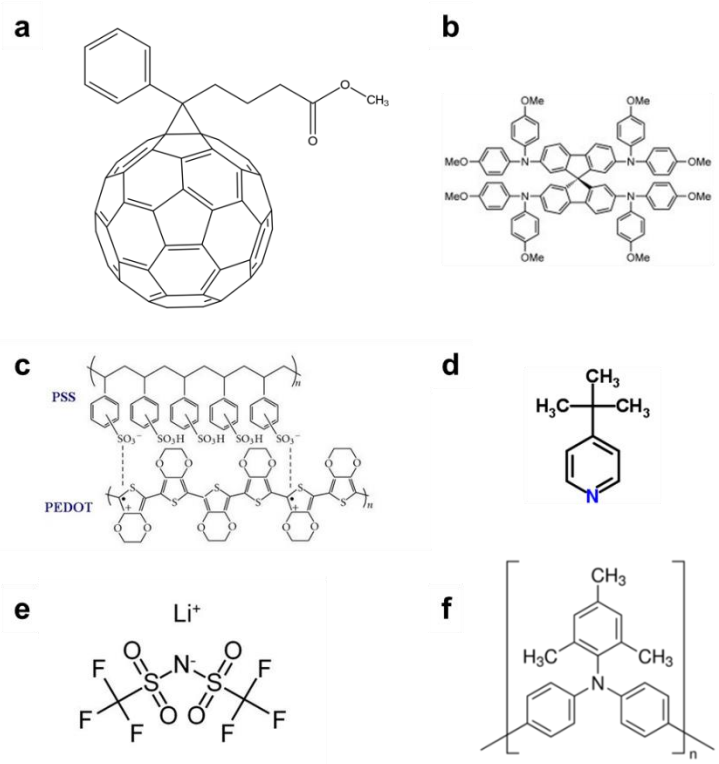

Figure 1.16. *Chemical structure of: (**a**) PCBM, (**b**) Spito-OMeTAD, (**c**) PEDOT:PSS, (**d**) TBP, (**e**) LiTFSI and (**f**) PTAA.*

Regardless of the intrinsic properties of the charge transport layers above mentioned, the growth conditions of the perovskite should be taken into account. Even if the growth process for perovskites is not well understood, it is known that depending on the material beneath the perovskite, the growth conditions will differ, thus, its electronic properties. Some studies showed a preferential order when the perovskite is deposited on top of TiO_2 due to local interactions.[157] There are also studies that compare the energy band positions of the perovskite when deposited on different substrates (for instance TiO_2, ZnO and PEDOT:PSS).[158] Therefore, even if the focus of this thesis is not related to PSC performance directly, the choice of a transport layer is also important. Since the tests that were going to be performed to characterize the perovskite layer are slow by themselves, a fast deposition process was preferred. In this aspect PEDOT:PSS was chosen, not only it allows for a relatively fast deposition process but it is also highly reproducible, cheap and very common material used as HTL in perovskite solar cells. Although it was described earlier that it can be unstable, it is sandwiched between the back electrode and the perovskite, limiting its contact with atmospheric conditions, moreover, it is used in controlled environments and under an inert N_2 atmosphere.

1.4 Objectives and Outline of the Thesis

From the above considerations, it is clear that there are many detrimental effects in perovskite materials causing them to outperform and, lately, to be chemically degraded. The understanding of the processes taking place in the degradation process is of high importance for their commercialization as solar cell devices. In this regard, the ultimate goal of this work is to contribute to the development of perovskite-based solar cells by providing experimental insight about the perovskite reactivity upon water exposure at the nano-level.

To do so, scanning probe microscopy techniques have been used through all the thesis to understand the electronic behaviour of the perovskite surface which, ultimately, could help to understand the behaviour at the interface between the perovskite and the eventual transport layer in a solar cell stack. After the introduction of this chapter, *Chapter 2* provides a description of the sample preparation conditions and the used techniques through this thesis. *Chapter 3* compares the local electronic behaviour of two perovskite synthesis routes both leading to $MAPbI_3$. The discussion lies around the presence of two

dominating domains at the surface of one of the synthesis routes (MAPI-$PbAc_2$), with a difference in work function between these domains. The main experimental measurements were performed by KPFM and C-AFM.

The optimization of the measuring parameters and conditions has taken quite some work in *Chapter 4*. This includes not only testing both perovskite synthesis routes by Scanning Microwave Microscopy (SMM) but also finding the optimal procedure to extract some meaningful results. The chapter discusses about the suitability of the mentioned technique to characterize a semiconductor such as perovskite. Continuing with the characterization of the two different perovskite synthesis routes, we use the capabilities of the SMM to track any hysteretic effect.

Chapter 5 takes a closer on the surface stability from both $MAPbI_3$ perovskites upon water exposure. Based on these results, we perform an evaluation of which perturbing phenomena is making the stability difference. In the last part of the thesis, in *Chapter 6*, final conclusions and outlook of the thesis are presented. Various studies are proposed in view of further complementary analysis of the perovskite surface.

References

1. Sørensen, B. A history of renewable energy technology. *Energy Policy* **19**, 8–12 (1991).
2. World Energy Outlook 2019 – Analysis. *IEA* https://www.iea.org/reports/world-energy-outlook-2019.
3. Teske, S. & Masson, G. Solar generation 6. Solar photovoltaic electricity empowering the world. (2011).
4. Global Market Outlook 2019-2023 – SolarPower Europe. https://www.solarpowereurope.org/global-market-outlook-2019-2023/.
5. Gates, D. M. Direct Use of the Sun's Energy. Farrington Daniels. Yale University Press, New Haven, Conn., 1964. xviii + 374 pp. Illus. Paper, $2.45; cloth, $7.50. *Science* **148**, 790–791 (1965).
6. Green, M. A. The path to 25% silicon solar cell efficiency: History of silicon cell evolution. *Progress in Photovoltaics: Research and Applications* **17**, 183–189 (2009).
7. Yoshikawa, K. *et al.* Silicon heterojunction solar cell with interdigitated back contacts for a photoconversion efficiency over 26%. *Nature Energy* **2**, 1–8 (2017).
8. Green, M. A. *et al.* Solar cell efficiency tables (Version 53). *Progress in Photovoltaics: Research and Applications* **27**, 3–12 (2019).
9. Friesen, G., Pavanello, D. & Virtuani, A. Overview of Temperature Coefficients of Different Thin Film Photovoltaic Technologies. *25th European Photovoltaic Solar Energy Conference and Exhibition / 5th World Conference on Photovoltaic Energy Conversion, 6-10 September 2010, Valencia, Spain* 4248–4252 (2010) doi:10.4229/25thEUPVSEC2010-4AV.3.83.
10. Simya, O. K., Mahaboobbatcha, A. & Balachander, K. A comparative study on the performance of Kesterite based thin film solar cells using SCAPS simulation program. *Superlattices and Microstructures* **82**, 248–261 (2015).
11. Hossain, M. I. Prospects of CZTS solar cells from the perspective of material properties, fabrication methods and current research challenges. in (2012).
12. Wang, W. *et al.* Device Characteristics of CZTSSe Thin-Film Solar Cells with 12.6% Efficiency. *Advanced Energy Materials* **4**, 1301465 (2014).
13. Bag, S. *et al.* Low band gap liquid-processed CZTSe solar cell with 10.1% efficiency. *Energy Environ. Sci.* **5**, 7060–7065 (2012).
14. Siebentritt, S. Why are kesterite solar cells not 20% efficient? *Thin Solid Films* **535**, 1–4 (2013).
15. Simya, O. K., Mahaboobbatcha, A. & Balachander, K. Compositional grading of CZTSSe alloy using exponential and uniform grading laws in SCAPS-ID simulation. *Superlattices and Microstructures* **92**, 285–293 (2016).

16. Upadhyaya, H. M., Senthilarasu, S., Hsu, M.-H. & Kumar, D. K. Recent progress and the status of dye-sensitised solar cell (DSSC) technology with state-of-the-art conversion efficiencies. *Solar Energy Materials and Solar Cells* **119**, 291–295 (2013).

17. Chung, I., Lee, B., He, J., Chang, R. P. H. & Kanatzidis, M. G. All-solid-state dye-sensitized solar cells with high efficiency. *Nature* **485**, 486–489 (2012).

18. Best Research-Cell Efficiency Chart. https://www.nrel.gov/pv/cell-efficiency.html.

19. Sahli, F. *et al.* Fully textured monolithic perovskite/silicon tandem solar cells with 25.2% power conversion efficiency. *Nature Materials* **17**, 820–826 (2018).

20. SciVPro | Perovskite LEDs | Prof. Sir Richard Friend and Dr Dawei Di. *Scientific Video Protocols* https://scivpro.com/manuscript/10_32386_scivpro_000008/ doi:10.32386/scivpro.000008.

21. Byun, J. *et al.* Efficient Visible Quasi-2D Perovskite Light-Emitting Diodes. *Advanced Materials* **28**, 7515–7520 (2016).

22. Onoda-Yamamuro, N. Calorimetric and IR spectroscopic studies of phase transitions in methylammonium trihalogenoplumbates (II)†. *Journal of Physics and Chemistry of Solids* **51**, 1383–1395 (1990).

23. Poglitsch, A. & Weber, D. Dynamic disorder in methylammoniumtrihalogenoplumbates (II) observed by millimeter-wave spectroscopy. *Journal of Chemical Physics* **87**, 6373–6378 (1987).

24. Liu, X., Hong, R. & Tian, C. Tolerance factor and the stability discussion of ABO3-type ilmenite. *J Mater Sci: Mater Electron* **20**, 323 (2008).

25. Whitfield, P. S. *et al.* Structures, Phase Transitions and Tricritical Behavior of the Hybrid Perovskite Methyl Ammonium Lead Iodide. *Scientific Reports* **6**, 35685 (2016).

26. Li, C. *et al.* Formability of ABX3 (X = F, Cl, Br, I) halide perovskites. *Acta Crystallogr., B* **64**, 702–707 (2008).

27. Hsu, H.-P., Li, L.-C., Shellaiah, M. & Sun, K. W. Structural, Photophysical, and Electronic Properties of CH 3 NH 3 PbCl 3 Single Crystals. *Scientific Reports* **9**, 13311 (2019).

28. Zhumekenov, A. A. *et al.* Formamidinium Lead Halide Perovskite Crystals with Unprecedented Long Carrier Dynamics and Diffusion Length. *ACS Energy Lett.* **1**, 32–37 (2016).

29. Burschka, J. *et al.* Sequential deposition as a route to high-performance perovskite-sensitized solar cells. *Nature* **499**, 316–319 (2013).

30. Liu, M., Johnston, M. B. & Snaith, H. J. Efficient planar heterojunction perovskite solar cells by vapour deposition. *Nature* **501**, 395–398 (2013).

31. Kojima, A., Teshima, K., Shirai, Y. & Miyasaka, T. Organometal Halide Perovskites as Visible-Light Sensitizers for Photovoltaic Cells. *J. Am. Chem. Soc.* **131**, 6050–6051 (2009).

32. Etgar, L. *et al.* Mesoscopic CH3NH3PbI3/TiO2 Heterojunction Solar Cells. *J. Am. Chem. Soc.* **134**, 17396–17399 (2012).

33. Frost, J. M. *et al.* Atomistic Origins of High-Performance in Hybrid Halide Perovskite Solar Cells. *Nano Lett.* **14**, 2584–2590 (2014).

34. Bernal, C. & Yang, K. First-Principles Hybrid Functional Study of the Organic–Inorganic Perovskites CH3NH3SnBr3 and CH3NH3SnI3. *J. Phys. Chem. C* **118**, 24383–24388 (2014).

35. Dualeh, A. *et al.* Impedance Spectroscopic Analysis of Lead Iodide Perovskite-Sensitized Solid-State Solar Cells. *ACS Nano* **8**, 362–373 (2014).

36. McMeekin, D. P. *et al.* A mixed-cation lead mixed-halide perovskite absorber for tandem solar cells. *Science* **351**, 151–155 (2016).

37. Urbach, F. The Long-Wavelength Edge of Photographic Sensitivity and of the Electronic Absorption of Solids. *Phys. Rev.* **92**, 1324–1324 (1953).

38. Chen, J., Zhou, S., Jin, S., Li, H. & Zhai, T. Crystal organometal halide perovskites with promising optoelectronic applications. *J. Mater. Chem. C* **4**, 11–27 (2015).

39. Solarspectrum. https://www.esa.int/ESA_Multimedia/Images/2017/12/Solar_spectrum.

40. Zhang, W. *et al.* Ultrasmooth organic-inorganic perovskite thin-film formation and crystallization for efficient planar heterojunction solar cells. *Nat Commun* **6**, 6142 (2015).

41. Cody, G. D., Tiedje, T., Abeles, B., Brooks, B. & Goldstein, Y. Disorder and the Optical-Absorption Edge of Hydrogenated Amorphous Silicon. *Phys. Rev. Lett.* **47**, 1480–1483 (1981).

42. Kim, J., Lee, S.-H., Lee, J. H. & Hong, K.-H. The Role of Intrinsic Defects in Methylammonium Lead Iodide Perovskite. *The Journal of Physical Chemistry Letters* **5**, 1312–1317 (2014).

43. De Wolf, S. *et al.* Organometallic Halide Perovskites: Sharp Optical Absorption Edge and Its Relation to Photovoltaic Performance. *J. Phys. Chem. Lett.* **5**, 1035–1039 (2014).

44. Ponseca, C. S. *et al.* Organometal Halide Perovskite Solar Cell Materials Rationalized: Ultrafast Charge Generation, High and Microsecond-Long Balanced Mobilities, and Slow Recombination. *J. Am. Chem. Soc.* **136**, 5189–5192 (2014).

45. Dong, Q. *et al.* Solar cells. Electron-hole diffusion lengths > 175 μm in solution-grown CH3NH3PbI3 single crystals. *Science* **347**, 967–970 (2015).

46. Green, M. A., Emery, K., Hishikawa, Y., Warta, W. & Dunlop, E. D. Solar cell efficiency tables (Version 45). *Progress in Photovoltaics: Research and Applications* **23**, 1–9 (2015).

47. Sarritzu, V. *et al.* Optical determination of Shockley-Read-Hall and interface recombination currents in hybrid perovskites. *Scientific Reports* **7**, 44629 (2017).

48. Park, N.-G. & Segawa, H. Research Direction toward Theoretical Efficiency in Perovskite Solar Cells. *ACS Photonics* **5**, 2970–2977 (2018).

49. Lee, M. M., Teuscher, J., Miyasaka, T., Murakami, T. N. & Snaith, H. J. Efficient hybrid solar cells based on meso-superstructured organometal halide perovskites. *Science* **338**, 643–647 (2012).

50. Sun, Q. *et al.* High-efficiency planar p-i-n perovskite solar cells based on dopant-free dibenzo[b,d]furan-centred linear hole transporting material. *Journal of Power Sources* **449**, 227488 (2020).

51. Yin, X. *et al.* Dithieno[3,2-b:2′,3′-d]pyrrol-Cored Hole Transport Material Enabling Over 21% Efficiency Dopant-Free Perovskite Solar Cells. *Advanced Functional Materials* **29**, 1904300 (2019).

52. Wang, Q., Dong, Q., Li, T., Gruverman, A. & Huang, J. Thin Insulating Tunneling Contacts for Efficient and Water-Resistant Perovskite Solar Cells. *Advanced Materials* **28**, 6734–6739 (2016).

53. Anaraki, E. H. *et al.* Highly efficient and stable planar perovskite solar cells by solution-processed tin oxide. *Energy Environ. Sci.* **9**, 3128–3134 (2016).

54. Reference Air Mass 1.5 Spectra | Grid Modernization | NREL. https://www.nrel.gov/grid/solar-resource/spectra-am1.5.html.

55. Miyata, A. *et al.* Direct measurement of the exciton binding energy and effective masses for charge carriers in organic–inorganic tri-halide perovskites. *Nature Physics* **11**, 582–587 (2015).

56. D'Innocenzo, V. *et al.* Excitons versus free charges in organo-lead tri-halide perovskites. *Nature Communications* **5**, 3586 (2014).

57. Sze, S. M. Physics of Semiconductor Devices, 3rd Edition | Wiley. *Wiley.com* https://www.wiley.com/en-be/Physics+of+Semiconductor+Devices%2C+3rd+Edition-p-9780471143239 (1981).

58. Tress, W. Perovskite Solar Cells on the Way to Their Radiative Efficiency Limit – Insights Into a Success Story of High Open-Circuit Voltage and Low Recombination. *Advanced Energy Materials* **7**, 1602358 (2017).

59. Sanchez, R. S. *et al.* Slow Dynamic Processes in Lead Halide Perovskite Solar Cells. Characteristic Times and Hysteresis. *J. Phys. Chem. Lett.* **5**, 2357–2363 (2014).

60. Gottesman, R. *et al.* Extremely Slow Photoconductivity Response of CH3NH3PbI3 Perovskites Suggesting Structural Changes under Working Conditions. *J. Phys. Chem. Lett.* **5**, 2662–2669 (2014).

61. Kim, H.-S. & Park, N.-G. Parameters Affecting I–V Hysteresis of CH3NH3PbI3 Perovskite Solar Cells: Effects of Perovskite Crystal Size and Mesoporous TiO2 Layer. *J. Phys. Chem. Lett.* **5**, 2927–2934 (2014).

62. Snaith, H. J. *et al.* Anomalous Hysteresis in Perovskite Solar Cells. *J Phys Chem Lett* **5**, 1511–1515 (2014).

63. Unger, E. L. *et al.* Hysteresis and transient behavior in current–voltage measurements of hybrid-perovskite absorber solar cells. *Energy Environ. Sci.* **7**, 3690–3698 (2014).

64. Stoumpos, C. C., Malliakas, C. D. & Kanatzidis, M. G. Semiconducting Tin and Lead Iodide Perovskites with Organic Cations: Phase Transitions, High Mobilities, and Near-Infrared Photoluminescent Properties. *Inorg. Chem.* **52**, 9019–9038 (2013).

65. Quarti, C., Mosconi, E. & De Angelis, F. Interplay of Orientational Order and Electronic Structure in Methylammonium Lead Iodide: Implications for Solar Cell Operation. *Chem. Mater.* **26**, 6557–6569 (2014).

66. Bakulin, A. A. *et al.* Real-Time Observation of Organic Cation Reorientation in Methylammonium Lead Iodide Perovskites. *J. Phys. Chem. Lett.* **6**, 3663–3669 (2015).

67. Kutes, Y. *et al.* Direct Observation of Ferroelectric Domains in Solution-Processed CH3NH3PbI3 Perovskite Thin Films. *J. Phys. Chem. Lett.* **5**, 3335–3339 (2014).

68. Kim, H.-S. *et al.* Ferroelectric Polarization in CH3NH3PbI3 Perovskite. *J. Phys. Chem. Lett.* **6**, 1729–1735 (2015).

69. Chen, B. *et al.* Interface band structure engineering by ferroelectric polarization in perovskite solar cells. *Nano Energy* **13**, 582–591 (2015).

70. Coll, M. *et al.* Polarization Switching and Light-Enhanced Piezoelectricity in Lead Halide Perovskites. *J. Phys. Chem. Lett.* **6**, 1408–1413 (2015).

71. Wei, J. *et al.* Hysteresis Analysis Based on the Ferroelectric Effect in Hybrid Perovskite Solar Cells. *J. Phys. Chem. Lett.* **5**, 3937–3945 (2014).

72. Leguy, A. M. A. *et al.* The dynamics of methylammonium ions in hybrid organic–inorganic perovskite solar cells. *Nature Communications* **6**, 7124 (2015).

73. Fan, Z. *et al.* Ferroelectricity of CH3NH3PbI3 Perovskite. *J. Phys. Chem. Lett.* **6**, 1155–1161 (2015).

74. Richardson, G. *et al.* Can slow-moving ions explain hysteresis in the current–voltage curves of perovskite solar cells? *Energy Environ. Sci.* **9**, 1476–1485 (2016).

75. Zhang, Y. *et al.* Charge selective contacts, mobile ions and anomalous hysteresis in organic–inorganic perovskite solar cells. *Mater. Horiz.* **2**, 315–322 (2015).

76. Zhao, Y. *et al.* Anomalously large interface charge in polarity-switchable photovoltaic devices: an indication of mobile ions in organic–inorganic halide perovskites. *Energy Environ. Sci.* **8**, 1256–1260 (2015).

77. Haruyama, J., Sodeyama, K., Han, L. & Tateyama, Y. First-Principles Study of Ion Diffusion in Perovskite Solar Cell Sensitizers. *J. Am. Chem. Soc.* **137**, 10048–10051 (2015).

78. Eames, C. *et al.* Ionic transport in hybrid lead iodide perovskite solar cells. *Nature Communications* **6**, 7497 (2015).

79. Yuan, Y. *et al.* Photovoltaic Switching Mechanism in Lateral Structure Hybrid Perovskite Solar Cells. *Advanced Energy Materials* **5**, 1500615 (2015).

80. Azpiroz, J. M., Mosconi, E., Bisquert, J. & Angelis, F. D. Defect migration in methylammonium lead iodide and its role in perovskite solar cell operation. *Energy Environ. Sci.* **8**, 2118–2127 (2015).

81. Li, C. *et al.* Iodine Migration and its Effect on Hysteresis in Perovskite Solar Cells. *Advanced Materials* **28**, 2446–2454 (2016).

82. Egger, D. A., Kronik, L. & Rappe, A. M. Theory of Hydrogen Migration in Organic–Inorganic Halide Perovskites. *Angewandte Chemie International Edition* **54**, 12437–12441 (2015).

83. Frost, J. M. & Walsh, A. What Is Moving in Hybrid Halide Perovskite Solar Cells? *Acc. Chem. Res.* **49**, 528–535 (2016).

84. Xiao, Z. *et al.* Giant switchable photovoltaic effect in organometal trihalide perovskite devices. *Nat Mater* **14**, 193–198 (2015).

85. Yu, H., Lu, H., Xie, F., Zhou, S. & Zhao, N. Native Defect-Induced Hysteresis Behavior in Organolead Iodide Perovskite Solar Cells. *Advanced Functional Materials* **26**, 1411–1419 (2016).

86. Heo, J. H., Han, H. J., Kim, D., Ahn, T. K. & Im, S. H. Hysteresis-less inverted CH3NH3PbI3 planar perovskite hybrid solar cells with 18.1% power conversion efficiency. *Energy Environ. Sci.* **8**, 1602–1608 (2015).

87. van Reenen, S., Kemerink, M. & Snaith, H. J. Modeling Anomalous Hysteresis in Perovskite Solar Cells. *J. Phys. Chem. Lett.* **6**, 3808–3814 (2015).

88. Yuan, Z. *et al.* Perovskite Solar Cells: Hot-Electron Injection in a Sandwiched TiOx–Au–TiOx Structure for High-Performance Planar Perovskite Solar Cells (Adv. Energy Mater. 10/2015). *Advanced Energy Materials* **5**, (2015).

89. Singh, S. *et al.* Effect of Thermal and Structural Disorder on the Electronic Structure of Hybrid Perovskite Semiconductor CH3NH3PbI3. *J. Phys. Chem. Lett.* **7**, 3014–3021 (2016).

90. Miller, O. D., Yablonovitch, E. & Kurtz, S. R. Intense Internal and External Fluorescence as Solar Cells Approach the Shockley-Queisser Efficiency Limit. *IEEE J. Photovoltaics* **2**, 303–311 (2012).

91. Wetzelaer, G.-J. A. H. *et al.* Trap-Assisted Non-Radiative Recombination in Organic–Inorganic Perovskite Solar Cells. *Advanced Materials* **27**, 1837–1841 (2015).

92. Li, W., Dong, H., Dong, G. & Wang, L. Hysteresis mechanism in perovskite photovoltaic devices and its potential application for multi-bit memory devices. *Organic Electronics* **26**, 208–212 (2015).

93. Yamada, Y., Nakamura, T., Endo, M., Wakamiya, A. & Kanemitsu, Y. Photocarrier Recombination Dynamics in Perovskite CH3NH3PbI3 for Solar Cell Applications. *J. Am. Chem. Soc.* **136**, 11610–11613 (2014).

94. Wu, X. *et al.* Trap States in Lead Iodide Perovskites. *J. Am. Chem. Soc.* **137**, 2089–2096 (2015).

95. Bergmann, V. W. *et al.* Local Time-Dependent Charging in a Perovskite Solar Cell. *ACS Appl Mater Interfaces* **8**, 19402–19409 (2016).

96. Bergmann, V. W. *et al.* Real-space observation of unbalanced charge distribution inside a perovskite-sensitized solar cell. *Nat Commun* **5**, 5001 (2014).

97. Xing, G. *et al.* Interfacial Electron Transfer Barrier at Compact TiO2/CH3NH3PbI3 Heterojunction. *Small* **11**, 3606–3613 (2015).

98. Shao, Y., Xiao, Z., Bi, C., Yuan, Y. & Huang, J. Origin and elimination of photocurrent hysteresis by fullerene passivation in CH 3 NH 3 PbI 3 planar heterojunction solar cells. *Nature Communications* **5**, 5784 (2014).

99. Oga, H., Saeki, A., Ogomi, Y., Hayase, S. & Seki, S. Improved Understanding of the Electronic and Energetic Landscapes of Perovskite Solar Cells: High Local Charge Carrier Mobility, Reduced Recombination, and Extremely Shallow Traps. *J. Am. Chem. Soc.* **136**, 13818–13825 (2014).

100. Shi, D. *et al.* Solar cells. Low trap-state density and long carrier diffusion in organolead trihalide perovskite single crystals. *Science* **347**, 519–522 (2015).

101. Comin, R. *et al.* Structural, optical, and electronic studies of wide-bandgap lead halide perovskites. *J. Mater. Chem. C* **3**, 8839–8843 (2015).

102. Leijtens, T. *et al.* Carrier trapping and recombination: the role of defect physics in enhancing the open circuit voltage of metal halide perovskite solar cells. *Energy Environ. Sci.* **9**, 3472–3481 (2016).

103. Yin, W.-J., Shi, T. & Yan, Y. Superior Photovoltaic Properties of Lead Halide Perovskites: Insights from First-Principles Theory. *J. Phys. Chem. C* **119**, 5253–5264 (2015).

104. Gallet, T., Grabowski, D., Kirchartz, T. & Redinger, A. Fermi-level pinning in methylammonium lead iodide perovskites. *Nanoscale* **11**, 16828–16836 (2019).

105. Yin, W.-J., Shi, T. & Yan, Y. Unusual defect physics in CH3NH3PbI3 perovskite solar cell absorber. *Appl. Phys. Lett.* **104**, 063903 (2014).

106. Wei, S.-H. Overcoming the doping bottleneck in semiconductors. *Computational Materials Science* **30**, 337–348 (2004).

107. Du, M. H. Efficient carrier transport in halide perovskites: theoretical perspectives. *J. Mater. Chem. A* **2**, 9091–9098 (2014).

108. Stoneham, A. M. & Itoh, N. Materials modification by electronic excitation. *Applied Surface Science* **168**, 186–193 (2000).

109. Schwanitz, K., Weiler, U., Hunger, R., Mayer, T. & Jaegermann, W. Synchrotron-Induced Photoelectron Spectroscopy of the Dye-Sensitized Nanocrystalline TiO2/Electrolyte Interface: Band Gap States and Their Interaction with Dye and Solvent Molecules. *J. Phys. Chem. C* **111**, 849–854 (2007).

110. Aristidou, N. *et al.* The Role of Oxygen in the Degradation of Methylammonium Lead Trihalide Perovskite Photoactive Layers. *Angew. Chem. Int. Ed. Engl.* **54**, 8208–8212 (2015).

111. Henderson, M. A., Epling, W. S., Perkins, C. L., Peden, C. H. F. & Diebold, U. Interaction of Molecular Oxygen with the Vacuum-Annealed TiO2(110) Surface: Molecular and Dissociative Channels. *J. Phys. Chem. B* **103**, 5328–5337 (1999).

112. Lu, G., Linsebigler, A. & Yates, J. T. The adsorption and photodesorption of oxygen on the TiO2(110) surface. *J. Chem. Phys.* **102**, 4657–4662 (1995).

113. Gonzalez-Elipe, A. R., Munuera, G. & Soria, J. Photo-adsorption and photo-desorption of oxygen on highly hydroxylated TiO2 surfaces. Part 2.—Study of radical intermediates by electron paramagnetic resonance. *J. Chem. Soc., Faraday Trans. 1* **75**, 748–761 (1979).

114. Leijtens, T. *et al.* Overcoming ultraviolet light instability of sensitized TiO 2 with meso-superstructured organometal tri-halide perovskite solar cells. *Nature Communications* **4**, 2885 (2013).

115. Ito, S., Tanaka, S., Manabe, K. & Nishino, H. Effects of Surface Blocking Layer of Sb2S3 on Nanocrystalline TiO2 for CH3NH3PbI3 Perovskite Solar Cells. *J. Phys. Chem. C* **118**, 16995–17000 (2014).

116. Murugadoss, G. *et al.* Light stability tests of methylammonium and formamidinium Pb-halide perovskites for solar cell applications. *Japanese Journal of Applied Physics* **54**, 08KF08 (2015).

117. Kong, W., Rahimi-Iman, A., Bi, G., Dai, X. & Wu, H. Oxygen Intercalation Induced by Photocatalysis on the Surface of Hybrid Lead Halide Perovskites. *J. Phys. Chem. C* **120**, 7606–7611 (2016).

118. Schoonman, J. Organic–inorganic lead halide perovskite solar cell materials: A possible stability problem. *Chemical Physics Letters* **619**, 193–195 (2015).

119. Chen, J. *et al.* Recent progress in stabilizing hybrid perovskites for solar cell applications. *Journal of Power Sources* **355**, 98–133 (2017).

120. Abdelmageed, G. *et al.* Effect of temperature on light induced degradation in methylammonium lead iodide perovskite thin films and solar cells. *Solar Energy Materials and Solar Cells* **174**, 566–571 (2018).

121. Chen, B.-A. *et al.* In Situ Identification of Photo- and Moisture-Dependent Phase Evolution of Perovskite Solar Cells. *ACS Energy Lett.* **2**, 342–348 (2017).

122. Oksengendler, B. L., Ashurov, N. R., Maksimov, S. E., Akhmedov, M. I. & Nurgaliev, I. N. Mechanisms of radiation degradation of solar cells based on organic-inorganic perovskites. *Appl. Sol. Energy* **53**, 326–333 (2017).

123. Juarez-Perez, E. J., Hawash, Z., Raga, S. R., Ono, L. K. & Qi, Y. Thermal degradation of CH3NH3PbI3 perovskite into NH3 and CH3I gases observed by coupled thermogravimetry–mass spectrometry analysis. *Energy Environ. Sci.* **9**, 3406–3410 (2016).

124. Kim, N.-K. *et al.* Investigation of Thermally Induced Degradation in CH 3 NH 3 PbI 3 Perovskite Solar Cells using In-situ Synchrotron Radiation Analysis. *Scientific Reports* **7**, 4645 (2017).

125. Tong, C.-J. *et al.* Uncovering the Veil of the Degradation in Perovskite CH3NH3PbI3 upon Humidity Exposure: A First-Principles Study. *J. Phys. Chem. Lett.* **6**, 3289–3295 (2015).

126. Bass, K. K. *et al.* Influence of moisture on the preparation, crystal structure, and photophysical properties of organohalide perovskites. *Chem. Commun.* **50**, 15819–15822 (2014).

127. Christians, J. A., Miranda Herrera, P. A. & Kamat, P. V. Transformation of the Excited State and Photovoltaic Efficiency of CH3NH3PbI3 Perovskite upon Controlled Exposure to Humidified Air. *J. Am. Chem. Soc.* **137**, 1530–1538 (2015).

128. Noh, J. H., Im, S. H., Heo, J. H., Mandal, T. N. & Seok, S. I. Chemical Management for Colorful, Efficient, and Stable Inorganic–Organic Hybrid Nanostructured Solar Cells. *Nano Lett.* **13**, 1764–1769 (2013).

129. Shirayama, M. *et al.* Degradation mechanism of CH3NH3PbI3 perovskite materials upon exposure to humid air. *Journal of Applied Physics* **119**, 115501 (2016).

130. Deretzis, I. *et al.* Atomistic origins of CH3NH3PbI3 degradation to PbI2 in vacuum. *Appl. Phys. Lett.* **106**, 131904 (2015).

131. Chen, B. *et al.* Impact of Capacitive Effect and Ion Migration on the Hysteretic Behavior of Perovskite Solar Cells. *J. Phys. Chem. Lett.* **6**, 4693–4700 (2015).

132. Agmon, N. The Grotthuss mechanism. *Chemical Physics Letters* **244**, 456–462 (1995).

133. Yang, J., Siempelkamp, B. D., Liu, D. & Kelly, T. L. Investigation of CH3NH3PbI3 Degradation Rates and Mechanisms in Controlled Humidity Environments Using in Situ Techniques. *ACS Nano* **9**, 1955–1963 (2015).

134. Zhao, J. *et al.* Investigation of the Hydrolysis of Perovskite Organometallic Halide CH 3 NH 3 PbI 3 in Humidity Environment. *Scientific Reports* **6**, 21976 (2016).

135. Leguy, A. M. A. *et al.* Reversible Hydration of CH3NH3PbI3 in Films, Single Crystals, and Solar Cells. *Chem. Mater.* **27**, 3397–3407 (2015).

136. Fang, H. & Jena, P. Super-ion inspired colorful hybrid perovskite solar cells. *J. Mater. Chem. A* **4**, 4728–4737 (2016).

137. Niu, G. *et al.* Study on the stability of CH3NH3PbI3 films and the effect of post-modification by aluminum oxide in all-solid-state hybrid solar cells. *J. Mater. Chem. A* **2**, 705–710 (2013).

138. Mosconi, E., Azpiroz, J. M. & De Angelis, F. Ab Initio Molecular Dynamics Simulations of Methylammonium Lead Iodide Perovskite Degradation by Water. *Chem. Mater.* **27**, 4885–4892 (2015).

139. Zhang, L., Ju, M.-G. & Liang, W. The effect of moisture on the structures and properties of lead halide perovskites: a first-principles theoretical investigation. *Phys Chem Chem Phys* **18**, 23174–23183 (2016).

140. Zhu, L. *et al.* Performance enhancement of perovskite solar cells using a La-doped BaSnO3 electron transport layer. *J. Mater. Chem. A* **5**, 3675–3682 (2017).

141. Wang, Q., Chueh, C.-C., Eslamian, M. & Jen, A. K.-Y. Modulation of PEDOT:PSS pH for Efficient Inverted Perovskite Solar Cells with Reduced Potential Loss and Enhanced Stability. *ACS Appl. Mater. Interfaces* **8**, 32068–32076 (2016).

142. Zhang, L. Q. *et al.* Highly efficient and stable planar heterojunction perovskite solar cells via a low temperature solution process. *J. Mater. Chem. A* **3**, 12133–12138 (2015).

143. Seo, J.-Y. *et al.* Boosting the Efficiency of Perovskite Solar Cells with CsBr-Modified Mesoporous TiO2 Beads as Electron-Selective Contact. *Advanced Functional Materials* **28**, 1705763 (2018).

144. Chen, C., Cheng, Y., Dai, Q. & Song, H. Radio Frequency Magnetron Sputtering Deposition of TiO 2 Thin Films and Their Perovskite Solar Cell Applications. *Scientific Reports* **5**, 17684 (2015).

145. Qiu, W. *et al.* An electron beam evaporated TiO2 layer for high efficiency planar perovskite solar cells on flexible polyethylene terephthalate substrates. *J. Mater. Chem. A* **3**, 22824–22829 (2015).

146. Ke, W. *et al.* Perovskite Solar Cell with an Efficient TiO2 Compact Film. *ACS Appl. Mater. Interfaces* **6**, 15959–15965 (2014).

147. Liu, D., Yang, J. & Kelly, T. L. Compact Layer Free Perovskite Solar Cells with 13.5% Efficiency. *J. Am. Chem. Soc.* **136**, 17116–17122 (2014).

148. Zhang, Q., Dandeneau, C. S., Zhou, X. & Cao, G. ZnO Nanostructures for Dye-Sensitized Solar Cells. *Advanced Materials* **21**, 4087–4108 (2009).

149. Tseng, Z.-L., Chiang, C.-H. & Wu, C.-G. Surface Engineering of ZnO Thin Film for High Efficiency Planar Perovskite Solar Cells. *Scientific Reports* **5**, 13211 (2015).

150. Fang, Y., Bi, C., Wang, D. & Huang, J. The Functions of Fullerenes in Hybrid Perovskite Solar Cells. *ACS Energy Lett.* **2**, 782–794 (2017).

151. Yeo, J.-S. *et al.* Highly efficient and stable planar perovskite solar cells with reduced graphene oxide nanosheets as electrode interlayer. *Nano Energy* **12**, 96–104 (2015).

152. Hou, F. *et al.* Efficient and stable planar heterojunction perovskite solar cells with an MoO3/PEDOT:PSS hole transporting layer. *Nanoscale* **7**, 9427–9432 (2015).

153. Hawash, Z., Ono, L. K., Raga, S. R., Lee, M. V. & Qi, Y. Air-Exposure Induced Dopant Redistribution and Energy Level Shifts in Spin-Coated Spiro-MeOTAD Films. *Chem. Mater.* **27**, 562–569 (2015).

154. Yue, Y. *et al.* Enhanced Stability of Perovskite Solar Cells through Corrosion-Free Pyridine Derivatives in Hole-Transporting Materials. *Advanced Materials* **28**, 10738–10743 (2016).

155. Wang, Z. *et al.* High irradiance performance of metal halide perovskites for concentrator photovoltaics. *Nature Energy* **3**, 855–861 (2018).

156. Liu, X. *et al.* 20.7% highly reproducible inverted planar perovskite solar cells with enhanced fill factor and eliminated hysteresis. *Energy Environ. Sci.* **12**, 1622–1633 (2019).

157. Roiati, V. *et al.* Stark Effect in Perovskite/TiO2 Solar Cells: Evidence of Local Interfacial Order. *Nano Lett.* **14**, 2168–2174 (2014).

158. Miller, E. M. *et al.* Substrate-controlled band positions in CH3NH3PbI3 perovskite films. *Phys. Chem. Chem. Phys.* **16**, 22122–22130 (2014).

Chapter 2

Materials and Methods

In this thesis, to understand the phenomenon occurring in perovskite solar cells at the nanoscale, a series of preparation methods and experimental techniques have been used. In order to avoid repetition in the next chapters, the operational principle of the techniques used for characterization will be included in this chapter. Also, the material synthesis and device preparation is described.

2.1 Fabrication Process

The device structure prepared in this work is based on the typical materials used for p-i-n perovskite solar cells, as discussed in **section 1.3.5**: ITO/PEDOT:PSS/Perovskite. However, in some parts of **Chapter 4**, an insulating layer of Al_2O_3 is added after the perovskite deposition in order to avoid degradation due to the characterization technique, which are made in atmospheric conditions

First, transparent and patterned indium-tin-oxide (ITO) substrates (Naranjo substrates, ref. NS1463, 95 nm, ~ 20 Ω.sq) are cleaned thoroughly. The surface is wiped down with soap to remove any microscopic contaminants such as organic compounds, dirt and dust. Then the substrates are ultra-sonicated with detergent, deionized water (15 MΩ/cm^2), acetone and isopropanol for 10 minutes each. They are then dried under a stream of nitrogen gas. Finally, the samples are O_2-plasma cleaned for 5 min. After the cleaning process, a thin layer of PEDOT:PSS is deposited. PEDOT:PSS (Heraeus Clevios P Al 4083) is spin-coated at 5000 rpm for 60 s and baked at 110 °C for 10 min. The final thickness of the PEDOT:PSS layer is around 40 nm. Then, the samples are transferred into an N_2-filled glovebox in order to deposit the $MAPbI_3$ perovskite, see **Fig. 2.1**. At this point, two different synthetic routes were carried out.

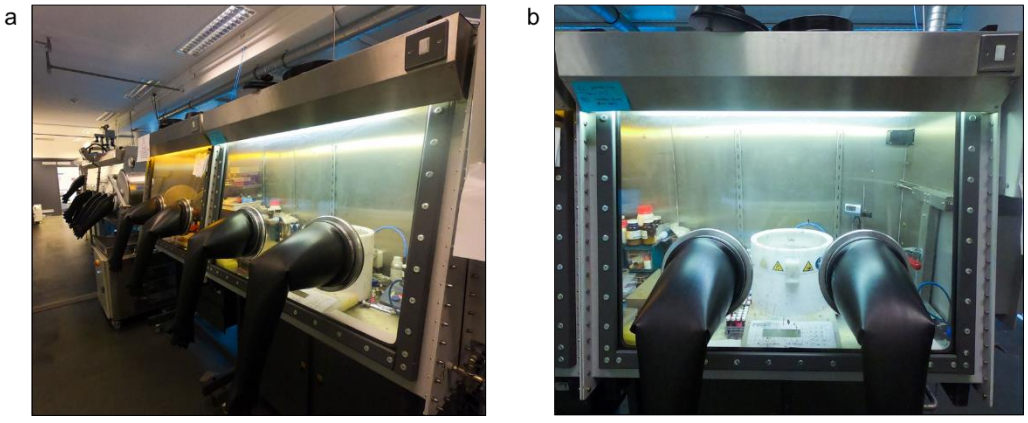

Figure 2.1. *Glovebox used for (**a**) perovskite synthesis and (**b**) deposition.*

To describe how the perovskite films were made, it should be noted that hybrid perovskites can be fabricated and deposited in multiple ways. However, due to the low cost and ease of use of solution processing techniques, they are the preferred deposition techniques and the ones used in this work, **Fig. 2.2a** and **2.2b**. In solution process, the

precursors are dissolved (typical solvents are DMF, DMSO or GBL, but there are many others) and can be deposited via spin-coating in one-step, two-steps, with an antisolvent, etc.[1–7]

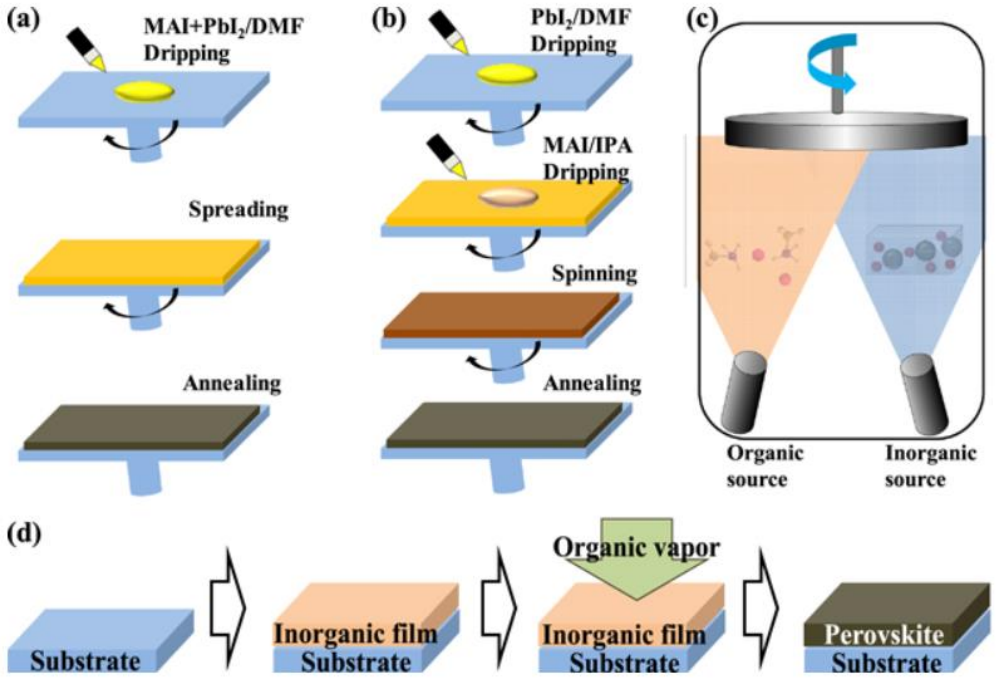

Figure 2.2. *Four perovskite deposition processes: **(a)** one-step precursor deposition, **(b)** two-step sequential deposition, **(c)** dual-source vapour deposition and **(d)** vapour-assisted solution process.*[8]

In one-step deposition, a single solution is used so the solvent(s) should dissolve all the perovskite precursors, organic and inorganic, **Fig. 2.2a**.[1] One-step can become difficult to make for longer organic chains in the perovskite since it would be more difficult to find a good solvent. Same goes for the inorganic part, they are soluble (or stable) with orthogonal solvents. Nonetheless, an optimization of the precursor ratio and the usage of additives makes one-step deposition still a very valid deposition technique. Two-step deposition involves dissolving each precursor individually and spin-coating them sequentially without stopping the spinning, and dropping the second solution at some point of the spin-coating process, **Fig. 2.2b**. It allows for a better control of the final thickness, morphology and it shows high uniformty.[2] After the deposition, the films are then annealed. Other techniques used in literature but in a lesser extent are vapour process and hybrid processes. In vapour process deposition, perovskites are deposited via evaporation and annealing (as in **Fig. 2.2c** or **2.2d**).[9] This technique is usually done in

vacuum and it is especially useful for growing oriented thin films. However, it is not as cheap as solution process and it is limited when depositing different perovskites. The so-called "hybrid" processes are a combination of both, solution and vapour processes.[8]

$CH_3NH_3PbI_3$ perovskite can be formed by different chemical reactions depending on the precursor materials used. The most popular precursors are methylammonium iodide (MAI) and a lead source, typically lead iodide (PbI_2), **Eq. 2.1**. Nonetheless, the perovskite formation can be achieved with other anions as a lead source, or even with a mixture of anions.[10] Zhang *et al.* studied the role of different anions in the lead precursor and found that they affect the crystal growth kinetics, film morphology and device performance.[11] The typical anion for the PbX_2 precursor is iodide. However, lead acetate ($PbAc_2$) was found to accelerate the crystal growth, **Eq. 2.1**. In addition, the perovskite films can be either p-type or n-type depending on the ratio between the precursors, as in **Fig. 2.3**. With a PbI_2-rich (PbI_2-deficient) film, the perovskite will be n-doped (p-doped), respectively.[12]

$$PbAc_2 + 3\,CH_3NH_3I \longrightarrow CH_3NH_3PbI_3 + 2\,CH_3NH_3Ac \qquad (2.1)$$

$$PbI_2 + CH_3NH_3I \longrightarrow CH_3NH_3PbI_3$$

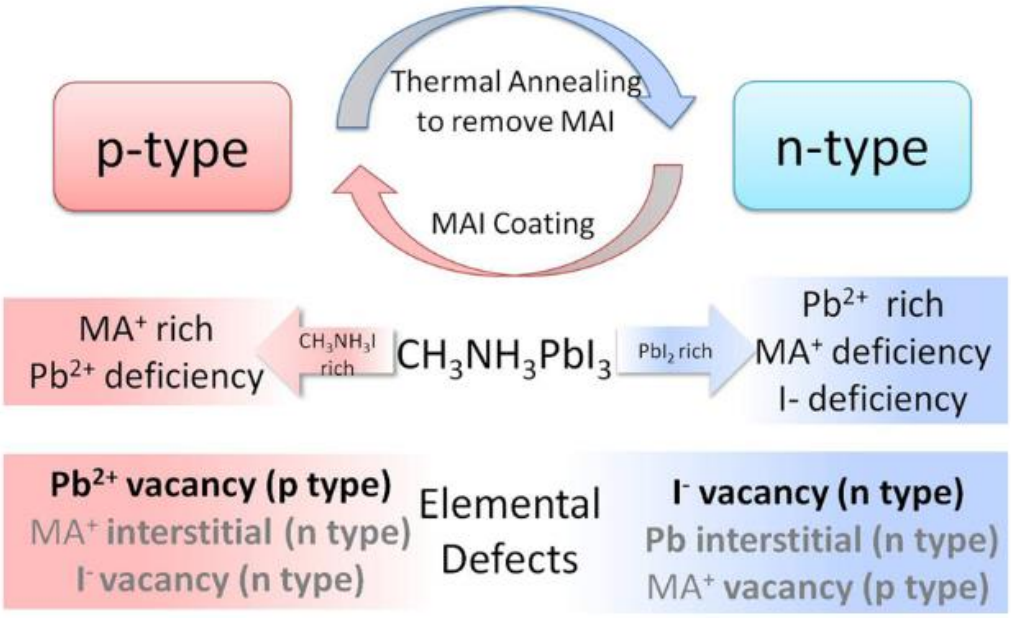

Figure 2.3. *Schematic conductivity type conversions in perovskite films by excess CH_3NH_3I (left side) or excess PbI_2 (right side). Possible point defects in perovskite films caused by composition variation were illustrated correspondingly. The elemental defects in grey colour are less-likely to form in the films.*[12]

In this work, two routes were carried out to synthesize $MAPbI_3$. The first one (MAPI-$PbAc_2$ route, described below) was developed by Zhang *et al.* to increase the grain size and to grow the perovskite with less defects.[13] The second one (MAPI-PbI_2 route, described below) is the most used synthesis route for $MAPbI_3$ perovskite and served as a reference route.[14] The purpose is to analyse the electronic differences in the MAPbI3 behaviour (especially at the surface) when using different precursor materials and/or process techniques.

Solution process was performed in one-step for the two $CH_3NH_3PbI_3$ synthesis routes, the materials required for their synthesis are summarized in **Table 1**. While one route involves the usage of an additive in the precursor solution, the other route is done through an anti-solvent method to improve the morphology. The first synthesis route was made using MAI and $PbAc_2$ as precursor materials and were mixed prior to depositing them in one-step, this perovskite will be referred to as $MAPbI_3$-$PbAc_2$.

MAI (Greatcell Solar) and $PbAc_2 \cdot 3H_2O$ (99.999% Merck) were used in a 3:1 molar ratio dissolved with anhydrous N,N-Dimethylformamide (DMF, 99.9% Merck), with a final concentration of 0.5 M. Hydrophosphorous acid (HPA, 50% Merck) was added with a HPA/$PbAc_2 \cdot 3H_2O$ molar ratio of 11%. HPA is used to enlarge the grain size and to reduce the non-radiative recombination centres, being 11% the optimal molar ratio.[13] The solution was then spin-coated at 2000 rpm for 60 s, left at room temperature for 10 min. and heated at 100 ºC for 5 min.

In the second route, MAI and PbI_2 were used as precursors and were deposited in one-step using an anti-solvent method, this perovskite will be referred to as $MAPbI_3$-PbI_2.[14] The anti-solvent consists of a solvent that speeds up the nucleation via the creation of an instantaneous local supersaturation on the spinning substrate. This solvent is usually dripped after some time while the substrate is spinning, resulting in the formation of an intermediate phase like MAI-PbI_2-DMSO.[15] The intermediate phase prevents the fast reaction between MAI and PbI_2 precipitation and allows for a uniform morphology. In this thesis, the perovskite was made by mixing lead iodide PbI_2 (99% Merck) and MAI in DMF (and 1.5% of the total volume with DMSO as additive) with a 1:1 molar ratio and a final concentration of 1.5 M. The solution was spin coated at 5000 rpm for 30 s while 200 µL of ethyl acetate is dropped into the sample after 10 s to control the end point of the growth process.[14,16] The final thickness for both perovskite routes is of around ~ 300 nm.

Table 1: *Materials used for the preparation of MAPI-$PbAc_2$ and MAPI-PbI_2 perovskites.*

MAPI-$PbAc_2$ route	**MAPI-PbI_2 route**
MAI (Greatcell Solar)	MAI (Greatcell Solar)
$PbAc_2 \cdot H_2O$ (99.999% Merck)	PbI_2 (99% Merck)
HPA (50% Merck)	DMF (Merck)
DMF (Merck)	DMSO (Merck)
	Ethyl Acetate (Merck)

Additionally in **Chapter 4**, perovskite devices were characterized with an AFM exposed to air. Therefore, an insulating layer of aluminium oxide (Al_2O_3) was deposited on top of the perovskite layer. Using an atomic layer deposition (ALD) chamber, trimethylaluminium ($Al(CH_3)_3$, 97% Sigma Aldrich) and water were injected in a series

of pulses, leading to a final thickness of 5 nm. The chamber was set to 200 ºC and the chuck at around 55 ºC. The pressure in the vacuum chamber was 1.1 torr.

2.2 Characterization Techniques

2.2.1 X-Ray Diffraction

X-ray diffraction (XRD) is a method used to determine the structural properties of the crystals based on the scattering of light. Since amorphous materials are not organized in a periodic array, they do not scatter light coherently. In a crystal structure each atom is arranged in a periodic array and, when an X-ray interacts with it, a certain amount of energy is absorbed. Electrons occupy certain energy states around an atom, but the absorbed energy is not enough to release the electron, the energy must then be re-emitted in a form of a new x-ray with the same energy as the original, this process is known as elastic scattering. At specific x-ray incident angles, the scattered x-rays can constructively interfere; this is called diffraction and results in a peak in intensity seen in the XRD diffractogram. The diffracted peaks can be associated with different planes in an atom structure and they are named after the (hkl) Miller indices. In the XRD set-up, the sample under test is exposed to a beam of x-rays with a given incident angle θ as in **Fig. 2.4**. The diffracted light is received by the X-ray detector in a 2θ angle. Diffraction is used to measure the distance between the atom planes.

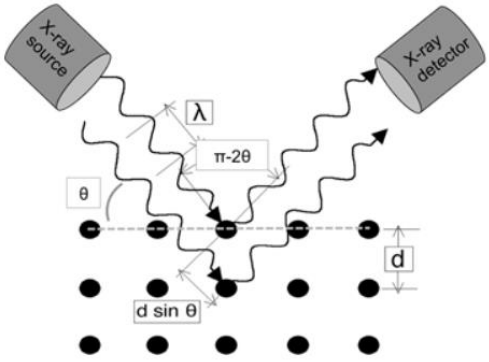

Figure 2.4. *Schematic representation of the Bragg's equation.*

The Bragg's law relates the crystal spacing d_{hkl} with the x-ray wavelength λ and the angle of incidence by the following expression:

$$n\,\lambda = 2\,d\sin\theta \tag{2.2}$$

where n is an integer known as the order or reflection. The crystal geometry can be determined from the crystal spacing measured by XRD. XRD has been used in this work to determine the crystalline structure of the $MAPbI_3$ perovskite (in **Chapter 3**) and to determine if any change occur in the structure when exposing the $MAPbI_3$ perovskite to water vapour (in **Chapter 5**). From the crystal spacing, the lattice distances can be also determined following the expression for a given geometry. Perovskites use to be in a tetragonal configuration as it is the case for the perovskite used for this work:

$$\frac{1}{d_{hkl}^2} = \frac{h^2+k^2}{a^2} + \frac{l^2}{c^2} \tag{2.3}$$

X-ray diffractograms were obtained using a Panalytical Empyrean XRD diffractometer operating with the Cu $K_{\alpha 1}$ (α = 0.1542 nm) source.

2.2.2 X-Ray Photoelectron Spectroscopy

In X-ray photoelectron spectroscopy (XPS), an x-ray is sent to the sample surface with enough energy to eject an electron (photoelectron) as in **Fig. 2.5**. The threshold energy ν_0 at which the electron can be emitted is determined by its frequency. At higher frequencies ν, the emitted electrons will possess higher kinetic energies $KE_{electron}$,

$$KE_{electron} = h\nu - h\upsilon_0 \tag{2.4}$$

Knowing the $KE_{electron}$ and the energy of the incident photon, the binding energy (BE) can be calculated as

$$BE = h\nu - KE_{electron} - \phi_{spec} \tag{2.5}$$

where ϕ_{spec} is the spectrometer work function. The system is operated under high vacuum (< 10^{-9} torr) to avoid surface reactions or contamination. All orbital levels except the s levels are doublets with the two possible states having different binding energies. However, for p, d and f peaks, two peaks are observed (spin orbital splitting). The XPS technique was used to understand the chemical composition of the perovskite sample surface (in **Chapters 3** and **5**). XPS measurements were carried out with a PHI

5300ESCA PerkinElmer spectrometer and the recorded spectra were calibrated with the C 1s peak (285.1 eV).

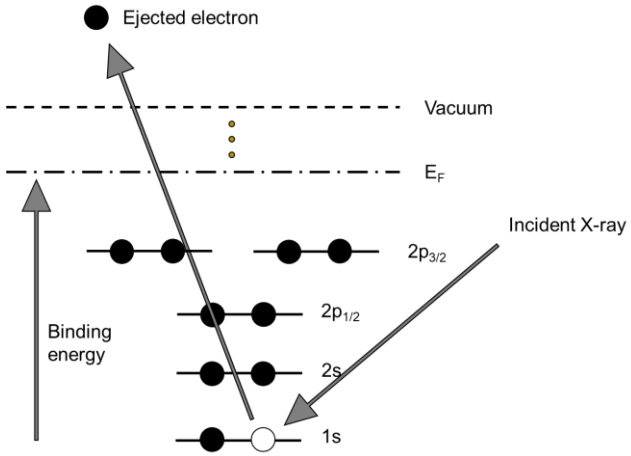

Figure 2.5. *Photoemission process in XPS. Black dots represent electrons and the bars represent energy levels in a given atom.*

2.2.3 UV Visible Spectroscopy

In UV-Visible spectroscopy, a light beam is directed to an absorbing material and then the amount of absorbed (or transmitted) light is determined. The absorbed light depends on the thickness of the material and the concentration following the expression:

$$A = \alpha\, c\, d \tag{2.6}$$

where A is the absorbance, α is the absorption coefficient, c is the concentration of the material and d is the length of the material. The spectrometer shoots light in a range of wavelengths of light, obtaining an absorption spectrum. From the spectrum, the absorption peak at which the material absorbs light can be determined. When the light is absorbed, the electron occupying the valence band is promoted to the conduction band, therefore, a certain amount of energy is absorbed:

$$E = h\nu = h\,\frac{c}{\lambda} \tag{2.7}$$

where h is the Planck constant, ν is the frequency of light, c is the speed of light and λ is the wavelength. From this relationship, the optical bandgap of the material can be calculated. However, for materials with a direct allowed transition in the bandgap, the optical bandgap E_G could be determined with the Tauc plot (see **Fig. 2.6**) by the equation:

$$\alpha h\gamma = A(h\nu - E_G)^{1/2} \tag{2.8}$$

UV-visible absorption spectra was taken with a Lambda 650 S PerkinElmer spectrometer.

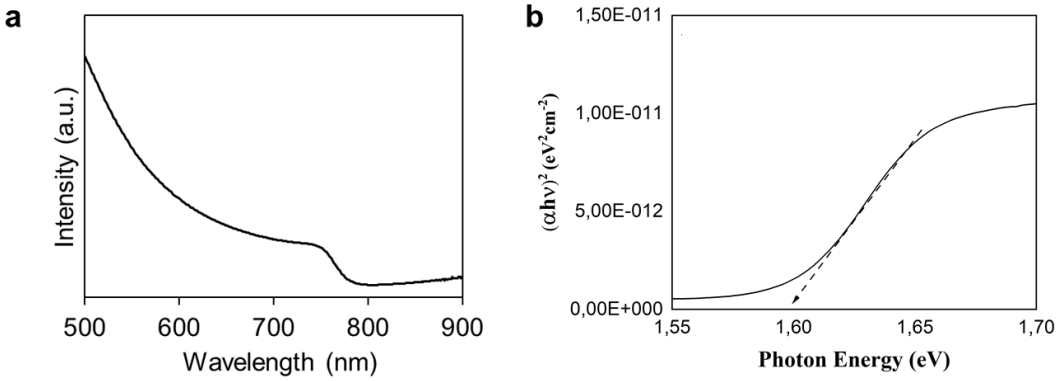

Figure 2.6. UV-Vis spectra and *Tauc plot for the MAPI-PbAc$_2$ perovskite with an optical bandgap estimated around 1.59 eV.*

2.2.4 Atomic Force Microscopy - Principle

Atomic Force Microscopy (Multimode AFM from Bruker) is used to provide a topographical image at the nanoscale of the surface under test. AFM probes the forces between the probe and the surface at short distances (between 0 and 10 nm). The scheme of an AFM can be seen in **Fig. 2.7**, and it is divided into different components. The AFM probe is located at the end of a cantilever, which has a given spring constant (0.1 to 20 N/m typically). The spring constant affects directly the force applied to the sample; soft samples could be damaged with probes with high spring constant. The motion of the probe is controlled by a piezoelectric actuator and a feedback loop maintaining the amplitude modulation to a user-defined value. The piezoelectric actuator vibrates at the resonance frequency of the cantilever under an applied ac bias voltage, it will produce the cantilever oscillation. The light of a laser is projected on the back of the cantilever, which is reflected to a four-quadrant photodiode, **Fig. 2.7**.

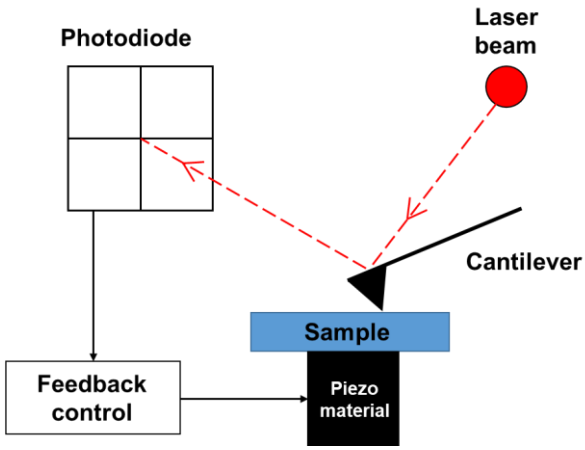

Figure 2.7. *Scheme of an AFM set-up.*

The photodiode detects the motion of the cantilever and a feedback loop maintains the position of the laser on the photodiode by adjusting a voltage sent to the piezoelectric tube supporting the sample. The probe undergoes Van der Waals forces when closer to the sample surface. Indeed, several methods of operation can be distinguished: contact, non-contact and tapping mode.

In contact mode (**Fig. 2.8a**), the probe touches the sample surface with a given force and the probe-surface repulsive forces deflect the cantilever. The force applied to the probe and its deflection are proportional according to Hooke's law ($F = -k \cdot \delta z$, where F is the applied force, δz is the deflection distance and k is the spring constant of the cantilever). Through a feedback loop, the applied force (so the deflection) is maintained. This may be a destructive technique for soft surfaces. In contrast, in non-contact mode (**Fig. 2.8b**), an ac signal is sent to the piezoelectric material at, or close to, the resonance frequency of the cantilever. The probe oscillates above the surface sample at a given distance. By monitoring the shift of the resonance frequency caused by the attractive forces and maintaining the distance to the surface with a feedback loop, the morphology of the surface can be recorded. It is important to note that the gradient of attractive forces is smaller than the gradient of repulsive forces, meaning that the cantilevers with high resonance frequencies are preferred for a better sensitivity. In tapping mode (**Fig. 2.8c**), the cantilever is kept at a certain distance from the sample and, it oscillates in a given amplitude touching the sample. The amplitude is controlled by an ac signal applied to the piezo at, or close to, its resonance frequency. The amplitude of oscillation depends on the interaction between the probe and the surface. It is kept constant though a feedback loop,

which allows for a non-destructive scanning of the surface under test. The measurements are based on electrostatic forces, establishing a direct relationship between the force of the probe and the sample. The relationship between force and probe-sample distance can be seen in **Fig. 2.8d**.

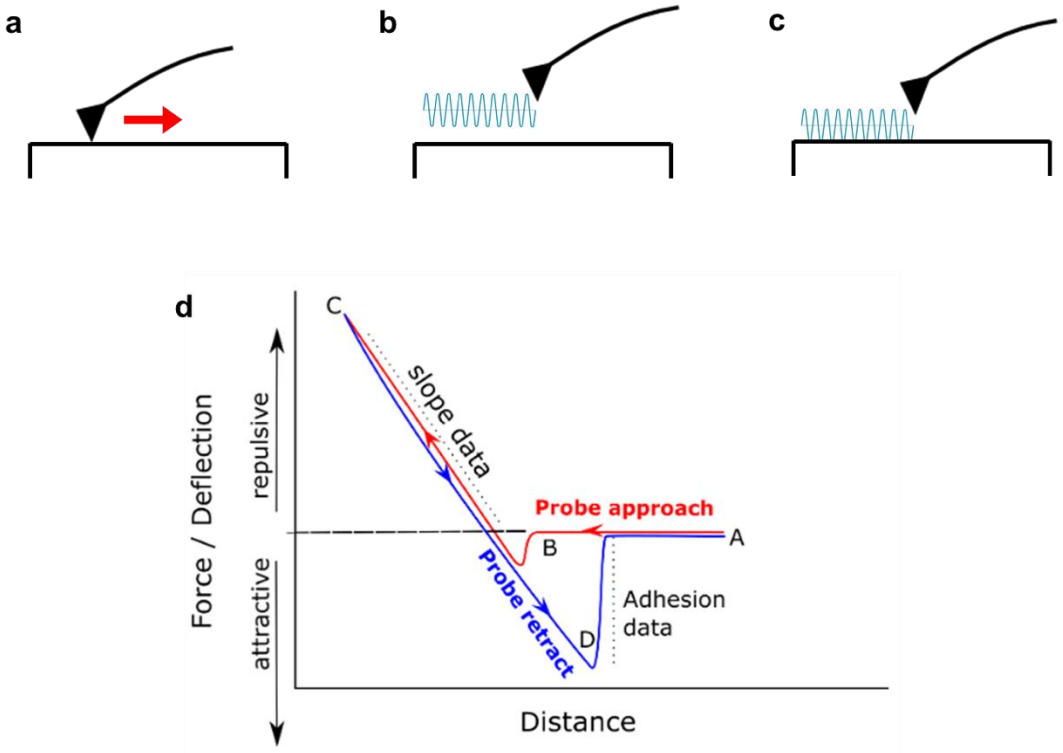

Figure 2.8. *Atomic force microscopy modes: (**a**) contact, (**b**) non-contact or frequency modulated AFM and (**c**) Tapping mode or amplitude modulated AFM. (**d**) Typical force-distance curve in AFM.*

The AFM used in this thesis (Bruker Multimode AFM) was the same for conductive AFM and Kelvin Probe Force Microscopy measurements. It was operated in an inert environment, see **Fig. 2.9**.

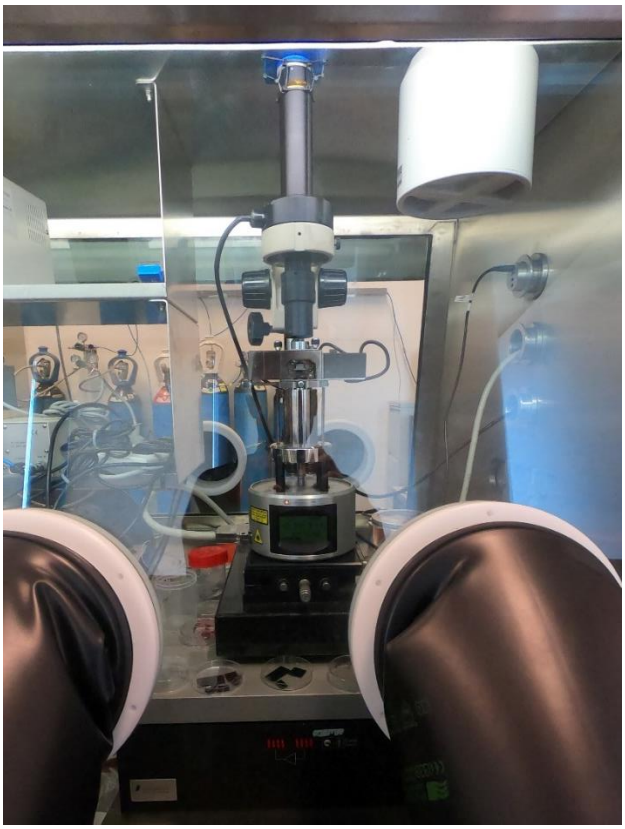

Figure 2.9. *Bruker Multimode AFM inside a N_2-filled glovebox.*

2.2.5 Conductive AFM

Conductive AFM (C-AFM) is typically done in contact mode and the probe used for this mode of operation has a conductive coating. **Fig. 2.10** shows a schematic of the C-AFM set-up. When the probe is in contact with the sample surface, a dc voltage can be applied, then, the current flowing between the conductive probe and the sample is recorded. The electrodes are the probe itself and the metallic sample holder. Note that even if the silver paste is in contact with the perovskite layer, the probe is far enough to avoid any eventual lateral current.[17] The current response signal is recorded simultaneously with the topography of the sample. An external amplifier module (TUNA module from Bruker) is necessary to detect the current with high sensitivity. In this mode, it is also possible to record I-V spectroscopy on specific areas however, the signal to noise ratio use to be high. Nonetheless, since the current signal from the imaging is reliable enough and constant throughout the measurement, several images done at the same location and different voltages were done in order to reconstruct I-V curves (data presented in **Chapter 3**).

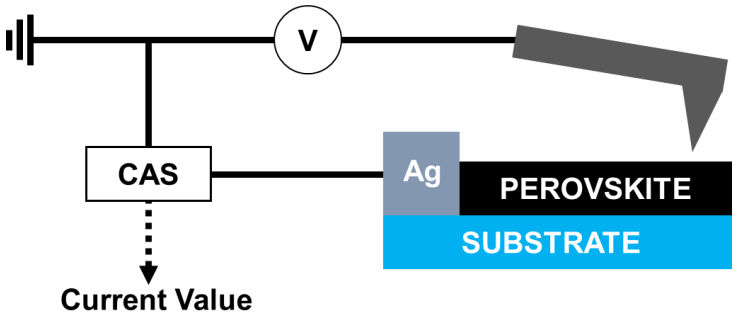

Figure 2.10. *Schematic of the C-AFM set up. CAS stands for current amplifier setup.*

C-AFM measurements were carried out with a Bruker Multimode AFM and an Extended TUNA (Bruker) module for detection between 100 fA and 10 nA. The set-up was used under a nitrogen atmosphere to prevent our samples reacting with the ambient humidity, see **Fig. 2.9**. The probes used were made of $PtIr_5$ (SCM-PIT-V2 from Bruker) with a spring constant of 3 N/m. Also, when preparing the samples for C-AFM measurements, Ag paint was added between the substrate and the sample surface so the current can flow through the sample to the probe when applying voltage to the sample.

Another way to track the current in C-AFM is with PeakForce tunnelling mode (PF-TUNA). It is an intermittent contact AFM method with force control, which prevents damaging the sample. The probe is brought into contact and the system records the force between the probe and the sample at any point, **Fig. 2.11**. Instead of applying frequencies near or at its resonance frequency (as in tapping mode or non-contact mode), a low frequency oscillation is applied to the probe (~ 1 KHz). The resulting force-distance curve is recorded and readjusted to match the force setpoint (named Peak Force setpoint). Applying a potential difference between the probe and the sample, it allows for measurement of electrical properties. In PF-TUNA, the average current, flowing between the probe and the sample is derived along each measured force-distance curve. PF-TUNA shows an advantage over tapping or contact modes for electrical measurements since the signal can be measured at any point of the probe-to-sample distance, see **Fig. 2.11**. The "TUNA current" or the average current for the whole force-distance curve, point A to E in **Fig. 2.11**. The "contact current" or the average current when the probe is in contact with the sample surface, points B to D in **Fig. 2.11**. The "peak current" or the current obtained at maximum force point of the force-distance curve (point C in **Fig. 2.11**).[18] In this work, PF-TUNA mode has been used to make current maps of the perovskite layers and the signal included in the results is obtained from the maximum force point, point C

in **Fig. 2.11**. PF-TUNA allows for a better spatial resolution compared to contact AFM, what translates into a better electrical contrast between domains.

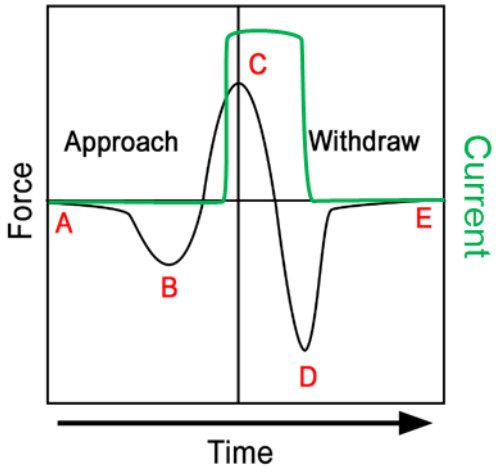

Figure 2.11. *Force curve in Peakforce mode. Red letters represent the important information points on the curves.*

2.2.6 Kelvin Probe Force Microscopy

Kelvin Probe Force Microscopy (KPFM) is normally used for electrical characterization of interfaces (when using a cross section) and surfaces in the dark or illumination.[19] Is based on the Fermi energy alignment. The Fermi energy, E_F, is the energy level where the probability to find an electron with 50 % probability. The energy level occupation by the electrons in the CB and VB is described by the Fermi-Dirac distribution. The difference between the vacuum energy level and the E_F is the so-called work function (WF). When the probe is brought close to the perovskite surface, the E_F of the material under test and the probe align creating an electric field between them, as shown in **Fig. 2.12**.[20] Then, the vacuum levels for the probe and the sample are not the same anymore, creating a potential difference (V_{CPD}). A dc voltage (V_{dc}) is then applied between the probe and the sample to nullify the electric field created by the potential difference, this dc voltage corresponding to the V_{CPD}. As the AFM probe is sensitive to the electrostatic force induced by the tip-sample interactions, KPFM results in a high sensitive technique for CPD determination.

$$V_{CPD} = \frac{\phi_{tip} - \phi_{sample}}{-e} \tag{2.9}$$

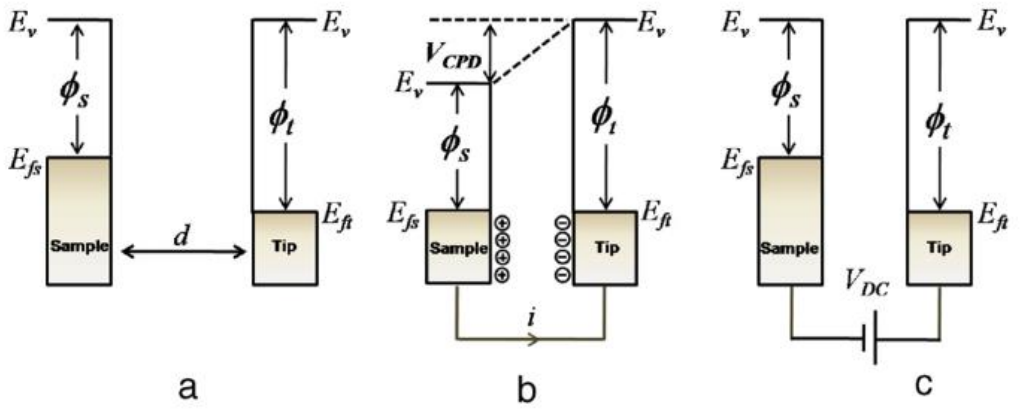

Figure 2.12. *Electronic energy levels of the sample and AFM tip for three cases: (**a**) tip and sample are separated by distance d with no electrical contact, (**b**) tip and sample are in electrical contact, and (**c**) external bias (V_{dc}) is applied between tip and sample to nullify the CPD and, therefore, the tip-sample electrical force. E_v is the vacuum energy level. E_{fs} and E_{ft} are Fermi energy levels of the sample and tip, respectively.*[21]

The electrostatic force between the tip and the sample (F_{elec}) in the z direction (vertical direction to the sample surface) is given by

$$F_{elec}(z) = -\frac{1}{2}\Delta V^2 \frac{dC(z)}{dz} \tag{2.10}$$

where dC/dz is the capacitance gradient between the probe and the surface and ΔV is the difference between the voltage applied to the probe and V_{CPD},

$$\Delta V = V_{dc} - V_{CPD} + V_{ac}\sin(\omega t) \tag{2.11}$$

being V_{ac} the ac voltage with a drive angular frequency ω. Then, introducing **Eq. 2.11** into **Eq. 2.10**, the electrostatic force dependant on whether the bias is applied to the sample or to the probe is expressed as,

$$F_{elec}(z,t) = -\frac{1}{2}[V_{dc} - V_{CPD} + V_{ac}\sin(\omega t)]^2 \frac{dC(z)}{dz} \tag{2.12}$$

which can be divided into three components:

$$F_{dc} = -\frac{dC(z)}{dz}\left[\frac{1}{2}(V_{dc} - V_{CPD})^2 + \frac{1}{4}V_{ac}^2\right] \tag{2.13}$$

$$F_{\omega} = -\frac{dC(z)}{dz}(V_{dc} - V_{CPD})\,V_{ac}\sin(\omega t) \tag{2.14}$$

$$F_{2\omega} = \frac{dC(z)}{dz} \frac{1}{4} V_{ac}^2 \cos(2\omega t) \quad (2.15)$$

being **Eq. 2.13** the force of a constant deflection of the cantilever, **Eq. 2.14** the force of an oscillation ω and it is used to measure the magnitude of V_{CPD}. Finally, **Eq. 2.15** describes an oscillation twice the applied frequency and it is usually used for capacitance measurements.[22] Concerning the determination of the V_{CPD}, it is necessary to determine the difference between V_{dc} and V_{CPD}. For this purpose, a lock-in amplifier is used in order to extract an electrical force component at the angular frequency ω. Then, a V_{dc} equal to V_{CPD} is applied, nullifying the output signal from the lock-in. Therefore, the CPD (and also the work function) can be determined all over the surface.

KPFM can be operated in AM (AM-KPFM) or FM modes (FM-KPFM) as in **Fig. 2.13**. In AM mode (**Fig. 2.13a**), the cantilever is excited by a bias sent to the tip with a driving frequency close to the resonance frequency of the cantilever. The CPD is determined from the F_ω, measured from the amplitude of oscillation of the probe. Through a PID feedback loop the probe bias is adjusted so the amplitude of oscillation remains minimized, hence the electrostatic force is nullified. The downside of this method of detection is that it measures the all the forces near the probe. Therefore, interactions of the bulk cone from the probe and the cantilever with the surface may be included in the CPD measurements. V_{CPD} is an averaged value, hence decreasing the resolution of the measurement. In FM mode (**Fig. 2.13b**), the cantilever is mechanically shaken at its resonance frequency and, at the same time, an ac bias with low frequency is sent to the tip. Then, due to the electrostatic interaction, sidebands appear at $\omega_0 \pm \omega$ (**Eq. 2.14**) and $\omega_0 \pm 2\omega$ (**Eq. 2.15**). A phase-locked loop is used to measure the frequency shift induced by the perturbation caused by the electrostatic force gradient. A lock-in amplifier is also used to isolate the low frequency electrostatic component. Here, the interaction is confined to the electrostatic forces coming only from the probe apex, which offers an improved resolution compared to AM-KPFM. The main drawback is that FM-KPFM has a lower sensitivity than AM-KPFM and higher ac voltages are necessary, what can make a perturbation in the tip-sample interaction.

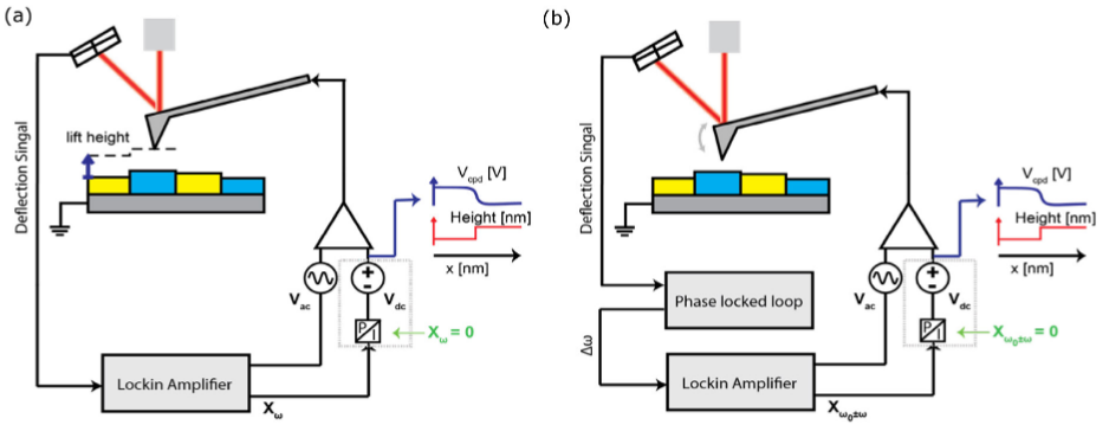

Figure 2.13. *Schematic diagram of KPFM system showing (**a**) AM and (**b**) FM mode.*[23]

In this thesis, FM-KPFM was operated in non-contact mode using a Multimode 8 Atomic force microscope (Bruker) equipped with a Nanoscope V and coupled to a NANONIS (Specs) external controller, see the connections used for this thesis in the schematics on **Fig. 2.14**. The ac voltages required for our samples were relatively low, ~ 1 V, therefore, the main drawback about voltage issues before mentioned for FM mode were not that important for our measurements. The topography was recorded in non-contact mode by tuning the probe at the resonant frequency of the cantilever (around ~ 75 kHz), using PPP-EFM (Nanosensors GmbH) metal coated ($PtIr_5$) etched Si probes. The frequency shift was typically set in a range between 10 to 30 Hz, allowing a constant amplitude of oscillation, see **Fig. 2.15**. V_{CPD} measurements were measured by sending an ac voltage to the tip at ~ 1 kHz. The electrostatic force gradient, created between the probe and the sample and the applied ac voltage, creates sidebands next to the resonance frequency. It is possible to nullify the force gradient at 1ω applying a dc voltage to the sample and with a feedback loop, see **Eq. 2.13**. V_{CPD} maps were systematically calibrated by measuring the V_{CPD} of a highly ordered pyrolytic graphite surface (HOPG), with a well-known WF of 4.65.[24]

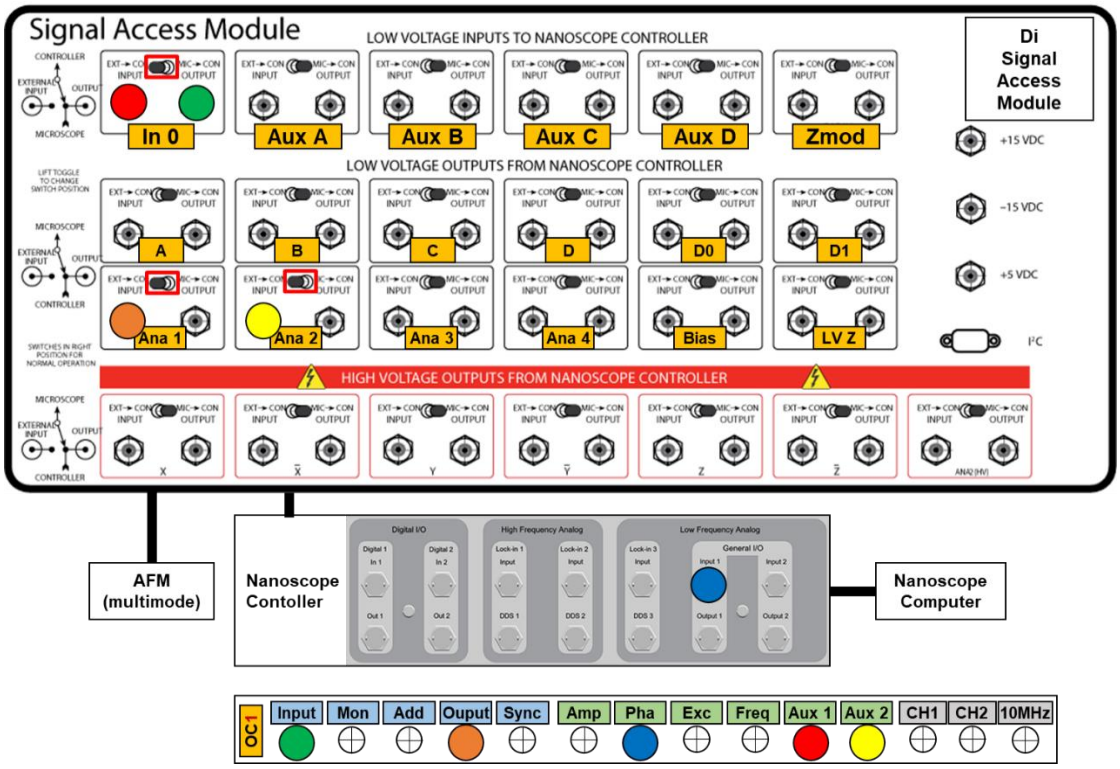

Figure 2.14. *Connections between the AFM Multimode, the Signal Access Module, the Nanoscope controller, the Oscillation Contol 1 (OC1) and the Nanoscope computer.*

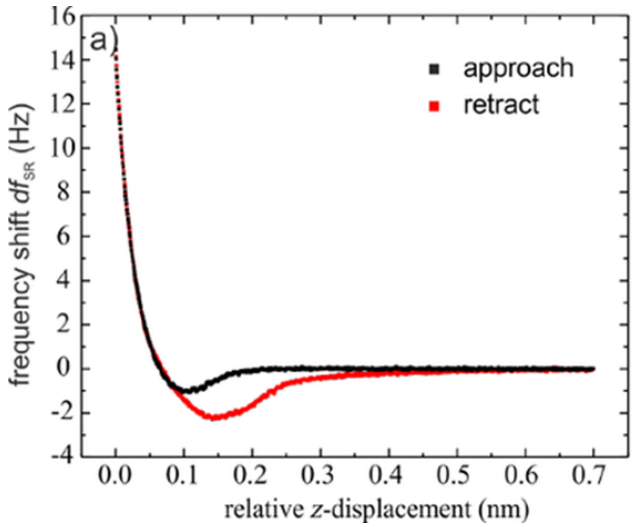

Figure 2.15. *Variation of the frequency shift with the probe-sample distance.*[25]

2.2.7 Scanning Microwave Microscopy

In order to measure the capacitive behaviour of perovskites at the nanoscale, Scanning Microwave Microscope (SMM) was used. SMM is composed by a vector network analyser (VNA) and connected to the AFM head by a coaxial cable. Several techniques have been proposed to perform measurements using SMM.[26–28] Since the wavelength of microwaves is in the range of cm and the thickness of the device under test (DUT) is in the range of nm, the SMM probes the interaction in the quasi-static near-field. In this work, the VNA is used as both, a wavelength source and a detection system. The VNA normally contains a radio frequency source generator (RF), a splitter, a detector and a digital processor. It measures the amplitude and phase magnitudes of small reflected electrical signals. The SMM used in this work operates from 2 to 18 GHz (AT-SMM from Keysight Technologies). **Fig. 2.16** shows the diagram of a VNA. The VNA splits the generated wave in two, one wave is used as the reference signal and the other is sent to the DUT, referred to as the incident wave. The reflected wave is directed to the measurement channel. At the source side, an attenuator gives the ability to change the output power depending on the response of the DUT.

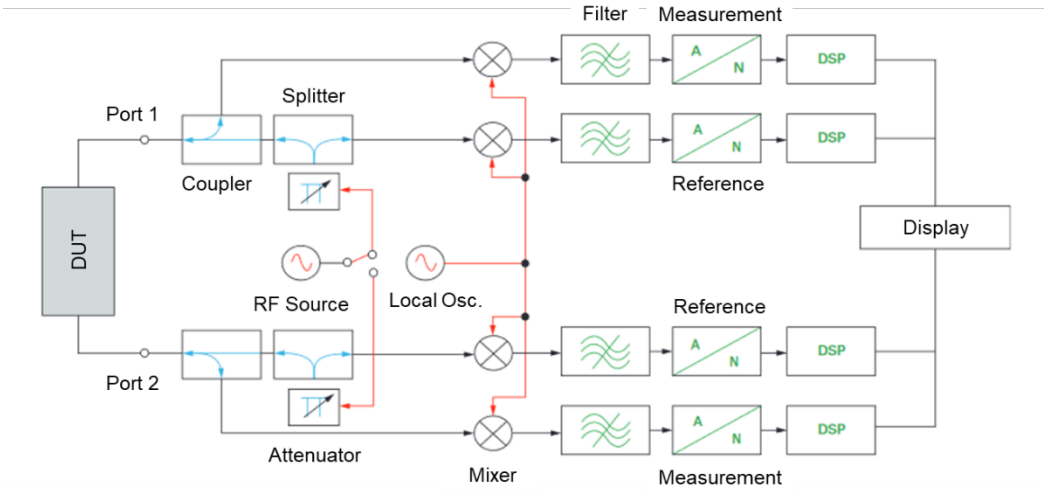

Figure 2.16. *Scheme of a two port VNA.*

These signals are then referenced around an intermediate frequency by means of a mixer and a local oscillator. They are then digitalised and processed. The ratio between the incident wave *a* and the reflected wave *b* represents the reflection coefficient Γ as:

$$\Gamma = \frac{b}{a} \tag{2.16}$$

However, the reflection coefficient is measured by the VNA in terms of S-parameters. Therefore, the VNA measures the so-called S_{11} coefficient. The S_{11} is a complex value, varies with the operating frequency and includes information about the amplitude and phase of the measured wave. To define the S-matrix, we need to take into account the incident waves generated in the port of the VNA (incident wave *a*) and the output wave (or reflected *b* wave). Then we define S_{11} as the response of port 1 due to the incident signal in port 1. This nomenclature is especially useful when using two or more ports in the VNA system. Therefore, Γ (or S_{11}) measures intrinsic properties of the DUT such as impedance, capacitance and conductance. Since the probe creates an electric field, the conductivity and dielectric constant of the material can be in principle extracted. Microwave systems use a standard impedance, Z_{ref} = 50 **Ω**, as a reference. Γ can be expressed as a function of the local (where waves a and b are measured) impedance as:

$$\Gamma = S_{11} = \frac{Z_{DUT} - Z_{ref}}{Z_{DUT} + Z_{ref}} \tag{2.17}$$

With a MOS structure where there is a dielectric layer on top of the semiconductor material, the resistance is probably high enough to consider that the capacitance variations take over. In addition, since the measurements are done at the nanoscale, the capacitance is in the order of aF ($C = \varepsilon \cdot A/d$, where ε is the dielectric constant, A is the area of measurement and d is the thickness). Therefore, the measured impedance range is in the order of MΩ. There is an important mismatch between the impedance of the VNA and the high impedance of the DUT. This means that the measurements done for Z_{DUT} are far from the Z_{ref}, lowering the measurement resolution.[29] To overcome this limitation, a 50 **Ω** lumped resistance is added to the AFM probe holder. The lumped resistance absorbs most of the incident signal, reducing the reflection coefficient to a 0 value. This system allows for accurate measurements for DUT with high impedance in parallel to the 50 **Ω** resistor. In addition, the sensitivity is increased with two amplifiers, which increase the magnitude of incident and reflected waves. One of the drawbacks of this SMM system is the limited range of measurable DUT impedances, only high Z_{DUT} impedances can be accurately measured. Another drawback is the dependence on the cable length connecting the resistor with the AFM tip, which limits the range of frequencies that can be used.[30] Since it is located at a given distance from the DUT, the cable length is L = n (λ/2) (where λ is the wavelength and n is an integer), the resistor can be considered to be connected to the sample.

A better approach is to use an adjustable interferometer instead, as in **Fig. 2.17**.[31] **Fig. 2.17** represents the SMM configuration with a VNA (PNA in the scheme) and the AFM represented by the "SMM probe" in the scheme. Here, when the wave is split in two, the reference signal is adjusted in magnitude by the variable attenuator and then combined with the reflected wave *b* (or a_{ref} in the scheme) in a different point of the circuit (Mach-Zehnder interferometer model). At this point, regardless of the impedance magnitude, the resulting wave can be nullified with the attenuator. With the cable length used in our set-up, the interference occurs more or less every 98.1 MHz, so the interference can be adjusted in a range of ± 50 MHz. This allows for a wider range of frequency operation compared to the method with a lumped resistance. Finally, the wave is amplified before being collected by the receiver.

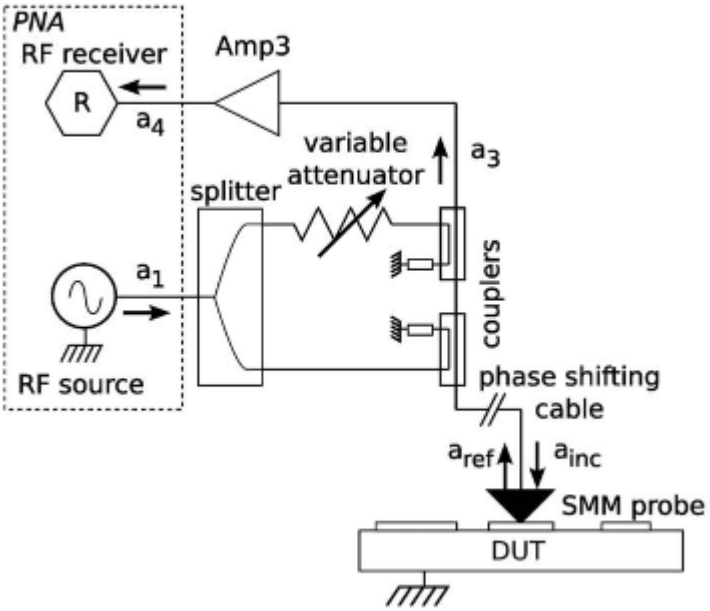

Figure 2.17. *SMM set-up integrating an adjustable microwave interferometer based on a March-Zender configuration.*[31]

Two SMM systems were used through the realization of this thesis. One of them consisted of an SMM made by the IEMN institute, and compatible with an SEM (TESCAN) **Fig. 2.18a**. The other one consisted of a commercial SMM 5600LS provided by Keysight Technologies, **Fig. 2.18b**.

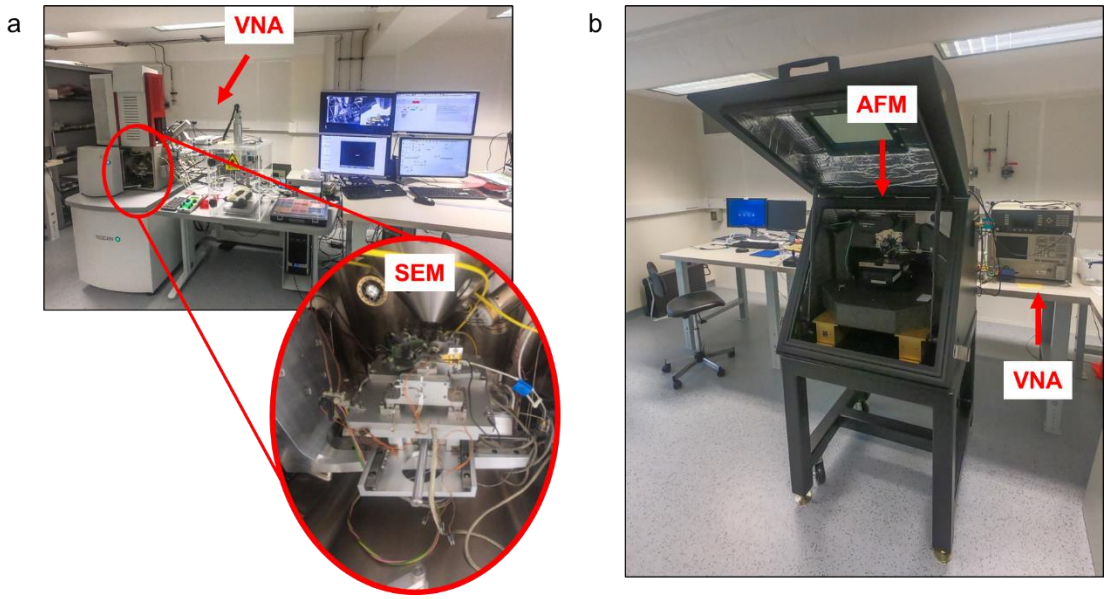

Figure 2.18. *SMM systems: (**a**) IEMN-made and (**b**) Keysight technologies.*

SMM is also very useful for measuring the local capacitance. The capacitance can be measured in two ways: it can be derived from the S-parameter or it can be directly measured with an additional differential capacitance (dC/dV) module added to the interferometer. For the first method, several calibration procedures have been reported but here we used two calibration methods: the calibration procedure described by Keysight Technologies and an interferometric model developed at the IEMN.[32] The second method to measure capacitance consists of a direct measurement of the dC/dV.

EFM calibration

For a given frequency, the measured S_{11} can be expressed in terms of error parameters (e_{00}, e_{01} and e_{11}) and related to the S parameter of the probe-sample system $S_{11,a}$ as:

$$S_{11} = e_{00} + e_{01}\frac{S_{11,a}}{1-e_{11}S_{11,a}} \tag{2.18}$$

where the error values include spatial losses, the stray capacitance, the phase shift and the attenuation produced by the couplers and splitters. While some error parameters, such as the one produced by the attenuation, depend mainly on the SMM system and remain constant through measurements, other errors such as the one produced by the stray capacitance, are made *in-situ*, that is, they are associated to the different tip-sample distance in each experiment. Generally, the error parameters are determined from three known reference samples but, since the stray capacitance will be disturbed when changing

the samples, Gramse *et al.* implemented a method that allows determining the error values from the DUT. [32] They used an approach-retract curve and recorded the S_{11} though the entire tip-sample distance. For dielectric samples, the impedance is only capacitive and can be measured at low frequencies (~ 1.5 kHz) by electric force microscopy (EFM). As described in **section 2.2.6**, the second harmonic is used for capacitive measurements thus it is recorded here. Although in EFM the second harmonic could be recorded, it constitutes a complex problem.[33,34] EFM involves van der Waals interactions between the probe and the sample, which are affected by any contaminants on the surface and/or the atmospheric conditions. It also modulates the capacitance with the vibration mode of the cantilever giving increased contribution from the moving end of the probe. This may limit the accuracy of the calibration. However, in contrast to EFM, SMM provides additional capabilities for capacitance measurements. In particular, since it operates in contact mode, an additional DC voltage can be added to evaluate the dependence of the capacitance with that voltage and deduce material properties such as doping type and eventually doping level.

Following **Eq. 2.10**, the integration of the electrostatic force *vs* the applied voltage curve results in the capacitance C(z). Next, from the approach-retract curve combining EFM and S_{11}, the error values can be determined. The capacitance has different contributions: tip-sample, cone-sample and probe plateau-sample. Near the sample, at a distance in the range of the tip radius, due to the local electrical interactions, the tip-sample contribution is large and follows a non-linear trend. In contrast, far from the sample the capacitance variation becomes small compared to the overall capacitance and can be linearized, as observed in **Fig. 2.19**.[35–37]

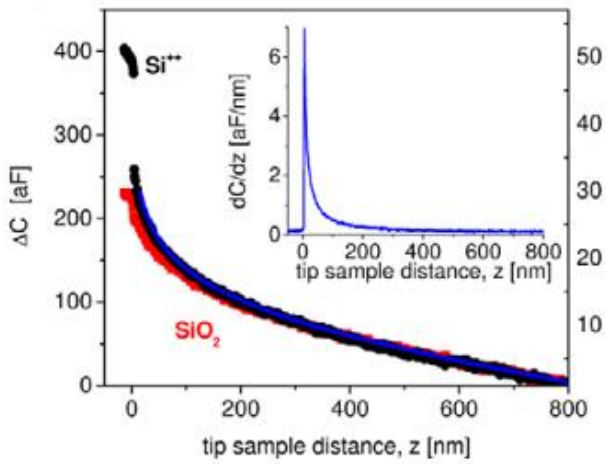

Figure 2.19. *Capacitance approach curves deduced from SMM measurements after EFM calibration onto highly doped Si^{++} (black), a 105 nm thick SiO_2 film (red). Inset: dC/dz deduced from EFM measurement (blue).*[32]

Interferometric calibration

To convert the S_{11} into complex impedance Z, an interferometric calibration is under development. First, a frequency for the measurement is set near a given frequency interference. Then, the procedure consists on recording the interference of the S parameter over two different frequency ranges. One range will span over several interferences, while the second frequency range will focus only on the interference near the frequency we set for the measurement.

Considering that the sinusoidal wave a_i created in the VNA source can be written as

$$a_i = a_0 e^{i\omega t} \tag{2.19}$$

where a_0 is a complex number composed by its amplitude $|a_0|$ and phase φ_{a0} at the initial point, x = 0. Then, at a given point of the system, the wave is split in two where one is directed to the DUT and the other one is used as a reference. Therefore, now it is necessary to take into account the distance (x) to the source at a given time (t):

$$a(x,t) = a_0 e^{-i(kx-\omega t)} \tag{2.20}$$

where k is the wave vector ($k=\omega/v_g$). Once the incident wave reaches the DUT and is reflected, it is defined as:

$$a(x,t) = e_{10}\Gamma a_0 e^{-i(kx-\omega t)} \tag{2.21}$$

where e_{10} includes the spatial losses, the phase shift and the attenuation produced by the couplers and splitters. The term Γ represents the reflection coefficient after interacting with the DUT. The other wave is directed to the attenuator and is defined as:

$$b(x,t) = e_{20}a_0e^{-i(kx-\omega t)} \tag{2.22}$$

where, again, e_{20} includes the spatial losses, the phase shift and the attenuation. The wave coupling is made in a given point, called x_1 for the reflected wave and x_2 for the reference wave. The amplitude of both waves is added following the expression:

$$a(x,t) + b(x,t) = e_{10}\Gamma a_0e^{-i(kx-\omega t)} + e_{20}a_0e^{-i(kx-\omega t)} \tag{2.23}$$

and then amplified by a complex gain, G, as:

$$a_r(x,t) + b_r(x,t) = Ga_0(e_{10}\Gamma e^{-ikx_1} + e_{20}e^{-ikx_2})e^{i\omega t} \tag{2.24}$$

The combined signal is detected by the VNA, which corresponds to the S parameter:

$$S = G(e_{10}\Gamma e^{-ikx_1} + e_{20}e^{-ikx_2}) \tag{2.25}$$

which corresponds to the complex amplitude from the combined wave. Since the length of the 2 different cables for the incident wave and the reference wave is not the same, there is a phase shift between them. This allows to nullify the S parameter using the attenuator, which can adjust e_{20}, resulting in a virtual Γ_0 used as a reference. When the signal is nullified, which occurs at some given angular frequency of interest ω_0 corresponding to wavelength k_0, $e_{20}e^{-ik_0x_2} = -e_{10}e^{-ik_0x_1}\Gamma_0$, and then:

$$S_{measured} = Ge_{10}e^{-ik_0x_1}(\Gamma e^{-i(k-k_0)x_1} - \Gamma_0e^{-i(k-k_0)x_2}) \tag{2.26}$$

However, even in the case where the interference is not perfectly nullified, a virtual reflection coefficient Γ_0 nullifies the combined signal:

$$\Gamma_0 = -\frac{e_{20}}{e_{10}}e^{-ik_0(x_2-x_1)} \tag{2.27}$$

Eq. 2.26 can be expressed as:

$$S_\Gamma(k) = S_{\Gamma_0}(k) + Ge_{10}e^{-ik_0x_1}(\Gamma - \Gamma_0)e^{-i(k-k_0)x_1} \tag{2.28}$$

Eq. 2.28 can be rewritten with the frequency difference $(f - f_0)$ and time difference $(t_1 - t_2)$ instead of the wave vector difference $(k - k_0)$ and spatial position difference $(x_1 - x_2)$, respectively. Using also $A = 2Ge_{10}e^{-ik_0x_1} = |A|e^{i\varphi_A}$, the first term becomes:

$$S_{\Gamma_0}(k) = |A|\Gamma_0 \sin[\pi(f - f_0)(t_2 - t_1)]e^{i[\frac{\pi}{2} - 2\pi(f-f_0)\frac{t_1+t_2}{2} + \varphi_A]} \quad (2.29)$$

where Γ_0 is a reflexion coefficient corresponding to an admittance that can be virtually described by a capacitance (C_0) and a conductance (G_0). The second term is rewritten as:

$$S_\Gamma(k) - S_{\Gamma_0}(k) = |A|\frac{\Gamma - \Gamma_0}{2} e^{i[-2\pi(f-f_0)t_1 + \varphi_A]}] \quad (2.30)$$

Due to the small probing area in SMM measurements, the admittance is usually small, therefore, $\Gamma \approx \Gamma_0 \approx 1$. This means that usually the term $\frac{\Gamma - \Gamma_0}{2} e^{i[-2\pi(f-f_0)t_1 + \varphi_A]}$ is much lower than $\sin[\pi(f - f_0)(t_1 - t_2)]$. When the experimental data is measured over a frequency range such that $(f - f_0)(t_1 - t_2) \cong 2$, they can be fitted with **Eq. (2.29)**, which makes it possible to determine $t_1 - t_2$ and $t_1 + t_2$ from the periodicity of the amplitude and phase over several periods. Also, fitting the experimental interferences allows to obtain the values of amplitude and phase (|A| and φ_A) so that the fitting is best near the interference near the frequency of interest (f_0), see **Fig. 2.20a** and **b**. However, due to the non-linear dependence of the electrical properties with the frequency, the frequencies far from f_0 do not fit well. Nonetheless, the curve follows well the experimental data in a range of around 500 MHz from f_0, which is enough to continue with the procedure.

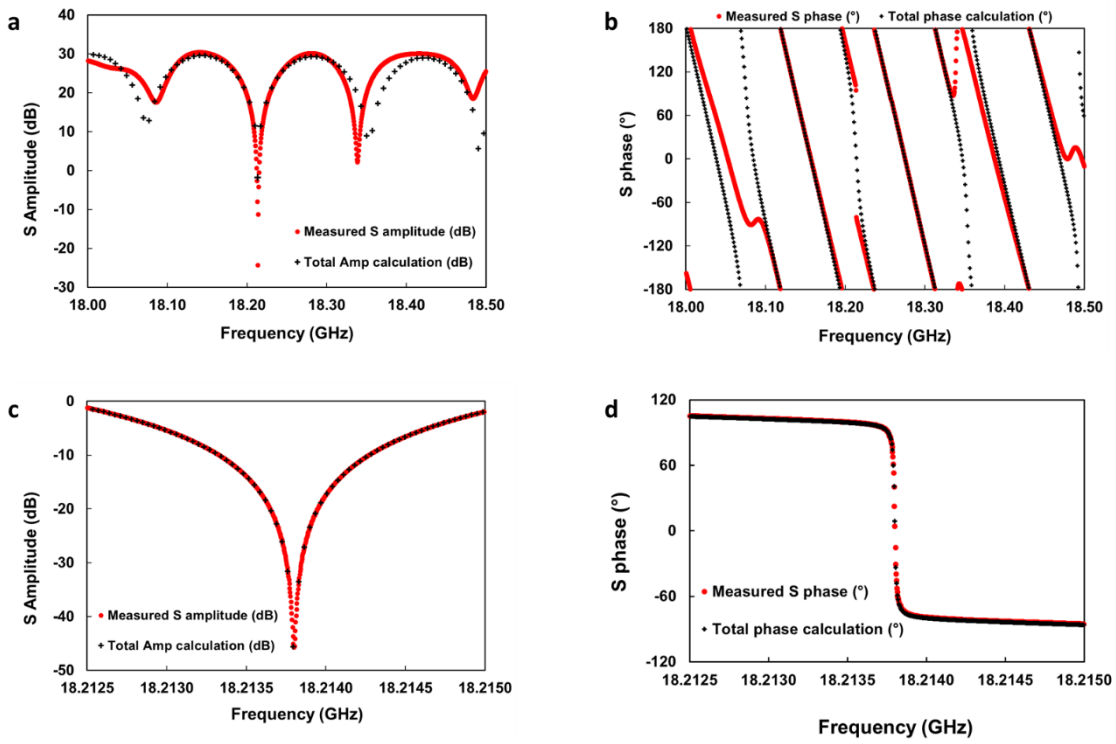

Figure 2.20. *Comparison between the experimental interference curve around 18.21 GHz and the modelled curve using Eq. 2.28 for* ***(a)*** *(**b**) a wide range of frequencies and* ***(c)*** *(**d**) a shorter range of frequencies. The used sample was composed of ITO/PEDOT:PSS/MAPI-PbAc*$_2$.

With t_1 and t_2 estimated, now we use a frequency range much shorter than before, as in **Fig. 2.20c** and **d** so as to fine tune the value of A near the interference. We track the amplitude and phase variation over typically hundred MHz around the f_0. If we consider $f_0 \approx f$, **Eq. (2.29)** can be written as:

$$S_{\Gamma_0}(k) = -|A|\Gamma_0\,\pi(f-f_0)(t_1-t_2)\,e^{i\left[\frac{\pi}{2}-2\pi(f-f_0)\frac{t_1+t_2}{2}+\varphi_A\right]} \qquad (2.31)$$

where |A| and φ_A can be found by fitting $S_{\Gamma_0}(k)$) vs frequency. Note that in **Fig. 2.20,** the fit is done using Eq. (**2.28**) for better validation of the model. This allows in particular to fine tune the dependence of $S_\Gamma(k)$ in the vicinity of f_0 (10 kHz range) by taking into account the admittance (Y_0) that makes the interference not fully abrupt (phase shifting by 180° without continuity due to the change of sign of (f-f_0)).

So far, |A| was determined from the wide frequency measurement and from the shorter frequency measurement, both giving similar values yet slightly shifted. This problem can be improved by enhancing the microwave components. Both t_1 and t_2 have been also

estimated. Therefore, we can proceed to measure a given sample in order to determine its admittance.

The determination of the sample's admittance (and capacitance) can be done if we take into account that the frequency set to make the measurement (f_1) may be shifted from f_0 by a small quantity (a few tens of kHz for instance), so that:

$$S_{k_1}(\Gamma) \cong B\frac{\Gamma-\Gamma_1}{2} \cong BZ_C(Y_1 - Y) \tag{2.34}$$

where $\Gamma_1 = \Gamma_0 e^{-i(k_1-k_0)(x_2-x_1)}$, $B = Ae^{-i(k_1-k_0)x_1}$ and Y_1 is the virtual admittance that gives $S_{k_1}(\Gamma_1) = 0$ at f_1. $Y_1 - Y$ is here assumed to be << $1/Z_C$. With the calibrated parameters, the admittance can be deduced.

Capacitance-Voltage Measurements

The C-V curve can be obtained by measuring the S_{11} for a range of dc biases. **Fig. 2.21a** shows an ideal C-V curve for a p-type semiconductor. This curve can be understood by taking the analogy with a metal-oxide-semiconductor (MOS) capacitor. In this work, the metal is the AFM probe (Rocky Mountain Nanotechnology xxPtyyyA), the oxide is Al_2O_3 and the semiconductor material is the perovskite under study. The capacitance associated to each region can be determined using a parallel plate approximation where the MOS structure can be seen as a group of capacitors connected as in **Fig. 2.21b**.[38]

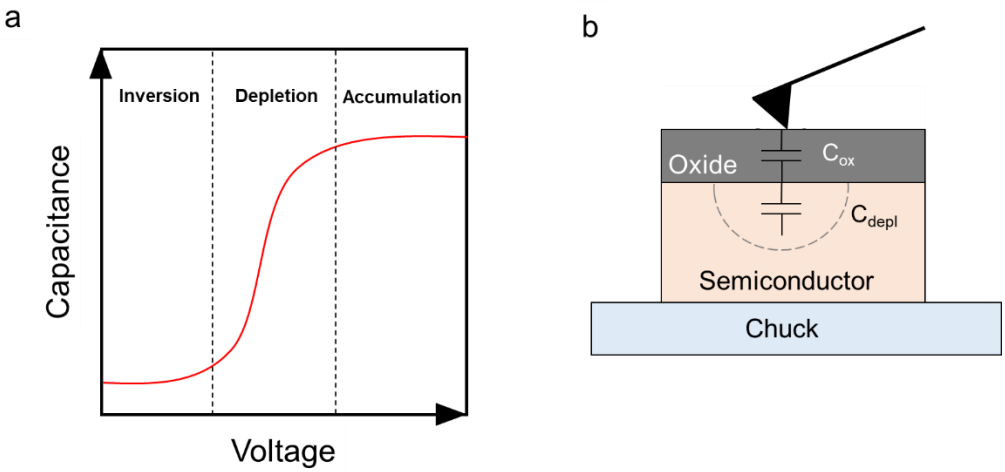

Figure 2.21. *(a) Ideal C-V curve of n-type semiconductor. (b) Metal-Oxide-Semiconductor (MOS) scheme of the SMM set-up with the associated capacitances.*

In the flat band region, the energy bands (conduction and valence bands) in the semiconductor are flat. This is reached between the accumulation and depletion behaviour in **Fig. 2.21a**. It corresponds to the case where the charge in the MOS capacitance is null. This situation is reached by applying a voltage (flat band voltage) that compensates the work function difference between the metal probe and the semiconductor. However, if there are charges in the oxide, the flat band voltage shifts to positive or negative values, depending on the sign of the charges.[39] Additional charges may also be present at the semiconductor interface that may be charged or discharged depending on the applied voltage. They compete with the semiconductor depletion, which results in a dilatation of the voltage scale in **Fig. 2.21a**.[38]

In the accumulation region, the majority charges (holes in p-type) are driven towards the anode (tip side) creating an accumulation at the oxide-semiconductor interface. This phenomenon occurs when applying negative voltages to the probe. The accumulation region can be further understood looking at the scheme in **Fig. 2.21a**, the total capacitance (C_{tot}) is mainly the oxide capacitance (C_{ox}) and it is independent on the doping type and carrier concentration of the semiconductor:

$$C_{tot} = C_{ox} = \frac{\varepsilon_{ox}\, \varepsilon_0\, A}{t_{ox}} \tag{2.35}$$

where ε_{ox} is the electric permittivity of the oxide, ε_0 is the dielectric permittivity in the vacuum, A is the surface area of the probe contact and t_{ox} is the oxide thickness.

When applying positive voltages to the probe, the majority carriers are driven towards the cathode (semiconductor side), this is known as depletion region and it induces a space region with a characteristic capacitance (C_{depl}), this is represented in **Fig. 2.21b**. The total capacitance will depend on both the C_{ox} and the C_{depl}:

$$C_{tot} = \frac{C_{ox}\, C_{depl}}{C_{ox} + C_{depl}} \tag{2.36}$$

where

$$C_{depl} = \frac{\varepsilon_{sem}\, \varepsilon_0}{\sqrt{\frac{2\, \varepsilon_{sem}\, \varepsilon_0\, \phi_{sem}}{q\, N}}} \tag{2.36}$$

being ϕ_{sem} the interface potential of the semiconductor, q the elementary charge and N is the acceptor dopant concentration of the semiconductor. If the positive voltage is further increased, then the energy bands will bend further downwards eventually crossing the fermi energy level, creating what is called "inversion". At this point, the capacitance depends on minority carriers. Depending on the ability of minority charges to follow the applied frequency will result in either a higher capacitance (normally for low frequencies) or lower capacitance (for high frequencies). At low frequencies, the system is in thermal equilibrium and minority carriers can respond, therefore only Cox is taken into account:

$$C_{tot} = C_{ox} \tag{2.37}$$

When the frequencies are high, minority carriers cannot follow so they do not contribute to the total capacitance and it decreases to a level below the depletion capacitance. Therefore, C_{tot} will be a combination of C_{ox} and C_{depl} at its maximum width:

$$C_{tot} = \frac{C_{ox}\, C_{inv}}{C_{ox} + C_{inv}} \tag{2.38}$$

where

$$C_{inv} = \frac{A\, \varepsilon_{sem}\, \varepsilon_0}{\sqrt{\frac{2\, \varepsilon_{sem}\, \varepsilon_0 2\, \phi_{sem}}{q\, N}}} \tag{2.39}$$

However, the stray capacitance induced by the system is usually in the order of picofarads (pF), which is much larger than the sample's capacitance (in the order of attofarads, aF). Therefore, a good technique to get rid of parasitic capacitance is the differential capacitance measurement.

Differential capacitance measurement

Another way to measure the capacitance is through a direct measurement of the differential capacitance (dC/dV) at different dc biases, similar as in scanning capacitance microscopy (SCM). As a comparison, in SCM two signals are simultaneously analysed: one in the GHz frequency range and the other one in the kHz range. Instead, the SMM can discriminate ac signals since only the reflected wave with the same frequency as the incident wave is detected by the VNA. In fact, SMM can measure dC/dV by applying an ac voltage with a low frequency (in the kHz range) and a microwave signal coming from the VNA (2 to 18 GHz) sent through an additional external module. The differential

capacitance is then measured with respect to a fixed dc bias. **Fig. 2.22** shows the diagram of the SMM system using the dC/dV module in blue. The scheme represents the SMM configuration as in **Fig. 2.17** plus the addition of the dC/dV module in blue. The dC/dV module can be mainly considered as an amplifier to be able to detect the small variations.

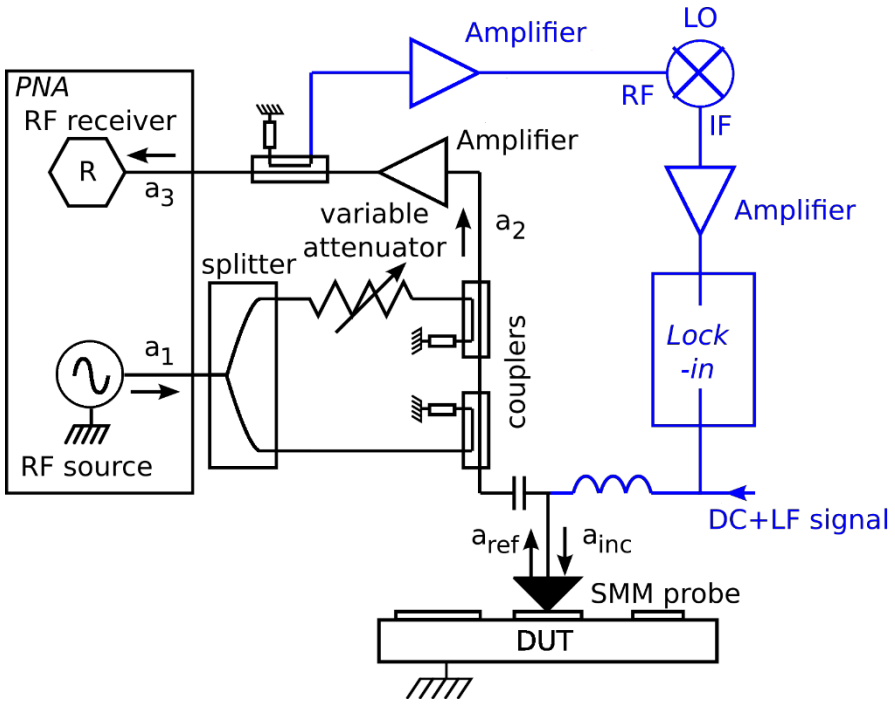

Figure 2.22. *Diagram of the VNA (black area) and dC/dV module (blue area) components.*[40]

The signal from the VNA enters the interferometric module as previously described. A coupler (not shown in the figure) allows for sending a reference signal to the local oscillator signal (LO) part of the dC/dV mixer. A second low frequency (LF) signal is sent to the tip from an external source. The LF signal induces a capacitive change in the sample and it makes the incident VNA signal to follow the same modulation which, at the same time, will be proportional to capacitance change. The reflected signal coming out of the interferometer is split in two, one is amplified and sent to the dC/dV module mixer where it is combined with the LO signal. The resulting signal is processed by an external lock-in amplifier where the complex values of dC/dV are obtained. The second part of the split signal is sent to the VNA to measure the average capacitance.[40]

The measurement of dC/dV has been shown to be especially useful in the semiconductor industry where non-linear behaviour at low frequency (RF) signal results in an impedance variation. Even if the impedance variation is typically low, the difference between the

incident VNA signal and the low frequency cause a signal magnification. The relationship between the capacitance difference (ΔC) and the impedance difference (ΔZ) is:

$$\Delta Z = \frac{1}{2\,\pi\, j\, f\, \Delta C} \tag{2.40}$$

where f is the microwave operation frequency. Therefore, the sensitivity is a prori increased compared to direct low frequency measurement and will further increase for higher frequencies.[40] The shift in dC/dV will be more significant around the depletion range, where the capacitance-voltage (C-V) curve will show the largest slope possible, **Fig. 2.23**. Under these conditions, high dC/dV values indicate low carrier concentration or low doping (red curve in **Fig. 2.23**) while low dC/dV values correspond to high carrier concentration or high doping. The signal is then analysed with a lock-in amplifier. The set up used in this work allows to use signals in a range of 50 kHz to 500 kHz.

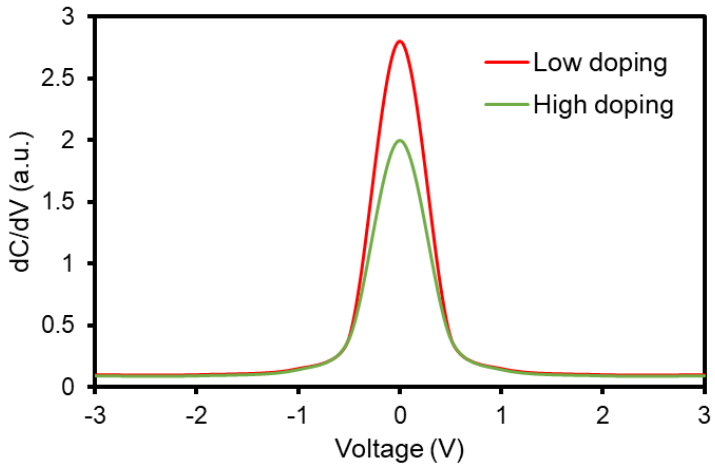

Figure 2.23. *Ideal dC/dV vs voltage curves derived from C-V curves.*

References

1. You, J. *et al.* Low-Temperature Solution-Processed Perovskite Solar Cells with High Efficiency and Flexibility. *ACS Nano* **8**, 1674–1680 (2014).

2. Xiao, Z. *et al.* Efficient, high yield perovskite photovoltaic devices grown by interdiffusion of solution-processed precursor stacking layers. *Energy Environ. Sci.* **7**, 2619–2623 (2014).

3. Ahn, N. *et al.* Highly Reproducible Perovskite Solar Cells with Average Efficiency of 18.3% and Best Efficiency of 19.7% Fabricated via Lewis Base Adduct of Lead(II) Iodide. *J. Am. Chem. Soc.* **137**, 8696–8699 (2015).

4. Zhou, Y. *et al.* Room-temperature crystallization of hybrid-perovskite thin films via solvent–solvent extraction for high-performance solar cells. *J. Mater. Chem. A* **3**, 8178–8184 (2015).

5. Xiao, M. *et al.* A Fast Deposition-Crystallization Procedure for Highly Efficient Lead Iodide Perovskite Thin-Film Solar Cells. *Angewandte Chemie* **126**, 10056–10061 (2014).

6. Bruening, K. & Tassone, C. J. Antisolvent processing of lead halide perovskite thin films studied by in situ X-ray diffraction. *J. Mater. Chem. A* **6**, 18865–18870 (2018).

7. Pearson, A. J. Structure formation and evolution in semiconductor films for perovskite and organic photovoltaics. *Journal of Materials Research* **32**, 1798–1824 (2017).

8. Chen, Q. *et al.* Planar Heterojunction Perovskite Solar Cells via Vapor-Assisted Solution Process. *J. Am. Chem. Soc.* **136**, 622–625 (2014).

9. Zhao, D. *et al.* Annealing-free efficient vacuum-deposited planar perovskite solar cells with evaporated fullerenes as electron-selective layers. *Nano Energy* **19**, 88–97 (2016).

10. Balaji, G. *et al.* CH3NH3PbI3 from non-iodide lead salts for perovskite solar cells via the formation of PbI2. *Phys. Chem. Chem. Phys.* **17**, 10369–10372 (2015).

11. Zhang, W. *et al.* Ultrasmooth organic-inorganic perovskite thin-film formation and crystallization for efficient planar heterojunction solar cells. *Nat Commun* **6**, 6142 (2015).

12. Wang, Q. *et al.* Qualifying composition dependent p and n self-doping in CH3NH3PbI3. *Appl. Phys. Lett.* **105**, 163508 (2014).

13. Zhang, W. *et al.* Enhanced optoelectronic quality of perovskite thin films with hypophosphorous acid for planar heterojunction solar cells. *Nat Commun* **6**, 10030 (2015).

14. Troughton, J., Hooper, K. & Watson, T. M. Humidity resistant fabrication of CH3NH3PbI3 perovskite solar cells and modules. *Nano Energy* **39**, 60–68 (2017).

15. Jeon, N. J. *et al.* Solvent engineering for high-performance inorganic–organic hybrid perovskite solar cells. *Nature Materials* **13**, 897–903 (2014).

16. Huang, Z., Wang, D., Wang, S. & Zhang, T. Highly Efficient and Stable $MAPbI_3$ Perovskite Solar Cell Induced by Regulated Nucleation and Ostwald Recrystallization. *Materials (Basel)* **11**, (2018).

17. Moerman, D. *et al.* Towards a unified description of the charge transport mechanisms in conductive atomic force microscopy studies of semiconducting polymers. *Nanoscale* **6**, 10596–10603 (2014).

18. Bruker. PeakForce TUNA. *Nanoelectrical Application Module* (2010).

19. Kronik, L. & Shapira, Y. Surface photovoltage phenomena: theory, experiment, and applications. *Surface Science Reports* **37**, 1–206 (1999).

20. Grévin, B. Kelvin Probe Force Microscopy Characterization of Organic and Hybrid Perovskite Solar Cells. in *Kelvin Probe Force Microscopy: From Single Charge Detection to Device Characterization* (eds. Sadewasser, S. & Glatzel, T.) 331–365 (Springer International Publishing, 2018). doi:10.1007/978-3-319-75687-5_11.

21. Melitz, W., Shen, J., Kummel, A. C. & Lee, S. Kelvin probe force microscopy and its application. *Surface Science Reports* **66**, 1–27 (2011).

22. Kalinin, S. V. & Gruverman, A. *Scanning Probe Microscopy: Electrical and Electromechanical Phenomena at the Nanoscale*. (Springer-Verlag, 2007). doi:10.1007/978-0-387-28668-6.

23. Collins, L., Kilpatrick, J. I., Kalinin, S. V. & Rodriguez, B. J. Towards nanoscale electrical measurements in liquid by advanced KPFM techniques: a review. *Rep. Prog. Phys.* **81**, 086101 (2018).

24. Turton, R. J. *The Physics of Solids*. (Oxford University Press, 2000).

25. Lange, M., Vörden, D. van & Möller, R. A measurement of the hysteresis loop in force-spectroscopy curves using a tuning-fork atomic force microscope. *Beilstein J. Nanotechnol.* **3**, 207–212 (2012).

26. Weber, J. C. *et al.* A near-field scanning microwave microscope for characterization of inhomogeneous photovoltaics. *Review of Scientific Instruments* **83**, 083702 (2012).

27. Imtiaz, A., Baldwin, T., Nembach, H. T., Wallis, T. M. & Kabos, P. Near-field microwave microscope measurements to characterize bulk material properties. *Appl. Phys. Lett.* **90**, 243105 (2007).

28. Anlage, S. M., Steinhauer, D. E., Feenstra, B. J., Vlahacos, C. P. & Wellstood, F. C. Near-Field Microwave Microscopy of Materials Properties. in *Microwave Superconductivity* (eds. Weinstock, H. & Nisenoff, M.) 239–269 (Springer Netherlands, 2001). doi:10.1007/978-94-010-0450-3_10.

29. Happy, H., Haddadi, K., Theron, D., Lasri, T. & Dambrine, G. Measurement Techniques for RF Nanoelectronic Devices: New Equipment to Overcome the Problems of Impedance and Scale Mismatch. *IEEE Microwave Magazine* **15**, 30–39 (2014).

30. Huber, H. P. *et al.* Calibrated nanoscale capacitance measurements using a scanning microwave microscope. *Rev Sci Instrum* **81**, 113701 (2010).

31. Dargent, T. *et al.* An interferometric scanning microwave microscope and calibration method for sub-fF microwave measurements. *Review of Scientific Instruments* **84**, 123705 (2013).

32. Gramse, G. *et al.* Calibrated complex impedance and permittivity measurements with scanning microwave microscopy. *Nanotechnology* **25**, 145703 (2014).

33. Kimura, K., Kobayashi, K., Matsushige, K., Usuda, K. & Yamada, H. Noncontact-mode scanning capacitance force microscopy towards quantitative two-dimensional carrier profiling on semiconductor devices. *Appl. Phys. Lett.* **90**, 083101 (2007).

34. Kobayashi, K., Yamada, H. & Matsushige, K. Dopant profiling on semiconducting sample by scanning capacitance force microscopy. *Appl. Phys. Lett.* **81**, 2629–2631 (2002).

35. Fumagalli, L. *et al.* Nanoscale capacitance imaging with attofarad resolution using ac current sensing atomic force microscopy. *Nanotechnology* **17**, 4581–4587 (2006).

36. Fumagalli, L., Ferrari, G., Sampietro, M. & Gomila, G. Dielectric-constant measurement of thin insulating films at low frequency by nanoscale capacitance microscopy. *Appl. Phys. Lett.* **91**, 243110 (2007).

37. Gomila, G., Toset, J. & Fumagalli, L. Nanoscale capacitance microscopy of thin dielectric films. *Journal of Applied Physics* **104**, 024315 (2008).

38. Sze, S. M. Physics of Semiconductor Devices, 3rd Edition | Wiley. *Wiley.com* https://www.wiley.com/en-be/Physics+of+Semiconductor+Devices%2C+3rd+Edition-p-9780471143239 (1981).

39. Buh, G. H., Tran, C. & Kopanski, J. J. PSPICE analysis of a scanning capacitance microscope sensor. *Journal of Vacuum Science & Technology B: Microelectronics and Nanometer Structures Processing, Measurement, and Phenomena* **22**, 417–421 (2004).

40. Bonnell, D. A. & Kalinin, S. V. *Scanning Probe Microscopy for Energy Research*. vol. 7 (WORLD SCIENTIFIC, 2013).

Chapter 3

Local Electronic Heterogeneities on the $CH_3NH_3PbI_3$ Perovskite Surface

The following publication was adapted from this chapter:

J. Llacer, D. Moerman, O. Douhéret, X Noirfalise, C. Quarti, R. Lazzaroni, D. Théron and P. Leclère, ACS Applied Nano Materials, 2020, 3, 8268-8277.

Surface properties are a key aspect to improve not only the interface properties in photovoltaic cells but also the stability. They are even more important in perovskite materials where much engineering has been researched in order to improve the interface properties. In this chapter, the local electronic properties of two different $CH_3NH_3PbI_3$ perovskite films are studied by atomic force microscopy methods. Nanoscale features such as local surface potential are correlated to current response. Perovskites made with lead acetate as a precursor for lead, result in a more heterogeneous surface compared to perovskites made with lead iodide in the precursor solution.

3.1 Introduction

Organic-inorganic hybrid perovskites have been capturing much interest in the field of photovoltaics (PV) as the power conversion efficiencies (PCEs) of corresponding devices have been strongly improved, from 3.8% in 2009 to more than 23% recently.[1,2] This prodigious increase in just a decade is the result of intense research and fundamental understanding of crucial intrinsic properties of the perovskites; in particular, their electronic and charge transport properties feature remarkably long diffusion lengths and carrier lifetimes.[3–8] However the device stability and the mechanisms responsible for this low stability are still under debate.[9,10] In addition to the bulk properties, the surface properties, which depend on the crystallographic facets and the possible presence of defects, are also of prime importance as their impact on the electronic and transport properties at grain boundaries or other interfaces is significant, hence affecting the performances of the devices.[11–18]

Several methods are proposed for reducing these detrimental effects for photovoltaic performances, involving, among others, tuning of the perovskite composition and interfacial engineering.[19–21] For instance, reducing the recombination at the interface can be achieved by introducing a chemical linker between the perovskite and the electron transport layer.[22] Recombination sites were also reduced after passivation of grain boundaries using either an excess of methylammonium iodide (MAI) during the synthesis or a post-fabrication surface treatment.[23,24]

Yet, to face such a major issue, the electronic properties of the surface of perovskite thin films ought to be further investigated where variations can be observed, *i.e.* at the nanoscale. In this regard, Scanning Probe Microscopy (SPM) provides several characterization methods to locally map the electronic properties of materials with nanometer resolution.[25–31] Kim *et al.* recently used Kelvin Probe Force Meicroscopy (KPFM) and bias-dependent atomic force microscopy (AFM) to show that the properties of the (112) surface of a perovskite crystal can be affected upon external bias while the (100) surface remains unchanged.[32] KPFM has also been used by many other groups to study the surface potential of perovskite thin films: Bergmann *et al.* used cross-section KPFM on a $MAPbI_3$ based solar cell to show the unbalanced charge-carrier extraction between electrons and holes.[27] Harwell *et al*. exposed the $MAPbI_3$ perovskite repeatedly

to light and found that the Fermi level eventually returns with time to its initial value with slow decay, this effect being attributed to trapped or slow charges within the device.[33] Stecker *et al.* used SPM to identify vacancy-assisted transport and, combined with density functional theory (DFT) calculations, they predicted an increase of the work function when increasing the number of vacancies in $MAPbBr_3$.[34] Gallet *et al.* found electronic heterogeneities at the $MAPbI_3$ perovskite surface and attributed them to differences in surface terminations.[35]

From these works, it has been mostly agreed that among the surface features ruling the electronic properties of the perovskite, defects or traps are those responsible for the electronic heterogeneities observed at the local scale. Traps can be classified as shallow or deep, depending on the energy position in the gap. Calculations on the activation energies of all the possible point defects as determined from those studies revealed that usually shallow trap states are more likely to form than deep traps, and they can be an explanation for the long electron-hole diffusion lengths observed in these materials.[36] Yet, Du *et al.* identified iodine interstitials, with specifically low activation energies that could generate significant deep trap states.[37] And all these studies are also pointing out how the type and density of traps at the surface of the perovskite are depending on the growth conditions of the materials along with the anisotropy of the surface properties. In spite of different types of defect evidenced at the surface, their corresponding impact onto the film stability are still under debate. To enhance perovskite stability, it is therefore crucial to understand how these defects specifically affect the surface properties and how they interact with water molecules, especially at the early stage of degradation.

In this chapter, frequency modulated KPFM (FM-KPFM) and Conductive Atomic Force Microscopy (C-AFM), are used to evidence the presence and the electronic contribution of trap states at the surface of methylammonium lead iodide ($CH_3NH_3PbI_3$ or $MAPbI_3$) perovskite thin films. FM-KPFM is an appropriate method to simultaneously probe topographic and surface potential variations without cross-talking.[25,29] It measures the contact potential difference (CPD, *i.e.* the work function difference) between the metallic probe and the sample under test, hence providing meaningful insights towards device performances and stability, see **Chapter 2**.[38] C-AFM was shown to be pertinent for high-resolution electrical characterization of perovskites.[39] As a current measurement method, C-AFM can be sensitive to contributions from surface properties, such as defects, as they

are expected to impact the charge transport mechanism *via* carrier injection.[23,39,40] Combining FM-KPFM and C-AFM allows us to locally correlate carrier injection to work function (WF) in view of understanding the electronic properties of the sample surface.

3.2 Characterization of the $CH_3NH_3PbI_3$ Surface

To gain insight into the perovskite films, we deposited $MAPbI_3$ on top of a glass/ITO/PEDOT:PSS substrate, using $PbAc_2$ as a precursor and following the fabrication procedure described in **section 2.1** for MAPI-$PbAc_2$.[41,42] Freshly-prepared MAPI-$PbAc_2$ thin films were then analyzed by XRD and XPS to determine their chemical composition and crystallinity, respectively, in order to establish reference profiles prior to any degradation process, and to confirm standards reported in literature for pristine $MAPbI_3$. As shown by the XPS spectrum of **Fig. 3.1a**, the major atomic species present at the surface of the MAPI-$PbAc_2$ are, as expected, iodine, nitrogen, carbon and lead. The additional presence of indium atoms could be attributed to the presence of pinholes in the PEDOT:PSS + $MAPbI_3$ stack.[43] The corresponding XRD profile, displayed in **Fig. 3.1b,** indicates a dominating presence of (110) and equivalent (220) crystalline planes corroborating the high crystal orientation expected from this fabrication route.[44] Moreover, the characteristic peak of PbI_2 expected at ~ 12.6° (see asterisk symbol in **Fig. 3.1b**), and usually related to perovskite phase segregation, is absent, allowing these XRD and XPS data to serve as reference profiles for pristine MAPI-$PbAc_2$.[45] The corresponding morphology of the films is composed of grains of varying size (170 ± 130 nm in diameter), as determined with non-contact AFM (**Fig. 3.1c**) operated in an inert environment. The topography of the films reports a typical RMS roughness around 34 nm for 4×4 μm^2 images.

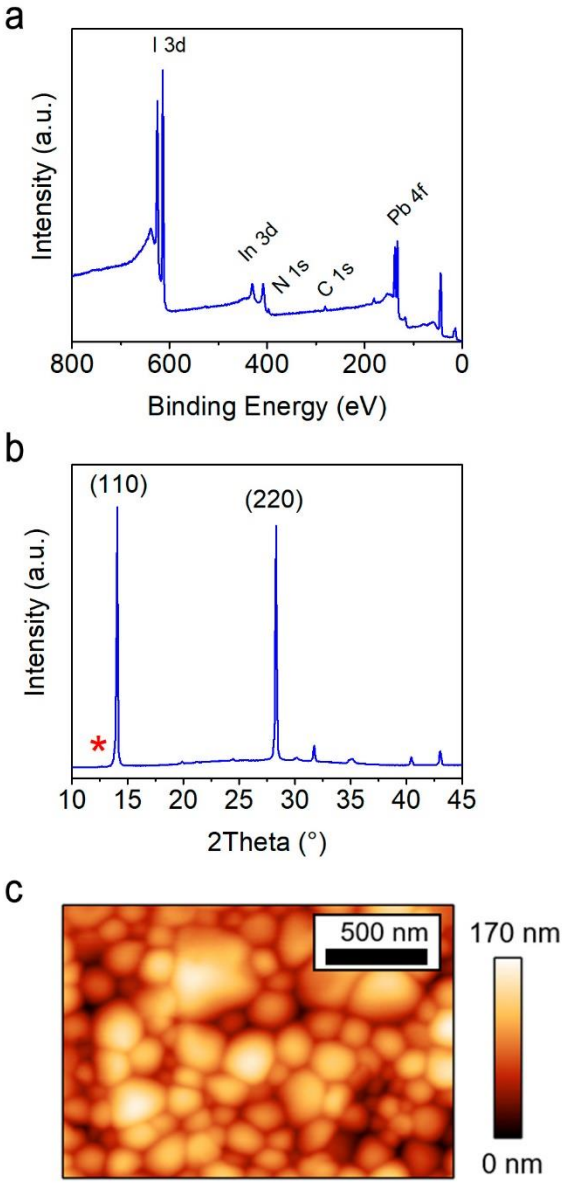

Figure 3.1. *Characterization of freshly-prepared MAPI-$PbAc_2$ deposits: (**a**) XPS survey spectrum, (**b**) X-ray diffractogram (the asterisk symbol indicates the angle corresponding to the reflection expected for PbI_2) and (**c**) typical non-contact AFM height image (cropped from a 4x4 µm image to see more easily the grains).*

Fig. 3.2a and **b** show the topography and WF, respectively, as measured by FM-KPFM for a MAPI-$PbAc_2$ film deposited on glass/ITO/PEDOT:PSS substrate (the WF image was obtained from the surface potential data after tip calibration, see **section 2.2.6**). **Fig. 3.2b** shows spatial heterogeneity of the WF at the film surface, as highlighted by the complex WF distribution curve in **Fig. 3.2d**. Note that the surface properties are studied at the $MAPbI_3/N_2$ interface, however, there may be substantial changes on the interface

properties when the contact with $MAPbI_3$ is made with other gas (like oxygen) or films used for device applications. The substrate on which the perovskite is grown and/or operating conditions (i.e. temperature or pressure) may also affect the surface properties. The WF distribution can be deconvoluted into two dominating populations, which have an average difference of ~ 0.1 eV. A high WF domain (HWF) and a low WF domain (LWF) are highlighted with white and red circles in **Fig. 3.2b**, respectively. However, if we take consider the WF values only at the center of the grains, those two domains show up to 0.2 eV WF difference; 4.80 ± 0.02 eV and 5.00 ± 0.02 eV for LWF and HWF respectively. This calculation is made by masking the HWF and LWF domains in the raw image, as in **Fig. 3.3a and b**. Masks were created by selecting the regions which possess values above or below a given threshold value, thus, HWF and LWF domains appear highlighted respectively. Results will then be discussed as if there were two clearly distinguished populations, although since the deconvoluted profiles are quite large and overlap, there might be intermediate populations lying between and outside the dominating contributions. The schematic representation of LWF and HWF on the KPFM configuration can be seen in **Fig. 3.4**.

The measured WF values lie in a range between 4.70 and 5.10 eV. The reported electron affinity and ionization energy for $MAPbI_3$ are most commonly around 3.9 and 5.4 eV, respectively, although there is some scatter in the literature.[46–49] This would indicate that despite the heterogeneous WF at the surface of the film, the Fermi level remains located between the valence band edge and mid-gap, what means that the whole surface of the MAPI-$PbAc_2$ thin film is exhibiting p-type semiconducting behavior, hence with holes as majority carriers.[46] Notice that the topographic profile does not influence nor correlate with the CPD signal (see **Fig. 3.5a)**; in other words, the contrast in WF images only arises from the electrostatic probing and is, in no manner, due to topographical variations of the surface. Actually, the graphs shown in **Figure 3.5** were performed by subtracting the values of topographic height and CPD for each pixel, in the case of **Fig. 3.5a**, and plotting them. This gives us the ability to detect any preferential trend or relationship between the *x* and *y* data.

Next, C-AFM was performed at the same location. Upon positive dc sample bias, holes are injected from the ITO/PEDOT:PSS bottom electrode into the valence band of the MAPI-$PbAc_2$ and transported across the film prior to collection at the tip-sample contact.

Likewise FM-KPFM measurements, a spatially heterogeneous current response is observed, as shown in **Fig. 3.2c**. A correlation clearly appears, with the HWF (LWF) domains corresponding to high (low) current domains, as exemplified by the white (red) circles in **Fig. 3.2b** and **C**, respectively. Although the histogram for the current signal in **Fig. 3.2e** does not show 2 clear peaks (as for the work function, **Fig. 3.2d**), the correlation between current and WF is further evidenced by the averaged scatter plot shown in **Fig. 3.5c**. The current variation with the topography was meanwhile found to be inside the error bar when compared to the height variations (see **Fig. 3.5b**), indicating little if no correlation also between these two signals.

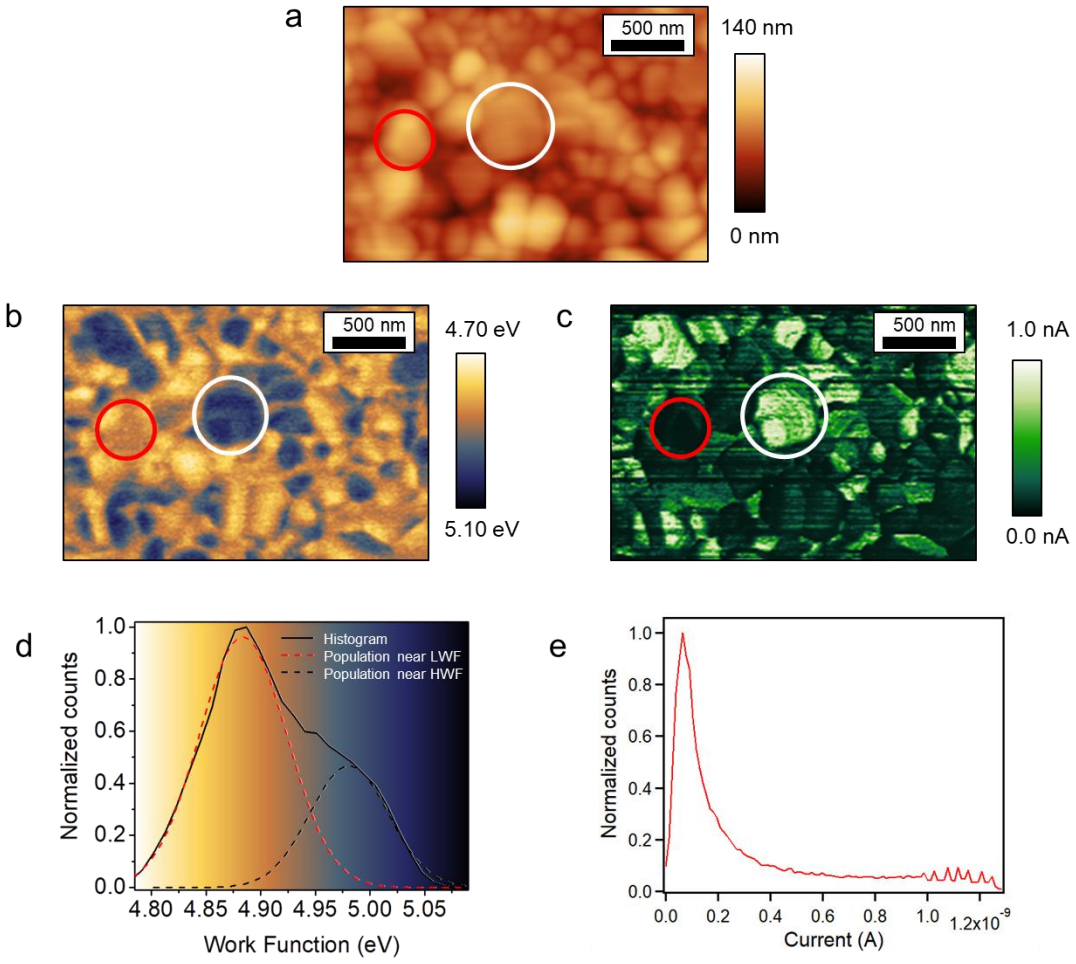

Figure 3.2. *SPM images of MAPI-$PbAc_2$ deposited on glass/ITO/PEDOT:PSS substrate showing the (**a**) topography, (**b**) work function (measured with FM-KPFM), (**c**) current image (measured with C-AFM in Peak-Force tunneling TUNA mode, taking the peak current with an applied dc sample bias of 1.7 V), (**d**) work function histogram (with the color grading used in (c)) and (**e**) current histogram. Note that the FM-KPFM and C-*

AFM measurements were carried out at the same location. Colored circles highlight HWF domains (white circle) and LWF domains (red circle).

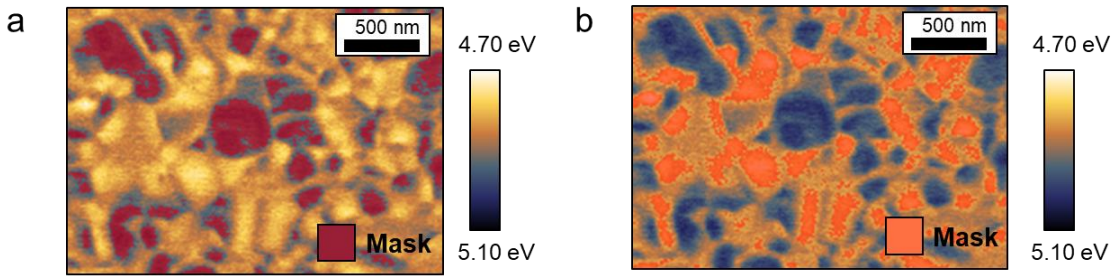

Figure 3.3. *Masks of the (**a**) HWF and (**b**) LWF regions used to determine the average WF in these domains.*

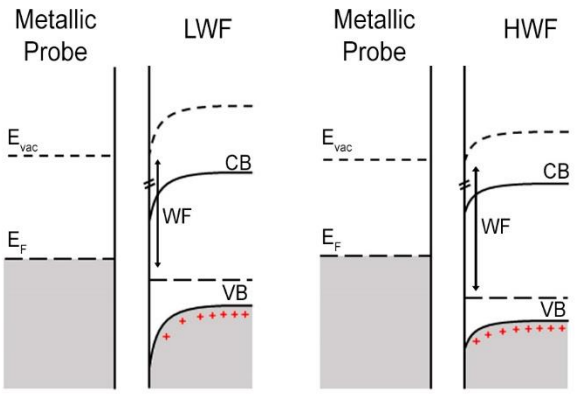

Figure 3.4. *Schematic representation of the LWF and HWF domains in KPFM.*

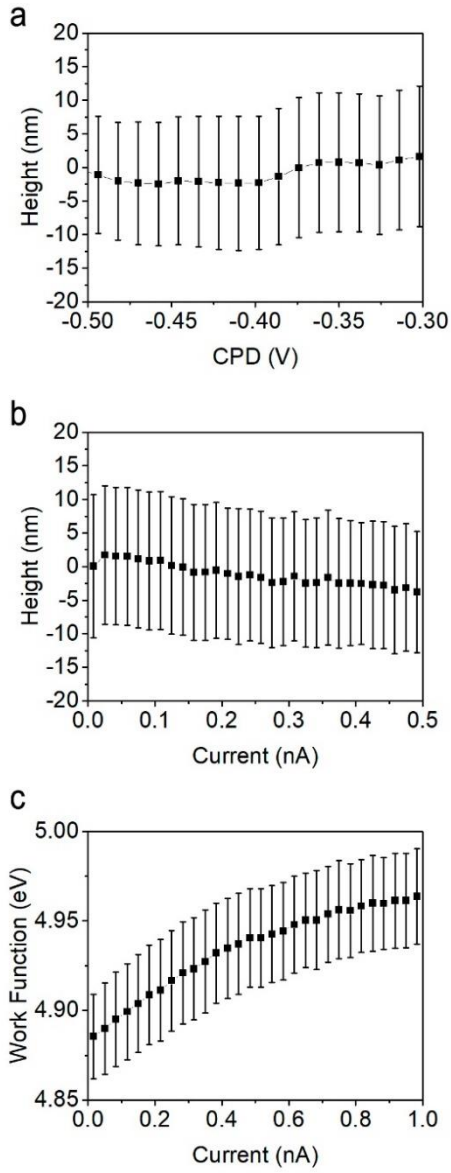

Figure 3.5. *Scatter plots of (**a**) the height vs. CPD, (**b**) the height vs. current and (**c**) the work function vs. current for MAPI-$PbAc_2$ perovskite.*

Because FM-KPFM is probing surface properties, the observed correlation between FM-KPFM and C-AFM images strongly supports that the C-AFM response is also related to the perovskite surface properties. In other words, the C-AFM current is ruled by perovskite surface properties (*i.e.* the local work function) at the tip-sample contact.

So far, we observed different surface domains associated to given local work functions and, at the same time, we found them to be related to different current densities. Surface heterogeneity is further investigated by means of averaged C-AFM images taken at

different biases, where I-V profiles are built for the different domains. **Fig. 3.6a** displays the C-AFM current variations with bias at these two locations, exhibiting an exponential law between 1 and 2 V in both domains, consistently with a specific injection/extraction dominating mechanism. In this bias range, the I-V profiles are characteristic to that of a rectifying diode, suggesting for both locations a Schottky-like contact at the tip-sample contact with an associated built-in potential (V_{bi}) in the films. MAPI-$PbAc_2$ exhibiting p-type behavior, this diode-like contact is therefore biased in forward polarity upon positive dc sample bias.

For a standard Schottky contact, the charge transport between the probe and the sample in forward bias is conditioned by the thermionic-emission theory, which analytical expression is:

$$J = J_0 \, e^{\frac{qV}{nkT}} \left(1 - e^{-\frac{qV}{kT}}\right) \qquad (3.1)$$

Where J is the current density, J_0 is the saturation current density obtained in reverse bias, q is the charge of an electron, V is the voltage applied to the sample, n is the ideality factor of the diode, k is the Boltzmann constant and T is the temperature;[50] and with $J_0 \propto e^{\frac{-q\phi_b}{kT}}$ where ϕ_b is the effective barrier of the Schottky contact. The ideality factors, determined from the slope in the semilog profiles of **Fig. 3.6a**, are similar. The difference in current between the two types of domains in the semilog I-V curve can therefore be mainly attributed to different effective barriers ($\Delta\phi_b$). **Fig. 3.6b** and **3.6c** illustrate this case-scenario, where holes must overcome a higher barrier in LWF domains before they can be collected by the metallic probe.

We also note that a divergent field might be expected for the probe-sample contact geometry. This effect would be present in case of an Ohmic contact, however, we observed rather a Schottky behavior.[51] Here we assume that the current is limited to the electronic properties of the contact, which will mainly affect to the magnitude of the measured current (~ nA). The current is limited to the injection mechanism and, considering the semiconducting properties of the perovskite, thermionic emission was assumed as the dominant mechanism in forward bias.

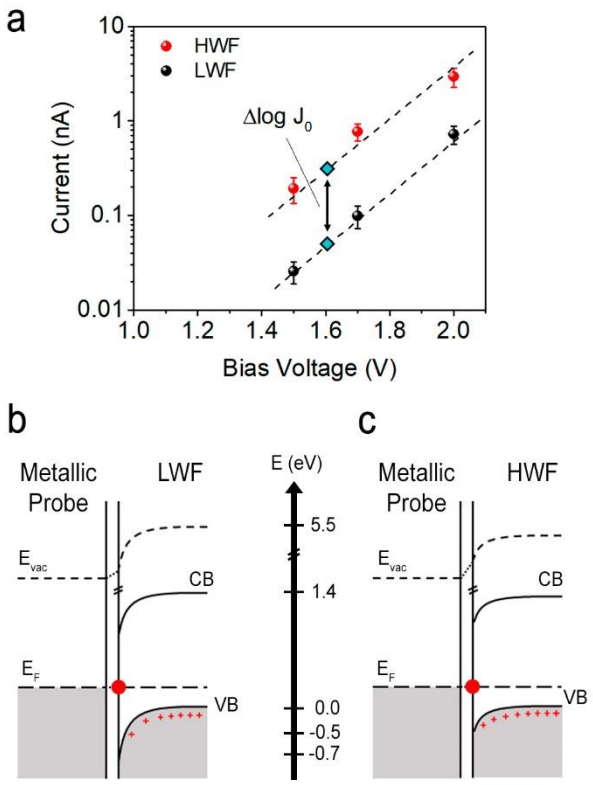

Figure 3.6. *(**a**) Semi-log plot of the bias-dependence of the C-AFM current (measured in contact mode) for the LWF and HWF types of $MAPbI_3$ domains. (**b**) and (**c**) Scheme of the C-AFM band structure of the probe-surface contact for the two types of domains, LWF and HWF at 0 V. The surface states (represented by the red dot) impact the position of the Fermi level at the $MAPbI_3$ surface. There is an interface layer between LWF/HWF and the metallic probe which allows for vacuum level adjustment.*

The effective barriers (ϕ_b) were experimentally extracted from **Fig. 3.6a** and are ~ 0.45 and ~ 0.70 eV for HWF and LWF, respectively. If we consider the measured barrier heights and compare them to the measured WF, the valence band (VB) is found to lie at ~ 5.5 eV for both types of domains. An optical bandgap of 1.58 eV was experimentally determined by UV-visible absorption spectroscopy, **Fig. 3.7a** and **b**. Even if the perovskite films have domains with heterogenous properties, local photoluminescence studies have shown similar emission wavelength for different domains, *i.e.* similar bandgap.[52] Therefore, even if the perovskite film shows heterogeneous WF at the surface, we consider that the optical bandgap remains constant. The obtained bandgap value is in close vicinity to what is traditionally reported in literature, and can be used to determine the position of the conduction band (CB) at the surface ~ 3.9 eV.[46]

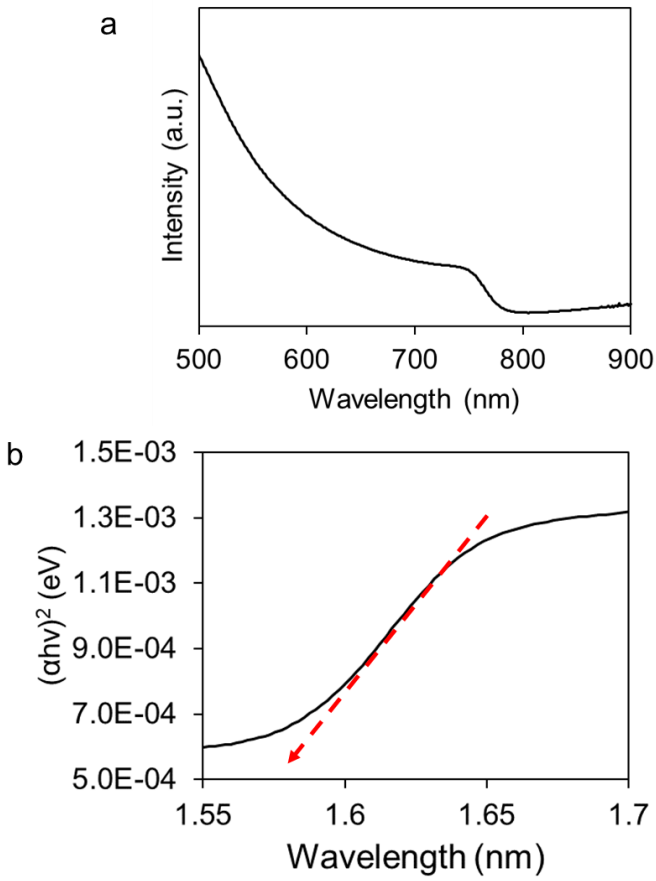

Figure 3.7. ***(a)*** *UV-Vis absorption spectra and (**b**) Tauc plot of the MAPI-$PbAc_2$ sample. The dotted arrows illustrate the fitting of the bandgap at the X-axis intercept.*

The variations of WF and ϕ_b between HWF and LWF domains are also consistent with the p-type semiconducting character of $MAPbI_3$, lower (higher) WF inducing higher (lower) V_{bi}. Generally, the WF and free carrier density (p) are conditioned by the sole crystallinity of the film and play a primary role onto charge collection, determining the injection voltages.[53,54] In this work, however, charge injection/extraction mechanisms are dominating the current response up to much higher injection voltages, indicating significant amount and impact of surface states, hence possible interfacial issues once incorporated in devices.[55,56] This is likely to induce a Fermi level pinning located at the energy level of the traps (4.8 and 5.0 eV as previously shown). In C-AFM, the alignment of the Fermi level is taking place between the probe and the sample in both the LWF and HWF domains with their respective trap energy levels at 0 V. This Fermi level pinning has an impact on the probe-sample contact and can be described with an additional electric field across an interfacial layer as depicted in **Fig. 3.6b** and **c**.

The existence of domains exhibiting different surface states despite similar stoichiometry can be attributed to, at least, two kinds of different perturbing states; they could either be the result of different terminations or the result of the growth procedure. Recent DFT calculations gave insight into the effect of the possible different $MAPbI_3$ terminations.[57] Pure methylammonium(MAI)-terminated (001) surfaces are around 1 eV higher in energy than pure PbI_2-terminated (001) surfaces, both independently affecting the charge injection properties.[58,59] In addition, MAI-terminated surfaces are expected to have a higher bandgap than PbI_2-terminated surfaces.[59] However, given the fact that the two types of domains observed here exhibit similar VB, it is quite unlikely that they would correspond to two different surface terminations. We are therefore led to hypothesize that surface structural defects induced by the growth conditions would cause the observed local electronic heterogeneity. However, at this point we cannot completely discriminate between these two possibilities. The presence of defects will be further examined in **Chapter 5**.

3.3 Alternative $CH_3NH_3PbI_3$ Perovskite

So far, the MAPI-$PbAc_2$ perovskite showed a p-type behavior. In fact, $MAPbI_3$ thin films can be self-doped depending on the ratio between the precursors used in the synthesis process.[60] High (low) concentrations of PbI_2 in the precursor solution makes the final perovskite film to be more n-type (p-type), respectively. Moreover, PEDOT:PSS has a better affinity to PbI_2 than to MAI, so even higher amounts of MAI are necessary to generate a p-type $MAPbI_3$ perovskite on the PEDOT:PSS surface.[61] Previously, we used MAPI-$PbAc_2$, the synthesis of which results in a p-type material. To prepare a n-type perovskite, we used PbI_2 as the precursor, in a 1:1 (PbI_2:MAI) ratio. It is referred as MAPI-PbI_2 (see **section 2.1**) and it corresponds to one of the most typical synthesis routes used in $MAPbI_3$ perovskite solar cells.[62,63]

The MAPI-PbI_2 perovskite surface in this case shows a surface with small grains of ~ 150 nm, **Fig. 3.8a**. This perovskite surface was also characterized by KPFM and C-AFM. The anisotropy in WF and current images is only apparent, that is, the highlighted domains in **Fig. 3.8a**, **b** and **c** are associated to the small peak at zero current observed in the C-AFM current distribution, **Fig. 3.8e**, which corresponds to insulating PbI_2 domains. The presence of PbI_2 domains are confirmed by the small peak at 12.6º in the XRD

diffractogram, **Fig. 3.8f**. Moreover, a narrow WF distribution can be observed in **Fig. 3.8d**.

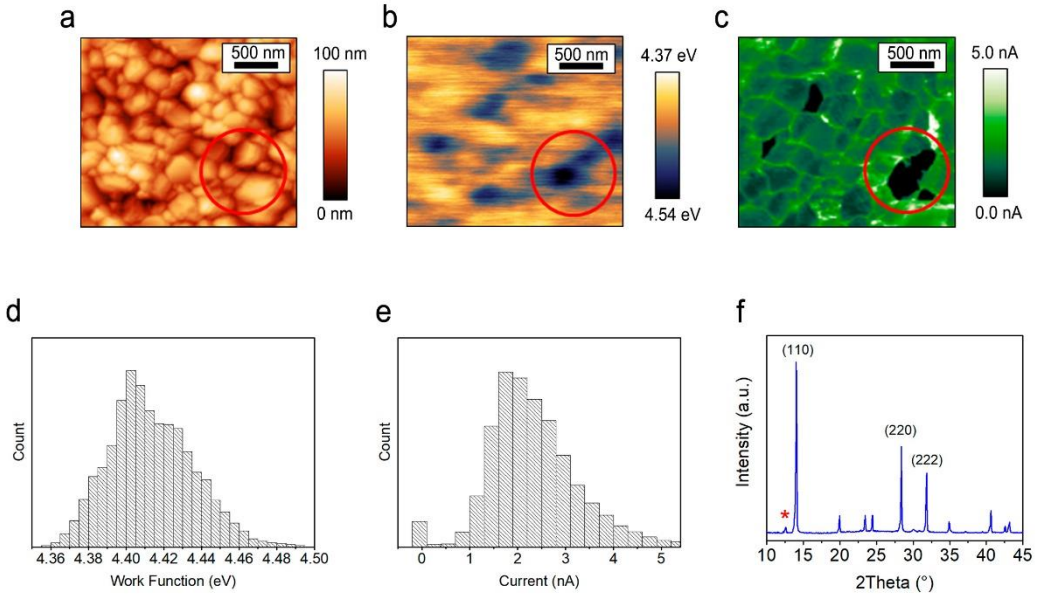

Figure 3.8. ***(a)*** *Height,* ***(b)*** *work function and* ***(c)*** *current (applied bias: 1.5 V) maps of a MAPI–PbI_2 layer deposited on top of PEDOT:PSS. Distribution of the* ***(d)*** *work function map and* ***(e)*** *the current map.* ***(f)*** *XRD diffractogram of the MAPI-PbI_2 sample. Red circles show the same spot.*

As observed in **Fig. 3.8d** (and **Fig. 3.8b**) the WF of the MAPI-PbI_2 lies around 4.4 eV. The bandgap energy is ~ 1.56 eV (**Fig. 3.9a** and **b**), in line with the bandgap reported in literature and, with the previously mentioned energy levels, it implies an n-type behavior for this perovskite film.[3] The approach previously used to reconstruct an I-V curve was also tempted for the MAPI-PbI_2 film in order to confirm the n-type behavior. This technique requires to make several C-AFM scans of the same area at increasing bias voltages after each scan. However, the described procedure is only apparently simple. A negative current was found when scanning at 0 V (note that the measurements are carried out in dark conditions), what means that there is a small parasitic photocurrent, most probably due to the AFM laser beam (680 nm wavelength) used to control the AFM probe motion. In addition, for each C-AFM scan (at different bias voltages) there is a small portion of the image scanned at 0 V, this allows us to check the "base" current prior to apply any voltage. Nonetheless, the negative current for this 0 V tests is increasing after each scan. This odd behavior translates into an increasing photocurrent contribution after

each scan and a misleading I-V curve. However, based on (i) our experimental protocol and (ii) what is regularly and consistently reported in literature, we assume these MAPI-PbI_2 films to exhibit n-type semiconducting properties.

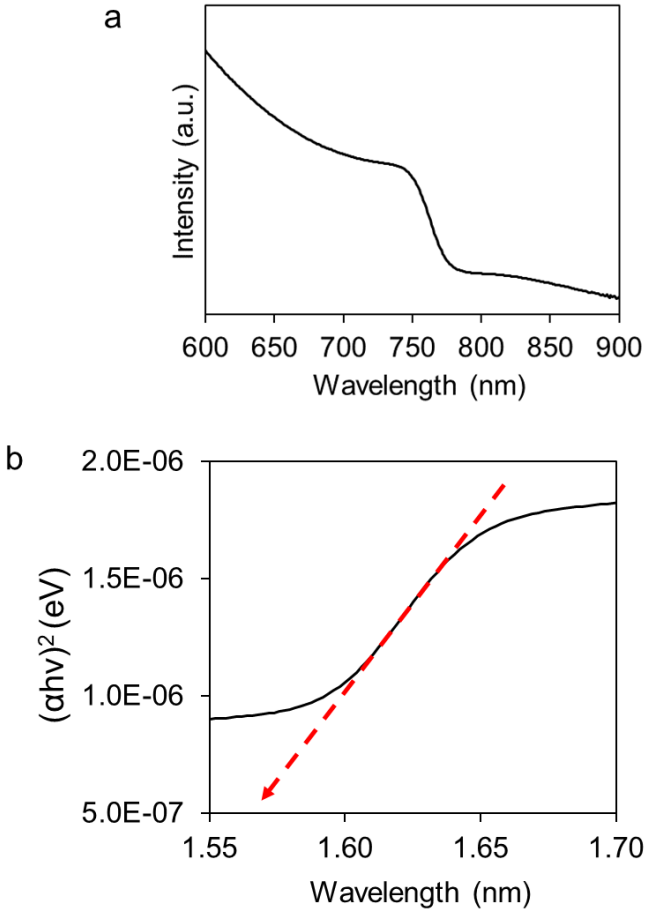

Figure 3.9. ***(a)*** *UV-Vis absorption spectra and* ***(b)*** *Tauc plot of the MAPI-PbI_2 pristine and water exposed samples. The dotted arrows illustrate the fitting of the bandgap at the X-axis intercept.*

Altogether, the MAPI-PbI_2 surface exhibits homogeneous electronic properties (excluding the fact that there are unreacted PbI_2 species) over the surface compared to the MAPI-$PbAc_2$ surface. In MAPI-PbI_2, deep traps were also found, since the average surface WF was ~ 4.4 eV. In this case, since the WF difference is almost negligible, we could assume a certain specific acceptor point defect to be the major defect present on the surface. The discussion about the possible defect candidates will be further discussed in **Chapter 5**.

3.4 Conclusions

In contrast to previous literature reports, we have demonstrated that even if MAPI-$PbAc_2$ perovskite films show a very high crystalline structure seen by XRD diffractograms, they can show regions with up to 0.2 eV WF difference. We discriminated between two different regions, HWF and LWF, where LWF regions have a surface WF closer to the mid-gap, hindering carrier injection/extraction at the surface, hence the charge transport in the film. We proposed either surface terminations or surface point defects to be the cause of these electronic local variations. Since the bandgap is expected to remain unaltered through the perovskite surface, it is unlikely that surface defects are causing such a WF perturbation. We then suggest a heterogeneous distribution of point defects over the MAPI-$PbAc_2$ surface. In contrast, when using lead iodide as a precursor (MAPI-PbI_2), the WF distribution over the surface appears to be much more homogeneous. Interestingly, even though the WF is more homogeneous in this perovskite film, the average surface WF indicates the presence of deep traps too. The determination of the surface traps will be further discussed in **Chapter 5** devoted to the evolution of the surface under water contamination.

References

1. Kojima, A., Teshima, K., Shirai, Y. & Miyasaka, T. Organometal Halide Perovskites as Visible-Light Sensitizers for Photovoltaic Cells. *J. Am. Chem. Soc.* **131**, 6050–6051 (2009).

2. Jiang, Q. *et al.* Surface passivation of perovskite film for efficient solar cells. *Nat. Photonics* **13**, 460–466 (2019).

3. Lee, M. M., Teuscher, J., Miyasaka, T., Murakami, T. N. & Snaith, H. J. Efficient hybrid solar cells based on meso-superstructured organometal halide perovskites. *Science* **338**, 643–647 (2012).

4. Wehrenfennig, C., Eperon, G. E., Johnston, M. B., Snaith, H. J. & Herz, L. M. High charge carrier mobilities and lifetimes in organolead trihalide perovskites. *Adv. Mater. Weinheim* **26**, 1584–1589 (2014).

5. Zhumekenov, A. A. *et al.* Formamidinium Lead Halide Perovskite Crystals with Unprecedented Long Carrier Dynamics and Diffusion Length. *ACS Energy Lett.* **1**, 32–37 (2016).

6. Tian, W., Zhao, C., Leng, J., Cui, R. & Jin, S. Visualizing Carrier Diffusion in Individual Single-Crystal Organolead Halide Perovskite Nanowires and Nanoplates. *J. Am. Chem. Soc.* **137**, 12458–12461 (2015).

7. Miyata, K. *et al.* Large polarons in lead halide perovskites. *Science Advances* **3**, e1701217 (2017).

8. Batignani, G. *et al.* Probing femtosecond lattice displacement upon photo-carrier generation in lead halide perovskite. *Nat Commun* **9**, 1971 (2018).

9. Wang, R. *et al.* A Review of Perovskites Solar Cell Stability. *Advanced Functional Materials* **29**, 1808843 (2019).

10. Mesquita, I., Andrade, L. & Mendes, A. Perovskite solar cells: Materials, configurations and stability. *Renewable and Sustainable Energy Reviews* **82**, 2471–2489 (2018).

11. Yun, J. S. *et al.* Critical Role of Grain Boundaries for Ion Migration in Formamidinium and Methylammonium Lead Halide Perovskite Solar Cells. *Advanced Energy Materials* **6**, 1600330 (2016).

12. Shao, Y. *et al.* Grain boundary dominated ion migration in polycrystalline organic–inorganic halide perovskite films. *Energy Environ. Sci.* **9**, 1752–1759 (2016).

13. Du, M.-H. Density Functional Calculations of Native Defects in CH3NH3PbI3: Effects of Spin–Orbit Coupling and Self-Interaction Error. *J. Phys. Chem. Lett.* **6**, 1461–1466 (2015).

14. Chen, B., Yang, M., Priya, S. & Zhu, K. Origin of J–V Hysteresis in Perovskite Solar Cells. *J. Phys. Chem. Lett.* **7**, 905–917 (2016).

15. Kong, W., Ding, T., Bi, G. & Wu, H. Optical characterizations of the surface states in hybrid lead–halide perovskites. *Phys. Chem. Chem. Phys.* **18**, 12626–12632 (2016).

16. Snaith, H. J. *et al.* Anomalous Hysteresis in Perovskite Solar Cells. *J Phys Chem Lett* **5**, 1511–1515 (2014).

17. Wu, X. *et al.* Trap States in Lead Iodide Perovskites. *J. Am. Chem. Soc.* **137**, 2089–2096 (2015).

18. Xiao, Z. *et al.* Efficient, high yield perovskite photovoltaic devices grown by interdiffusion of solution-processed precursor stacking layers. *Energy Environ. Sci.* **7**, 2619–2623 (2014).

19. Shi, D. *et al.* Solar cells. Low trap-state density and long carrier diffusion in organolead trihalide perovskite single crystals. *Science* **347**, 519–522 (2015).

20. Buin, A. *et al.* Materials Processing Routes to Trap-Free Halide Perovskites. *Nano Lett.* **14**, 6281–6286 (2014).

21. Nie, W. *et al.* Solar cells. High-efficiency solution-processed perovskite solar cells with millimeter-scale grains. *Science* **347**, 522–525 (2015).

22. Chen, J., Zhao, X., Kim, S.-G. & Park, N.-G. Multifunctional Chemical Linker Imidazoleacetic Acid Hydrochloride for 21% Efficient and Stable Planar Perovskite Solar Cells. *Advanced Materials* **31**, 1902902 (2019).

23. Son, D. Y. *et al.* Self-formed grain boundary healing layer for highly efficient CH3 NH3 PbI3 perovskite solar cells. *Nature Energy* **1**, 16081 (2016).

24. Braly, I. L. *et al.* Hybrid perovskite films approaching the radiative limit with over 90% photoluminescence quantum efficiency. *Nature Photon* **12**, 355–361 (2018).

25. Grévin, B. Kelvin Probe Force Microscopy Characterization of Organic and Hybrid Perovskite Solar Cells. *Springer* (2018).

26. Bergmann, V. W. *et al.* Local Time-Dependent Charging in a Perovskite Solar Cell. *ACS Appl Mater Interfaces* **8**, 19402–19409 (2016).

27. Bergmann, V. W. *et al.* Real-space observation of unbalanced charge distribution inside a perovskite-sensitized solar cell. *Nat Commun* **5**, 5001 (2014).

28. Garrett, J. L. *et al.* Real-Time Nanoscale Open-Circuit Voltage Dynamics of Perovskite Solar Cells. *Nano Lett.* **17**, 2554–2560 (2017).

29. Moerman, D., Eperon, G. E., Precht, J. T. & Ginger, D. S. Correlating Photoluminescence Heterogeneity with Local Electronic Properties in Methylammonium Lead Tribromide Perovskite Thin Films. *Chem. Mater.* **29**, 5484–5492 (2017).

30. Yun, J. S. *et al.* Benefit of Grain Boundaries in Organic-Inorganic Halide Planar Perovskite Solar Cells. *J Phys Chem Lett* **6**, 875–880 (2015).

31. She, L., Liu, M. & Zhong, D. Atomic Structures of CH3NH3PbI3 (001) Surfaces. *ACS Nano* **10**, 1126–1131 (2016).

32. Kim, D. *et al.* Probing Facet-Dependent Surface Defects in MAPbI3 Perovskite Single Crystals. *J. Phys. Chem. C* **123**, 14144–14151 (2019).

33. R. Harwell, J. *et al.* Probing the energy levels of perovskite solar cells via Kelvin probe and UV ambient pressure photoemission spectroscopy. *Physical Chemistry Chemical Physics* **18**, 19738–19745 (2016).

34. Stecker, C. *et al.* Surface Defect Dynamics in Organic-Inorganic Hybrid Perovskites: From Mechanism to Interfacial Properties. *ACS Nano* **13**, 12127–12136 (2019).

35. Gallet, T., Grabowski, D., Kirchartz, T. & Redinger, A. Fermi-level pinning in methylammonium lead iodide perovskites. *Nanoscale* **11**, 16828–16836 (2019).

36. Yin, W.-J., Shi, T. & Yan, Y. Unusual defect physics in CH3NH3PbI3 perovskite solar cell absorber. *Appl. Phys. Lett.* **104**, 063903 (2014).

37. Du, M. H. Efficient carrier transport in halide perovskites: theoretical perspectives. *J. Mater. Chem. A* **2**, 9091–9098 (2014).

38. Colchero, J., Gil, A. & Baró, A. M. Resolution enhancement and improved data interpretation in electrostatic force microscopy. *Phys. Rev. B* **64**, 245403 (2001).

39. Si, H. *et al.* Emerging Conductive Atomic Force Microscopy for Metal Halide Perovskite Materials and Solar Cells. *Advanced Energy Materials* **10**, 1903922 (2020).

40. Lee, J.-W. *et al.* A Bifunctional Lewis Base Additive for Microscopic Homogeneity in Perovskite Solar Cells. *Chem* **3**, 290–302 (2017).

41. Zhang, W. *et al.* Enhanced optoelectronic quality of perovskite thin films with hypophosphorous acid for planar heterojunction solar cells. *Nat Commun* **6**, 10030 (2015).

42. Zhang, W. *et al.* Ultrasmooth organic-inorganic perovskite thin-film formation and crystallization for efficient planar heterojunction solar cells. *Nat Commun* **6**, 6142 (2015).

43. Ahmad, Z. *et al.* Instability in CH 3 NH 3 PbI 3 perovskite solar cells due to elemental migration and chemical composition changes. *Sci Rep* **7**, 1–8 (2017).

44. Stoumpos, C. C., Malliakas, C. D. & Kanatzidis, M. G. Semiconducting Tin and Lead Iodide Perovskites with Organic Cations: Phase Transitions, High Mobilities, and Near-Infrared Photoluminescent Properties. *Inorg. Chem.* **52**, 9019–9038 (2013).

45. Docampo, P. *et al.* Influence of the orientation of methylammonium lead iodide perovskite crystals on solar cell performance. *APL Materials* **2**, 081508 (2014).

46. Kim, H.-S. *et al.* Lead iodide perovskite sensitized all-solid-state submicron thin film mesoscopic solar cell with efficiency exceeding 9%. *Sci Rep* **2**, 591 (2012).

47. Caputo, M. *et al.* Electronic structure of MAPbI 3 and MAPbCl 3 : importance of band alignment. *Scientific Reports* **9**, 15159 (2019).

48. Endres, J. *et al.* Valence and Conduction Band Densities of States of Metal Halide Perovskites: A Combined Experimental–Theoretical Study. *J. Phys. Chem. Lett.* **7**, 2722–2729 (2016).

49. Tao, S. *et al.* Absolute energy level positions in tin- and lead-based halide perovskites. *Nature Communications* **10**, 2560 (2019).

50. Rhoderick, E. H. & Williams, R. H. *Metal-semiconductor contacts*. (Clarendon Press ; Oxford University Press, 1988).

51. Moerman, D. *et al.* Towards a unified description of the charge transport mechanisms in conductive atomic force microscopy studies of semiconducting polymers. *Nanoscale* **6**, 10596–10603 (2014).

52. Quilettes, D. W. de *et al.* Impact of microstructure on local carrier lifetime in perovskite solar cells. *Science* **348**, 683–686 (2015).

53. Shi, L. X. *et al.* The effects of interfacial recombination and injection barrier on the electrical characteristics of perovskite solar cells. *AIP Advances* **8**, 025312 (2018).

54. Jiménez-López, J., Cambarau, W., Cabau, L. & Palomares, E. Charge Injection, Carriers Recombination and HOMO Energy Level Relationship in Perovskite Solar Cells. *Sci Rep* **7**, 1–10 (2017).

55. Dharmadasa, I. M. Fermi level pinning and effects on CuInGaSe2-based thin-film solar cells. *Semicond. Sci. Technol.* **24**, 055016 (2009).

56. Colleoni, D., Miceli, G. & Pasquarello, A. Fermi-level pinning through defects at GaAs/oxide interfaces: A density functional study. *Phys. Rev. B* **92**, 125304 (2015).

57. Mosconi, E., Azpiroz, J. M. & De Angelis, F. Ab Initio Molecular Dynamics Simulations of Methylammonium Lead Iodide Perovskite Degradation by Water. *Chem. Mater.* **27**, 4885–4892 (2015).

58. Haruyama, J., Sodeyama, K., Han, L. & Tateyama, Y. Termination Dependence of Tetragonal CH3NH3PbI3 Surfaces for Perovskite Solar Cells. *J. Phys. Chem. Lett.* **5**, 2903–2909 (2014).

59. Quarti, C., De Angelis, F. & Beljonne, D. Influence of Surface Termination on the Energy Level Alignment at the CH3NH3PbI3 Perovskite/C60 Interface. *Chem. Mater.* **29**, 958–968 (2017).

60. Wang, Q. *et al.* Qualifying composition dependent p and n self-doping in CH3NH3PbI3. *Appl. Phys. Lett.* **105**, 163508 (2014).

61. Wang, Q. *et al.* Large fill-factor bilayer iodine perovskite solar cells fabricated by a low-temperature solution-process. *Energy Environ. Sci.* **7**, 2359–2365 (2014).

62. Heo, J. H. *et al.* Efficient inorganic–organic hybrid heterojunction solar cells containing perovskite compound and polymeric hole conductors. *Nature Photon* **7**, 486–491 (2013).

63. Kim, H.-S. *et al.* Mechanism of carrier accumulation in perovskite thin-absorber solar cells. *Nat Commun* **4**, 2242 (2013).

Chapter 4

$CH_3NH_3PbI_3$ Perovskite Thin Film Capacitance Study at the Nanoscale

Characterization of the electrical properties semiconductors at the nanoscale is sometimes limited in terms of properties that can be measured. In this Chapter, we look further into local capacitance by means of scanning microwave microscopy. To do so, we use a calibration method that does not require additional calibration samples. Furthermore, a first study of the local capacitance of two kind of perovskite surfaces is carried out. Such local studies can help to distinguish different behaviours over the semiconductor surface.

4.1 Introduction

The remaining uncertainty about the chemical properties at the perovskite surface can be a potential factor that limits the approaches when trying to improve the perovskite-based devices. Therefore, it is essential to fully understand what processes are taking place at the perovskite surface to, later, understand the behavior at the interface between the perovskite and a given transport layer.

One of the limitations when measuring surface properties is the size of the measurement. Measuring electronic local properties in the order of few nanometers presents a challenge and it becomes harder when several measurements of different nature are required in the same nanometer-sized spot. While it exists a number of SPM-based techniques to test small features in perovskite devices, as described in **Chapter 2**, studies reporting local capacitance properties are still very limited. Impedance spectroscopy measurements have been shown to be a powerful method to determine the capacitance and the processes taking place at different parts of the device, yet it remains a macroscopic measurement.[1,2] For photovoltaic applications, the main interest in capacitive measurements is to be able to know more about conductivity, diffusion lengths and/or carrier lifetimes.

In order to understand the local capacitive effects, scanning microwave microscopy (SMM) could be a useful technique. SMM can detect small variations in the reflected microwave signal and it has been used in the microelectronics industry, for instance, to distinguish different doping levels.[3] However, while it has been proven to be a reliable technique to detect local capacitive features, meaningful studies with perovskite-based devices are lacking.[4]

In this chapter, preliminary SMM measurements have been carried out in order to study the local capacitive variations on both routes previously described in $MAPbI_3$ seen in **Chapter 3**. Two different systems were used, on one side the SMM 5600LS by Keysight Technologies, in the other side, the IEMN-made SMM allowing us to work under vacuum conditions and to avoid moisture degradation.

4.2 Topography Crosstalk

For this section, 5 nm of Al_2O_3 were deposited on top of the perovskite layer (see **section 2.1**). The SMM was operated in ambient conditions so the insulating layer prevented the moisture interacting with the perovskite surface while measuring the electronic local properties. Since the operating SMM frequency influences the depth of analysis, all the SMM measurements were carried out at 18.1 GHz. At such high frequency, the wave penetration is weaker so the measurement remains located at the surface.[5]

Fig. 4.1a shows the topography of a MAPI-$PbAc_2$ surface (**section 2.1**), with an average grain size of ~ 250 nm. **Fig. 4.1b** shows the $|S_{11}|$ image, which was recorded simultaneously with a microwave frequency of 18.2 GHz. Interestingly, comparing each pixel from **Fig. 4.1a** to each corresponding pixel in **Fig. 4.1b**, a dominant trend can be observed, **Fig. 4.1c**. These results suggest an important influence of the stray capacitance on the $|S_{11}|$ images, **Fig. 4.2a**, causing a topography crosstalk. That is, a higher $|S_{11}|$ signal at lower topography heights.

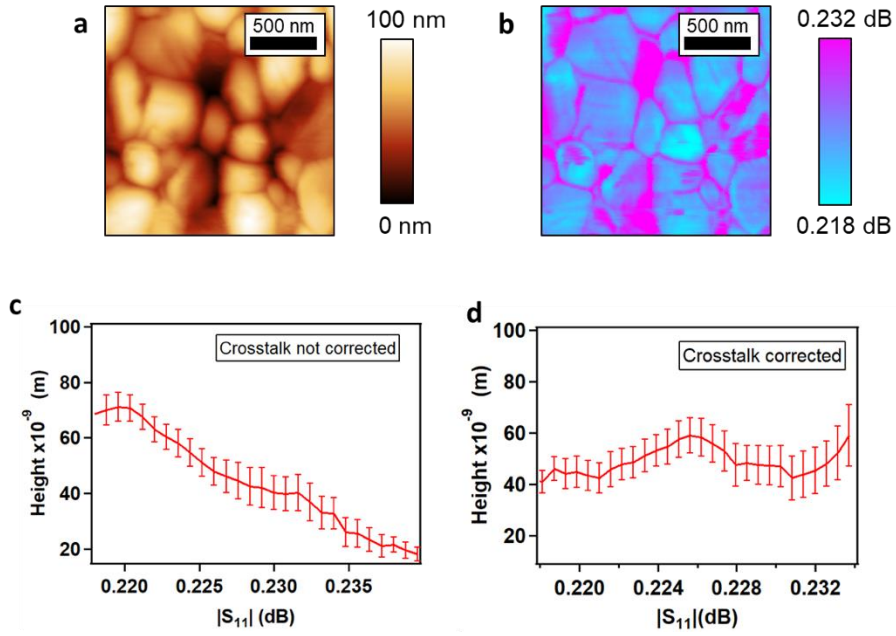

Figure 4.1. *(**a**) Topography and (**b**) $|S_{11}|$ image of the MAPI-$PbAc_2$ perovskite in contact mode performed in SMM. Height vs $|S_{11}|$ pixel relationship (**c**) before and (**d**) after regression correction.*

The dependence behavior between the capacitance and the probe-sample distance can be determined through an approach curve as in **Fig. 4.2b**. The capacitance was determined

following the EFM calibration procedure on **section 2.2.7 – *EFM calibration*** for S_{11} measurements and, as a result, a linear trend was approximated from **Fig. 4.2b**. Notice that after the probe contacts the sample, the capacitance keeps increasing, this might be due to geometrical changes in the probe tip or due to the bending of the cantilever. In order to minimize the topographical contributions on the SMM measurements, the following linear regression was systematically used for this purpose:[4]

$$|S_{11}| = \alpha + \beta_1 * z(x,y) + \beta_2 * \nabla^2 z(x,y) \quad (4.1)$$

where z (x,y) is the topography height, ∇^2z (x,y) is the Laplacian of the topography and α, β_1 and β_2 are determined from the regression method. The Laplacian operator was introduced to correct the local curvature that is typically found in AFM scans. **Fig. 4.1d** shows the same $|S_{11}|$ vs topography height after applying the linear regression.

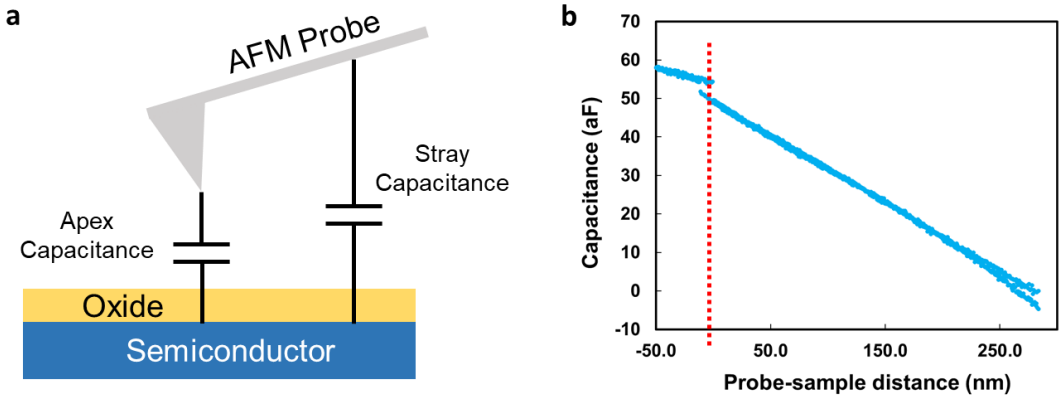

Figure 4.2. *(**a**) Schematics of the capacitance contributions between the probe and the sample, (**b**) Capacitance dependence on the probe-sample distance, the dotted line represents when the probe contacts the sample.*

In **Fig. 4.3a** and **b**, the $|S_{11}|$ can be observed before and after crosstalk correction, respectively. The correction allowed to decrease the signal from grain boundaries, which use to be problematic points for the probe-surface interaction and result in small artifacts. Even after crosstalk correction, it becomes evident that there is a contrast over the perovskite surface. In the $|S_{11}|$ histogram, **Fig. 4.3c**, we could distinguish 2 populations at 0.223 dB and 0.229 dB. This contrast is interestingly similar to the contrast observed for the same MAPI-$PbAc_2$ surfaces in **Chapter 3**, plotted in **Fig. 4.3d**. In **Chapter 3**, the discussion was around the possibility to have different surface defects, leading to a work function difference.

Making work function and $|S_{11}|$ images at the same spot could lead us to distinguish between the different populations. Such a study could be done by different ways, one of them consists to mark a nanometric spot with an AFM tip so when the WF map is measured, the spot can be found later when moving the sample to the SMM system. Nonetheless, the camera in the SMM system does not provide sharp enough images, making it very difficult to find the nanometric spot. Another way to perform such study would be to measure simultaneously the KPFM and SMM signals. Nonetheless, each technique is performed with different AFM probes; the resonant frequency for the KPFM probes used in this work is ~ 75 kHz while for SMM probes it is ~ 9 kHz. Therefore, either upgrading the camera system or making an AFM probe that could work with both modes would really represent a big improvement for SMM measurements.

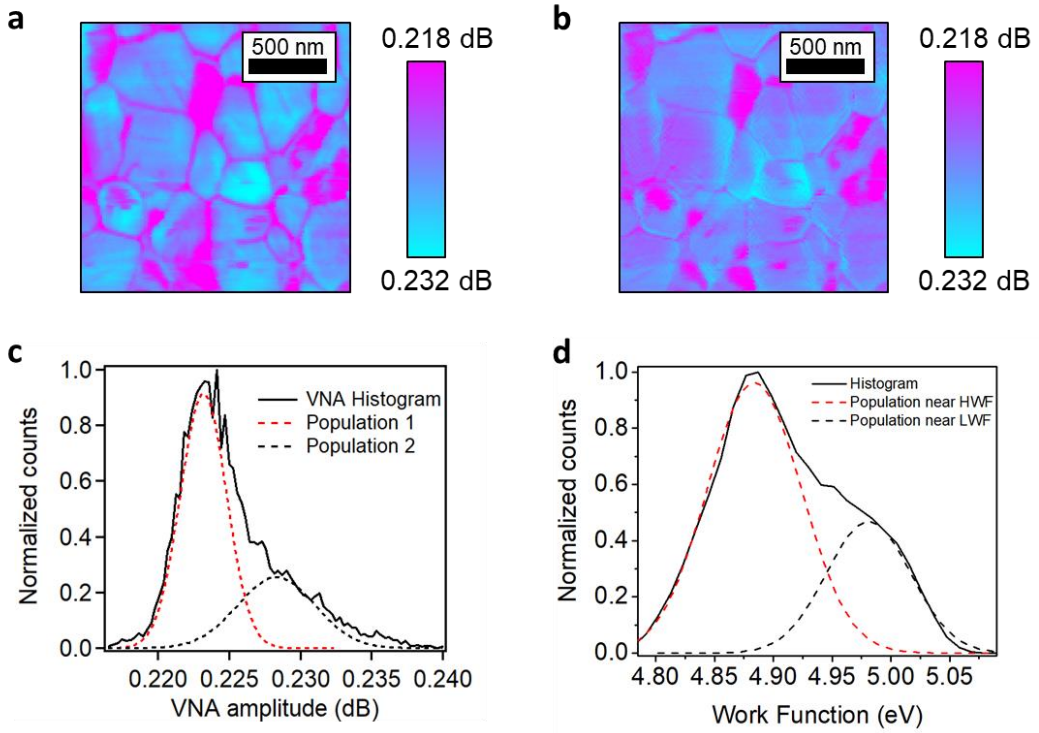

Figure 4.3. ***(a)*** *Raw and* ***(b)*** *corrected* $|S_{11}|$ *signals from the MAPI-*$PbAc_2$ *surface.* ***(c)*** $|S_{11}|$ *histogram and (d) work function histogram for the MAPI-*$PbAc_2$ *perovskite surface (two different samples).*

4.3 Calibration for Capacitance Measurements

The S_{11} signal can be converted to capacitance following the EFM calibration procedure described in **section 2.2.7 – *EFM calibration***. EFM calibration has been published and it is extensively used in literature, however, it is necessary to have the capability to make EFM and S_{11} measurements at the same time in order to get a calibrated sample.[6] This is actually a limitation for this work. S_{11} measurements were first performed in the Keysight SMM system where EFM measurements could be done through the AFM integrated capabilities, however, another SMM system was built by the IEMN with the added advantage of being operated under vacuum conditions. In this later system, the EFM measurements were not integrated just yet. Therefore, an alternative calibration technique was needed.

Calibration is a fundamental aspect generally in all kind of measurements, however, especially here it is a limiting factor. The most straightforward method to calibrate the measurements would be to measure the S_{11} signal in another well-known sample of similar characteristics, and it is a usual method usually performed with samples such as silicon or other materials.[7,8] Nonetheless, with other materials such as perovskites, it is complicated to find a reference sample with similar characteristics. In addition, the fact of using several samples implies that the probe-sample distance will be different in each case, therefore, sometimes it is not the most reliable way to calibrate the S_{11} measurements. IEMN developed a calibration method, so-called interferometric calibration, in which the S_{11} signal is recorded in a range of frequencies once the probe is in contact with the sample and prior to make any measurement, see **section 2.2.7 – *Interferometric calibration*** for further details. This technique does not need any additional measurement mode.

Therefore, the interferometric calibration was tested together with the EFM calibration just by measuring an approach-retract curve on a $MAPbI_3$ perovskite sample. In **Fig. 4.4** the results show negative capacitance values for the interferometric model. However, the results for the interferometric model had to be adjusted by adding an additional capacitance of around 1 pF in order to show a correct trend, that is, a higher capacitance close to the surface. This additional capacitance is rather high compared to what it is expected to be measured on the sample (~ fF), therefore, it should be due to some parasitic effect due to the instrumentation, probably caused in the SMM head. It could be that the

propagation of the high frequencies between the coaxial cable and the sample play an important role. Such complex propagation schemes may be difficult to solve and would require electromagnetic 3D modelling (COMSOL Multiphysics for instance).

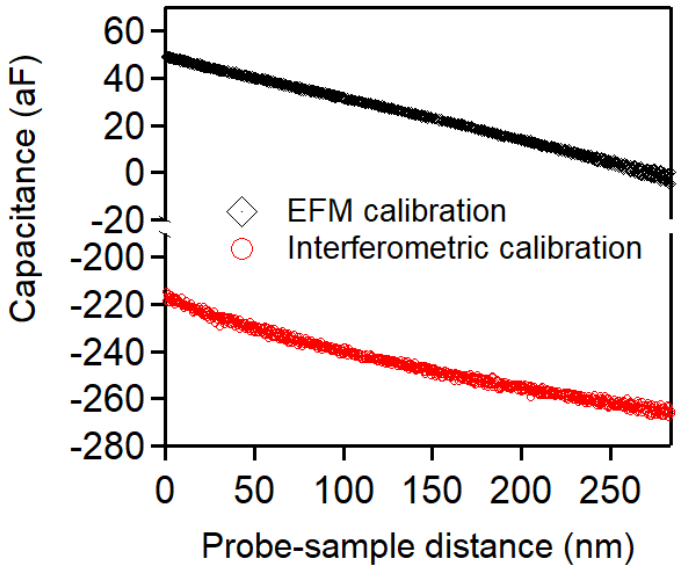

Figure 4.4. *Capacitance measurements calibrated with the EFM and interferometric models.*

Even though, regardless of the uncertainty of the capacitance values calculated using the interferometric calibration, it can provide a qualitative analysis which can be helpful to distinguish the local capacitive behaviour without needing to use an additional reference sample nor any additional AFM mode. Therefore, this will be the used calibration technique for the capacitance measurements in the next sections.

4.4 Local Capacitance

To further study the origin of the $|S_{11}|$ contrast seen in **Fig. 4.3**, the capacitance values were determined following the before-mentioned interferometric calibration model. The resulting capacitance image, **Fig. 4.5b,** shows a heterogeneous capacitance over the MAPI-$PbAc_2$ surface. The capacitance heterogeneity may be due to a variation in the surface perovskite properties such as: carrier density, carrier type or defects.

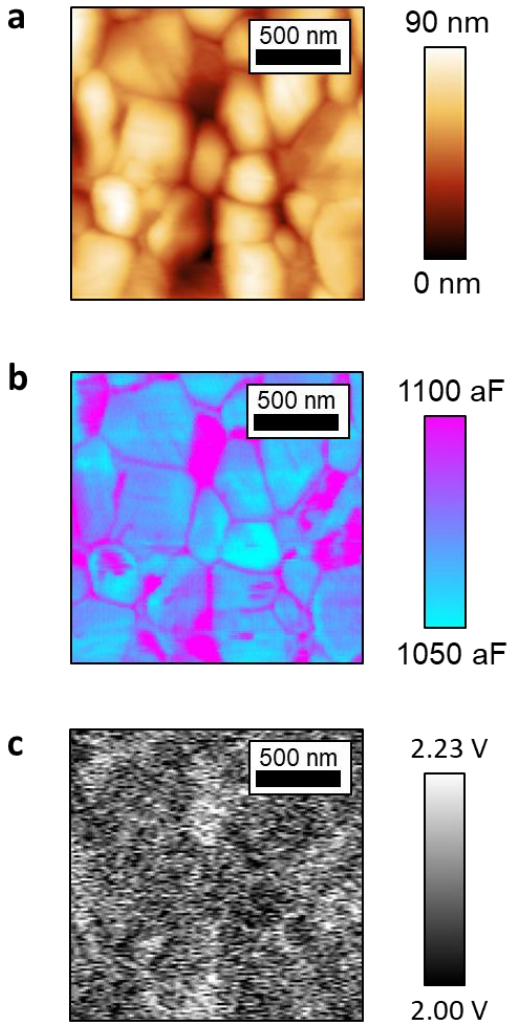

Figure 4.5. *(**a**) Topography, (**b**) local capacitance image determined from the corrected S_{11} signal and (**c**) differential capacitance image on the MAPI-$PbAc_2$ surface.*

However, one would wonder if the capacitance being probed in **Fig. 4.5b** is either a geometrical capacitance or a capacitance driven by the perovskite properties. Ideally, a way to exclude the implication of other films in the capacitance measurements and to further confirm that the perovskite properties are behind the capacitive contrast, would be to make dC/dV maps. **Fig. 4.5c** shows the dC/dV signal of the same sample, which was simultaneously recorded with the S_{11} and topography signals. Comparing the dC/dV signal with the S_{11} signal, it results in a less but not negligible contrasted dC/dV image. Unfortunately, the resolution of the measurement and the small difference between domains prevents us to draw any reliable conclusion with dC/dV measurements. Nonetheless, from **Chapter 3** we know that MAPI-$PbAc_2$ shows heterogeneous electronic properties due to different kind of defects. Therefore, these local capacitance

images serve as preliminary results leading us to think that defects present on the surface are creating a capacitance difference, probably due to a difference in their defect densities.

Since we could not combine KPFM and SMM at the same location, a C-V curve could ultimately help us to distinguish between n or p-type behavior in the different perovskite surfaces: MAPI-$PbAc_2$ and MAPI-PbI_2. To perform this study the SMM system was used under vacuum conditions so no insulating layer was necessary, see **Fig. 2.18a**. As for the C-V measurements, we found that taking multiple images of the same 2 x 2 μm spot and, varying the applied voltage sent to the tip, was the best method to obtain reliable capacitance measurements. The S_{11} values from the images taken at each bias voltage were averaged. Then the S_{11} values were converted to admittance values following **Eq. 2.34**, and then converted to capacitance values by taking the imaginary part of the admittance. Although this calibration model does not provide quantitative results, it is still useful to qualitatively compare the local capacitance. First, the MAPI-$PbAc_2$ perovskite layer was tested, which topography and derived capacitance can be seen in **Fig. 4.5a** and **b**, respectively. While the topography shows the typical grain size for the MAPI-$PbAc_2$ synthesis route (**Fig 4.6a**), the capacitance (**Fig. 4.6b**) seems to be less contrasted compared to the previous MAPI-$PbAc_2$ layer shown in **Fig. 4.5b**. In fact, depending on the working conditions while growing the perovskite, the contrast may change significantly. Also, the resolution for this study was decreased down to 64 $pixels^2$, so the measurement may not detect eventual local variations as much as in **Fig. 4.5** (resolution of 128 $pixels^2$). The resolution was decreased in order to decrease the time needed to make multiple S_{11} maps. Nonetheless, the purpose of this study was to test the capabilities of the SMM system and to track any capacitance change that the perovskite may show upon voltage variation.

Then, the capacitance was averaged for the MAPI-$PbAc_2$ maps at different applied bias voltages, **Fig. 4.7a**. Also, the C-V measurements were done twice as to be sure about the reproducibility, being both measurements very similar. A remarkable divergence between forward and reverse measurements can be easily noticed, *a priori* indicating a hysteresis effect. Given the hysteretic evidences in $MAPbI_3$ perovskites (**see section 1.3.3**), it lead us to think that the capacitance is mostly coming from the perovskite layer.

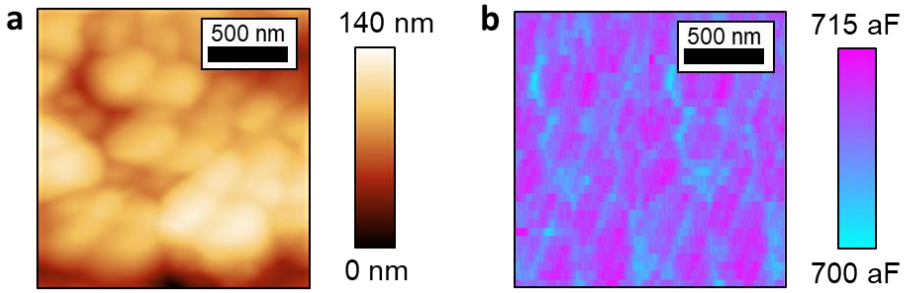

Figure 4.6. *(**a**) Topography and (**b**) derived capacitance from the S_{11} signal for a MAPI-$PbAc_2$ surface.*

Also, the current was tracked for the same voltage range as the C-V measurements but in another MAPI-PbAc2 sample, **Fig. 4.7b**. As a result, the current shows the HWF and LWF regions as in **Chapter 3**, and it does not seem to be affected by hysteresis effects. Nonetheless, the current is very small especially for LWF regions, therefore, a hysteresis effect may be harder to detect than in SMM.

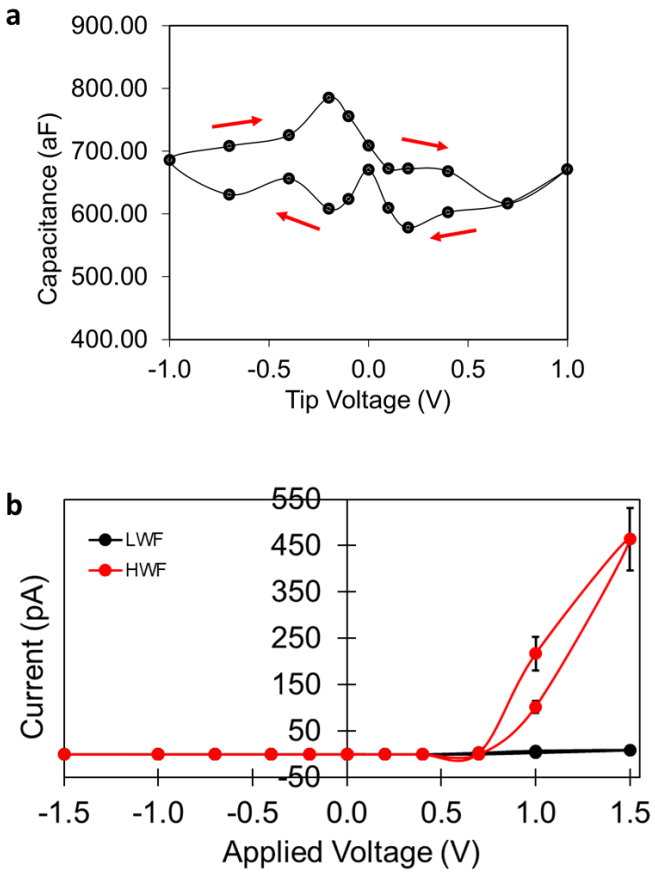

Figure 4.7. *(**a**) Capacitance and (**c**) current vs voltage in two different MAPI-$PbAc_2$ perovskite samples.*

Next, the MAPI-PbI_2 was also characterized by SMM, **Fig. 4.8**. The small perovskite grains are typical for this perovskite synthesis route, as seen in **Chapter 3** and, the capacitance appears to be homogeneous, same as the current maps shown in **Chapter 3** (see **Fig. 3.8**) when compared to the current maps for MAPI-$PbAc_2$ (see **Fig. 3.2**). Surprisingly, the capacitance variation with bias voltage shows a more pronounced hysteresis compared to MAPI-$PbAc_2$, **Fig. 4.9a**. In order to confirm the hysteresis effect, current vs voltage images were recorded as in **Fig. 4.9b**, but when looking to the current variation it does not seem to be as much hysteretic. Nonetheless, MAPI-PbI_2 is expected to be n-type (as explained in **Chapter 3)**, but here we found positive current for positive voltages. This was previously studied by Bowring *et al.* and they found that mobile ions accumulate at the contact and are responsible for the current flowing in reverse bias, this may result in a decrease in efficiency.[9] Defects can be also considered as mobile ions, from **Chapter 3** we know MAPI-PbI_2 has an n-type character, thus, the defects are most probably either V_{Pb} and/or I_i. For the p-type MAPI-$PbAc_2$ perovskite surface, the most probable defects to be present are either V_I and/or MA_i.

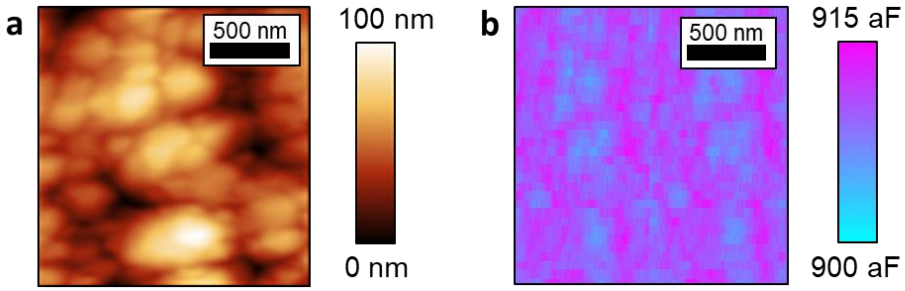

Figure 4.8. ***(a)*** *Topography and* ***(b)*** *derived capacitance from the S_{11} signal for a MAPI-PbI_2 surface.*

In fact, I_i are believed to be the main source of trapping charges in $MAPbI_3$.[10,11] Yang *et al.* found that V_I has lower formation energy than MA_i and I_i and also are fast diffusion defects. Therefore, they concluded that V_I should be the primary contributor to ionic conductivity in $MAPbI_3$.[12] Nonetheless, V_I can show different activation energies depending on the device architecture. For instance, while Eames *et al.* found 0.6 eV for the I_i activation energy in TiO_2/$MAPbI_3$/Spiro-OMeTAD/Au, Bryant *et al.* found that it is takes only 0.12 eV for I_i to be active in PEDOT:PSS/$MAPbI_3$/PCBM/LiF/Ag.[13,14] On the other hand, Yang *et al.* found a high ion conduction caused by iodide ions, which could lead us to thing that it is rather I_i the defects causing the high hysteresis.[15]

This discrepancy in activation energies and diffusion ions make it hard to draw any conclusion from our results. In addition, in our case, with a device structure such as PEDOT:PSS/$MAPbI_3$/PtIr, the activation energies may be also different, thus, it remains an open question whether the high hysteresis in C-V curves is caused by I_i or by other species. As discussed in **Chapter 1**, hysteresis can be induced by several phenomena, and, from the I-V measurements from **Fig. 4.9b** and with the before mentioned literature, we could think about mobile ions inducing a hysteretic capacitance, however, at this point we cannot discard other phenomena. In order to confirm mobile ions or defects as the cause of the hysteresis, a more detailed and exhaustive study of this material should be done. For instance, impedance spectroscopy measurements may help to detect and/or compare the capacitance with the capacitance measured with the SMM. Also, DFT calculations on the activation energies for defects in our device architecture would point towards specific defects, therefore, a specific study could be done. Nonetheless, it has to be pointed that SMM measurements would be an interesting technique to detect hysteretic properties at the local scale when combining it with other studies.

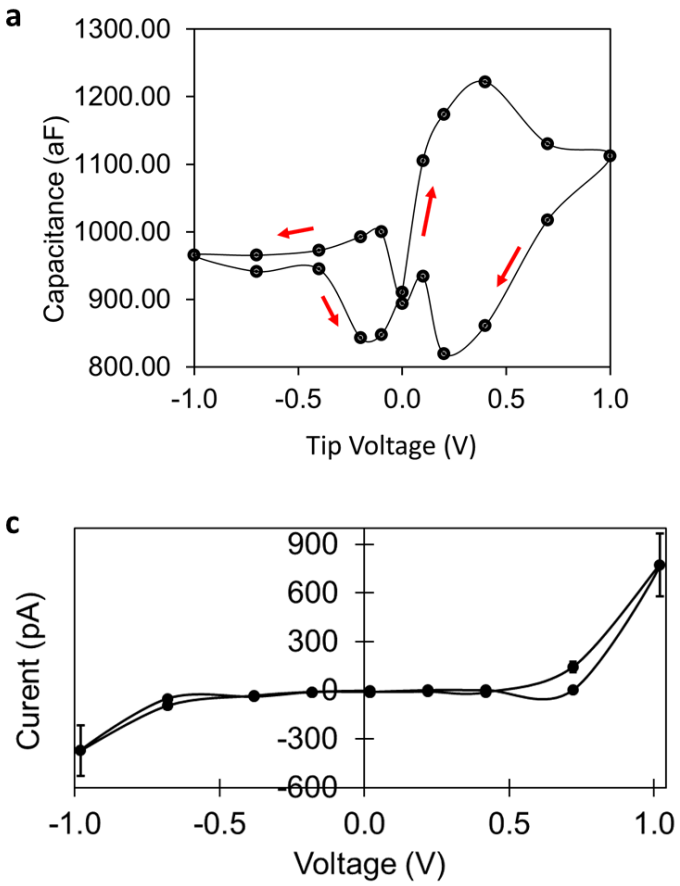

Figure 4.9. ***(a)*** *Capacitance and* ***(b)*** *current vs voltage in another MAPI-$PbAc_2$ perovskite surface.*

4.5 Conclusions

In this chapter, we first showed how to extract topographical artefacts from the SMM measurements by using a linear regression. The local S_{11} contrast has been also studied and compared to the work function contrast. While we found similarities in both SMM and KPFM contrasts we would need a deeper analysis to conclude they are arising from the same phenomena. The interferometric calibration has been tested and compared to the EFM calibration, providing a similar behaviour but with the values shifted. This is something that could be further investigated by making 3D models of the wave propagation from the end of the probe to the sample. Still, using the interferometric calibration for qualitative comparison, C-V curves have been made, showing a higher hysteresis on MAPI-PbI_2 samples compared to MAPI-$PbAc_2$ samples. After comparing them to I-V curves in the same range of voltages, an unusual behaviour at positive

voltages in MAPI-PbI_2 has been detected, thus, leading us to think that ion motion, from species such as I_i, is causing the high hysteresis effects.

As a summary it has been shown that SMM is a promising tool for capacitance characterization at the nanoscale. The results show: (1) contrasted capacitance images with several domains associated to a capacitance variation, and (2) the detection of a bigger MAPI-PbI_2 perovskite hysteresis compared to the MAPI-$PbAc_2$ perovskite.

References

1. Salado, M. *et al.* Impact of moisture on efficiency-determining electronic processes in perovskite solar cells. *J. Mater. Chem. A* **5**, 10917–10927 (2017).

2. Idígoras, J., Pellejà, L., Palomares, E. & Anta, J. A. The Redox Pair Chemical Environment Influence on the Recombination Loss in Dye-Sensitized Solar Cells. *J. Phys. Chem. C* **118**, 3878–3889 (2014).

3. Kharkovsky, S. & Zoughi, R. Microwave and millimeter wave nondestructive testing and evaluation - Overview and recent advances. *IEEE Instrumentation Measurement Magazine* **10**, 26–38 (2007).

4. Berweger, S. *et al.* Electronic and Morphological Inhomogeneities in Pristine and Deteriorated Perovskite Photovoltaic Films. *Nano Lett.* **17**, 1796–1801 (2017).

5. Plassard, C. *et al.* Detection of defects buried in metallic samples by scanning microwave microscopy. *Phys. Rev. B* **83**, 121409 (2011).

6. Gramse, G. *et al.* Calibrated complex impedance and permittivity measurements with scanning microwave microscopy. *Nanotechnology* **25**, 145703 (2014).

7. Huber, H. P. *et al.* Calibrated nanoscale capacitance measurements using a scanning microwave microscope. *Rev Sci Instrum* **81**, 113701 (2010).

8. Wu, S. & Yu, J.-J. Attofarad capacitance measurement corresponding to single-molecular level structural variations of self-assembled monolayers using scanning microwave microscopy. *Appl. Phys. Lett.* **97**, 202902 (2010).

9. Bowring, A. R., Bertoluzzi, L., O'Regan, B. C. & McGehee, M. D. Reverse Bias Behavior of Halide Perovskite Solar Cells. *Advanced Energy Materials* **8**, 1702365 (2018).

10. Meggiolaro, D. *et al.* Iodine chemistry determines the defect tolerance of lead-halide perovskites. *Energy Environ. Sci.* **11**, 702–713 (2018).

11. Du, M.-H. Density Functional Calculations of Native Defects in CH3NH3PbI3: Effects of Spin–Orbit Coupling and Self-Interaction Error. *J. Phys. Chem. Lett.* **6**, 1461–1466 (2015).

12. Yang, D., Ming, W., Shi, H., Zhang, L. & Du, M.-H. Fast Diffusion of Native Defects and Impurities in Perovskite Solar Cell Material CH3NH3PbI3. *Chem. Mater.* **28**, 4349–4357 (2016).

13. Eames, C. *et al.* Ionic transport in hybrid lead iodide perovskite solar cells. *Nature Communications* **6**, 7497 (2015).

14. Bryant, D. *et al.* Observable Hysteresis at Low Temperature in "Hysteresis Free" Organic–Inorganic Lead Halide Perovskite Solar Cells. *J. Phys. Chem. Lett.* **6**, 3190–3194 (2015).

15. Yang, T.-Y., Gregori, G., Pellet, N., Grätzel, M. & Maier, J. The Significance of Ion Conduction in a Hybrid Organic-Inorganic Lead-Iodide-Based Perovskite Photosensitizer. *Angew. Chem. Int. Ed. Engl.* **54**, 7905–7910 (2015).

Chapter 5

Early Stage Water Stability of $CH_3NH_3PbI_3$ Perovskites

The following publication was adapted from this chapter:

J. Llacer, D. Moerman, O. Douhéret, X Noirfalise, C. Quarti, R. Lazzaroni, D. Théron and P. Leclère, ACS Applied Nano Materials, 2020, 3, 8268-8277.

Stability is one of the most studied properties in perovskite materials. In this Chapter, stability against moisture degradation is studied at the nanoscale. The different regions found in Chapter 3 are also analyzed in this Chapter upon small amounts of water exposure. By controlling the amount of water at which the samples are exposed, a higher stability was found for perovskites prepared with lead iodide in the precursor solution. The results confirm the presence of different surface defects, as previously suggested in Chapter 3.

5.1 Introduction

As previously described in **Chapter 1**, perovskite solar cells are well known for their impressive optoelectronic properties. Their ease of fabrication also makes them to be in an economical advantage over other technologies such as silicon-based solar cells. Their latest improvements have brought them to the same performance level as other technologies such as thin-film photovoltaics.[1–4] However, the main reason holding them back to be competitive in the solar cell market is their lack of long term stability.[5] In **section 1.3.5** the stability in perovskite was widely described, in fact, stability is usually addressed macroscopically either for the whole solar cell device or for the perovskite layer itself.[6] Measurements such as photoluminescence, current-voltage (I-V) curves, quantum efficiency and many other related macroscopic measurements have been proven to be useful for the understanding of the device behavior under different conditions. Nevertheless, there still lacks a link between the observed macroscopic stability and the stability at the local scale. Lately, some groups are trying to push their perovskite research into that direction. For instance, Garret *et al.* used KPFM under illumination and found a reversible ion migration taking place at the $MAPbI_3$ perovskite surface, making the V_{oc} to vary upon illumination.[7] Such properties at the nanoscale may have affect the overall device performance and/or stability. Nonetheless, most of the perovskite stability studies are typically performed in ambient condition or in a humid environment. In this chapter we track the local stability with KPFM and, at the same time, we introduce a more precise method allowing for a controlled low water exposure level. For this study, $MAPbI_3$ was prepared by the two different synthesis routes previously described in **section 2.1** and characterized in **Chapter 3**. The SPM measurements, carried out for both sets of samples, exhibit different surface electronic properties and stability upon exposure to water. Complementary X-ray photoelectron spectroscopy (XPS) and X-ray diffraction (XRD) analysis correlate the observations with the variations in the chemical composition and the crystalline orientation planes, respectively, for the two types of $MAPbI_3$ perovskite. Consistent pictures can be drawn between chemical structure and composition, surface states and electronic properties and water stability for each of the two differently synthesized perovskites.

5.2 Sample Preparation for Tests

MAPI-$PbAc_2$ and MAPI-PbI_2 perovskite films, previously described in **Chapter 3,** were exposed to water vapor in this chapter. First, the perovskite films were introduced in a low-vacuum chamber (~ 1.15 torr) with 0.88 dm^3 of volume. Water vapor was then injected by cycles into the chamber, heated at ~ 55 ºC, and purged by a continuous nitrogen flow to hinder any condensation. Each cycle corresponds to a pulse of water and then flushing it away before the next one. This method allows a very precise control of the water quantity to which the sample is exposed. For comparison, Li *et al.* reported a threshold of $2 \cdot 10^{10}$ L (1 L corresponds to 10^{-6} torr.s) for $MAPbI_3$ to decompose, based on XPS measurements.[8] In this work, samples were exposed to much lower amounts of water, *i.e.*, from $2.25 \cdot 10^8$ L up to $5 \cdot 10^9$ L, which allows to follow earlier stages of the degradation process.

The purpose of this work was to study the evolution of the work function and current of a given location in the perovskite surface after water exposure. However, such study implies that the sample has to be moved from the AFM stage to the vacuum chamber for water exposure. Then, the sample needs to be placed again in the AFM stage for the measurement of the work function (by KPFM) and current (by C-AFM). Measurements with KPFM and C-AFM require different AFM probes, what implies that the AFM probe holder would necessarily be moved. Therefore, a method to identify the same micrometric spot was needed. The approach we followed is presented as follows:

First, the sample is marked with a cross using a tweezer, which makes it easy to spot with the AFM camera. Still, the cross is quite big compared to the probe size, so we need to make some smaller marks. Next, the topography is scanned near the cross mark in contact mode, taking care of not scratching the sample. Once a suitable location is found, the probe is lifted by decreasing the setpoint voltage so that the AFM feels like if it was in contact. Actually, this makes the AFM to scan while lifted. At this moment, we make the AFM to scan in just 1 horizontal line (we tend to use 512 lines for a whole image) repeatedly. Then we engage again but this time the setpoint voltage is set to be very high so that the sample surface is significantly scratched by the probe. After some time, the probe is lifted and the same process is made for a parallel line with around 7 μm of separation. This results in two parallel lines (and a destroyed probe) easily noticeable with the AFM camera, as in **Fig. 5.1**. Next, it is just a matter of looking for the small lines with

the AFM camera and, once engaged, to place the probe in the area between the lines by detecting the borders of it when tracking the topography.

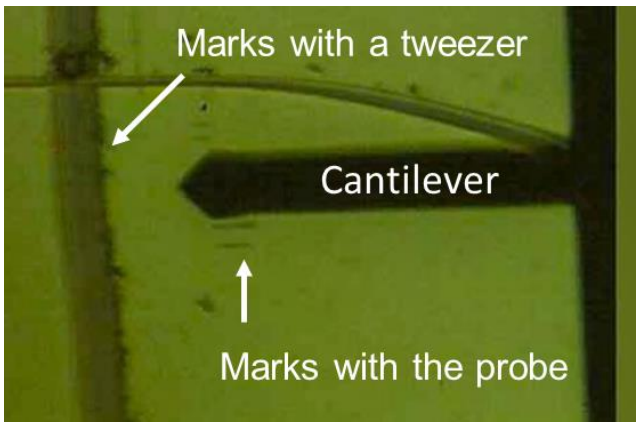

Figure 5.1. Marks done with an AFM probe for spot tracking.

5.3 Impact of Small Amounts of Water on the $CH_3NH_3PbI_3$ Perovskite Surface

Therefore, the WF was measured taking care of always probing the same location (**Fig. 5.2a, b)**. Upon exposure to water, the WF of the MAPI-$PbAc_2$ surface tends to decrease for the two types of domains, HWF and LWF (further described in **Chapter 3**), towards a common value, as shown in **Fig. 5.2c**. After $9 \cdot 10^8$ L (40 cycles) of water exposure, HWF and LWF domains can no longer be distinguished and, upon further water exposure, the WF tends to stabilize at ~ 4.6 eV. Note that at such low exposure, the topographic profile remains unchanged (**Fig. 5.2a**)**.** The final WF value corresponds to the Fermi level being in the vicinity of mid-gap. For a non-perfect crystal, such intrinsic behavior (having the Fermi level at mid-gap) can only be attributed to semi-insulating properties, where the energy bands are depopulated from their carriers by deep traps, inducing a weak conduction. This makes the perovskite to behave as an insulator.

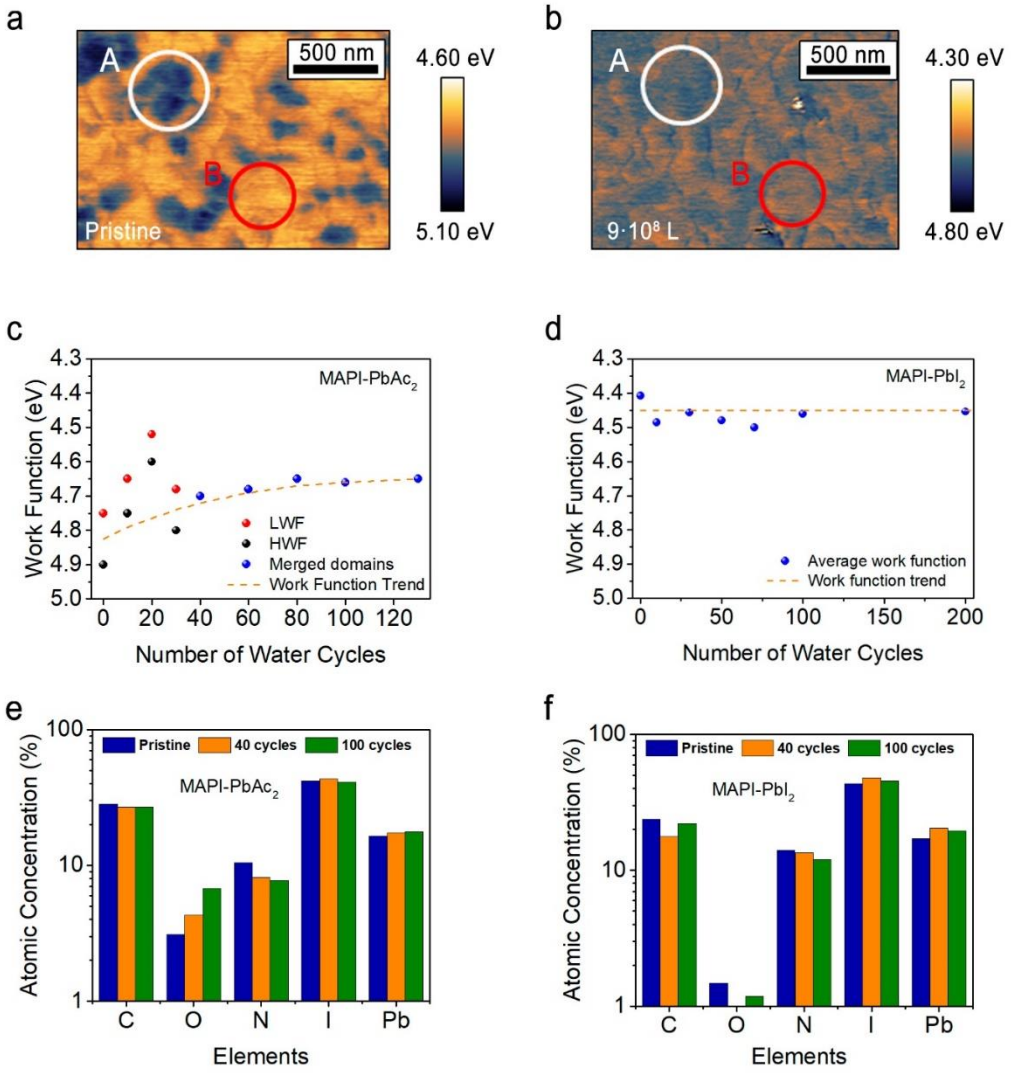

Figure 5.2. *Work function images of the MAPI-PbAc2 (**a**) pristine film and (**b**) after exposure to 100 cycles of water vapor. Graph (**c**) shows the WF evolution of MAPI-PbAc2 while graph (**d**) shows the WF evolution for MAPI-PbI2 upon water exposure. Graph (**e**) and (**f**) represent the atomic concentrations measured by XPS for MAPI-PbAc2 and MAPI-PbI2, respectively. Merged domains (blue dots in (c) and (d)) stand for the situations where domains can no longer be distinguished so only the average WF value of the sample is considered.*

The fact that the WF values are moving towards mid-gap upon water exposure for both domains, means that both HWF and LWF domains interact most probably in a similar way upon water exposure. This behavior excludes the hypothesis we made in **Chapter 3** about the possibility to have different surface terminations, making the MAPI-PbAc2 to be heterogeneous in terms of work function. Koocher *et al.* and Mosconi *et al.* found that

PbI-terminated surfaces should be more resistant to water interactions compared to MAI-terminated surfaces, which would result in a delayed WF shift toward mid-gap values.[9,10] In fact, Quarti et al. went further and measured a difference of ~ 1 eV between the energy levels of PbI and MAI-terminated surfaces.[11] Instead, in a perovskite system with defects, the position of the Fermi level at mid-gap rather relates to the formation of deep traps. Consistently, no C-AFM current could be detected after more than 10 cycles of water exposure (corresponding to $2.25 \cdot 10^8$ L). Therefore, there is a distribution of surface states on the MAPI-$PbAc_2$ surface that induces the difference in the carrier injection/extraction previously shown in **Chapter 3**, **Figure 3.4**. Such a heterogeneous surface can potentially lower not only the performance of the device but also its stability. These observations are comparable to the previously reported study by Ralaiarisoa *et al.* where a perovskite film was exposed to ~ $2 \cdot 10^4$ L, showing a reversible water adsorption.[12] Higher exposures, ~ $1 \cdot 10^{10}$ L, resulted in a WF decrease of 0.33 eV attributed to an increase of Pb^0-related surface states. The present work studies the water interaction in the upper exposure range of the previous study.

These results indicate that for the MAPI-$PbAc_2$ films, very small exposure to water is enough to strongly affect the electronic properties by creating deep trap states, hence to suppress charge transport. In this scenario, in a pristine p-type perovskite, the presence of surface states makes the surface to be less p-type, as previously shown in **Fig. 3.4**, the possible point defects to be considered are donor sites lying above the Fermi level. These defects can be induced by I vacancies (V_I), substitution of Pb and MA cations at I sites (Pb_I and MA_I, respectively), substitution of Pb ions at MA sites (Pb_{MA}) and MA and Pb interstitials (MA_i and Pb_i, respectively).[13] Among these defects, we consider MA_i, and V_I to potentially dominate due to their lower formation energies.[14,15]

We also investigated the effect of water exposure on the perovskite prepared from the PbI_2 precursor (MAPI-PbI_2). When exposing the MAPI-PbI_2 surface to pulsed water vapor cycles, the WF remains unchanged up to 200 cycles (**Fig. 5.2d)**. The C-AFM current also remain constant up to 200 cycles (see **Fig. 5.3)**. This is in strong contrast with the MAPI-$PbAc_2$ material, for which no current could be measured after the first 10 water vapor cycles (corresponding to $2.25 \cdot 10^8$ L). Interestingly, Leguy *et al.* also investigated the initial steps of $MAPbI_3$ degradation by exposing the films to 35% relative humidity at 21 ºC and found that $MAPbI_3$ forms hydrated intermediates ($MAPbI_3 \cdot H_2O$), which can

be dehydrated back to $MAPbI_3$.[16] For comparison, in our tests we exposed the samples to much lower amounts of water and, in addition, the vacuum chamber was heated at ~ 55 ºC, which would dehydrate the intermediate back to $MAPbI_3$. After prolonged exposure to water vapor, the perovskite can transform into a dihydrated compound ($(MA)_4PbI_6 \cdot 2H_2O$) that cannot be dehydrated back.[16] Here, MAPI-$PbAc_2$ and MAPI-PbI_2 perovskites cannot be measured anymore by SPM techniques after 120 and 200 cycles respectively. The dihydrated perovskite compound may be creating electrostatic interactions through the coordinated H_2O and the AFM probe.

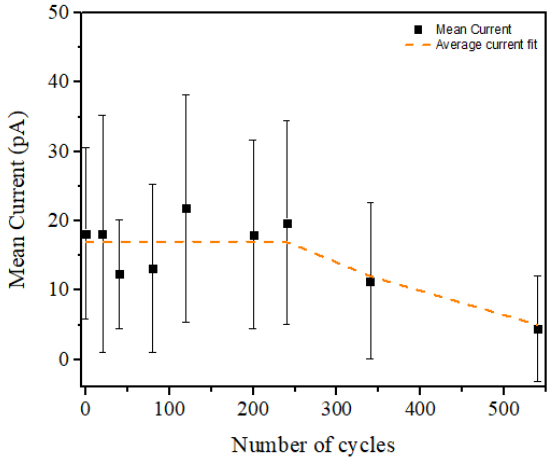

Figure 5.3. *Current response average measured in C-AFM at 1.3V for MAPI-PbI_2 upon exposure to water cycles. The decrease of the current beyond 200 cycles is thought to be due to formation of a layer of condensed water on the surface which results in $MAPbI_3$ perovskite segregation.*

The work function of MAPI-PbI_2 is located closer to the mid-gap than to the conduction band, the trap states observed in MAPI-PbI_2 surface are then expected to be acceptor ones inducing deep states. These surface acceptor defects seem to be less reactive upon water exposure, therefore we assume n-type surfaces such as MAPI-PbI_2 are more stable at the early-stage of water-induced degradation.

5.4 Tracking the Structural Evolution at the Early Stage of Water Degradation

Both pristine $MAPbI_3$ materials were also characterized by XPS, and similar measurements were carried out after exposure to 40 and 100 water vapor cycles,

corresponding to 9 x 10^8 L and 2.2 x 10^9 L. However, when transferring the samples from the glovebox to the XPS, it is inevitable to expose the samples to ambient conditions for a short period of time. The relative humidity of the atmospheric air in our lab is around 50%. The saturated vapor pressure of water at 21 ºC is 18.650 torr.[17] If we take into account that the time needed to transfer the samples from the glovebox to the XPS chamber is around 1 minute:

$$\frac{0.50 \cdot 1\ min\ \cdot 60\ s\ \cdot\ 18.650\ torr}{10^{-6}\ torr \cdot s} = 5.6 \cdot 10^8\ L$$

Although this is a considerable amount of water, it is still below the amounts of water vapor injected in the vacuum chamber during 40 and 100 water vapor cycles. When looking at the amount of oxygen present in both $MAPbI_3$ films (**Fig. 5.2e** and **f**), it seems that the amount of water is greatly affected by the water vapor injected in the vacuum chamber rather than by the ambient exposure. Therefore, we considered that this fast exposure to ambient conditions has little effect for these measurements.

Fig. 5.2e shows the variations of the atomic concentration of the elements forming the MAPI-$PbAc_2$ films. Upon exposure to water, a significant increase of the oxygen content at the surface can be observed and, simultaneously, a decrease in nitrogen concentration. In contrast, the nitrogen concentration barely changes in MAPI-PbI_2 upon water exposure while no significant amount of oxygen is observed (**Fig. 5.2f)**. It is tempting to relate these behaviors to the WF shift towards the mid-gap observed in water-exposed MAPI-$PbAc_2$ films (**Fig. 5.2c**) and the constant WF value for MAPI-PbI_2 films (**Fig. 5.2d**). The Pb:I elemental ratio for both materials (1:3) remains constant even after exposure to 100 cycles of water vapor, indicating that a possible degradation cannot be attributed here to perovskite segregation at the surface and thus a change in stoichiometry. Interestingly, the traps expected to be present in the MAPI-$PbAc_2$ surface, V_I and MA_i, are typically positively charged, which would imply that they are keen to interact with the electronegative oxygen atoms from water molecules. As for MAPI-PbI_2, the considered defects, V_{Pb} and I_i are negatively charged, which would make them more difficult for the oxygen to interact.

The water-perovskite interaction is further confirmed by the XRD measurements carried out after similar amounts of exposure to water vapor shown in **Fig. 5.4a** for MAPI-$PbAc_2$ and **Fig. 5.5** for MAPI-PbI_2. The main XRD peaks in MAPI-$PbAc_2$ are located at 14.04º

and 28.31º, corresponding to the X-ray scattering from the (110) and (220) planes, **Fig. 5.4a**.[18] After exposing the MAPI-$PbAc_2$ sample to 100 cycles of water, there is a reduction in the X-ray scattering intensities while the characteristic PbI_2 signal is not present, indicating that the perovskite did not start structural degradation yet. On the other hand, in the MAPI-PbI_2 film, apart from the most intense peaks at 14.07º and 28.40º, there is another intense peak at 31.82º attributed to the (222) plane, **Fig. 5.4c**. The low-intensity feature at 12.65º in the XRD diffractogram for MAPI-PbI_2 indicates the presence of unreacted PbI_2.[19] The reduction in intensity of the XRD features seen for MAPI-$PbAc_2$ could be related to the change in morphology observed with AFM, (**Fig. 5.6b)**. **Fig. 5.6c** shows the variations of the topographical roughness of the MAPI-$PbAc_2$ layer upon exposure to water vapor, as described by the power density spectrum of the AFM images. The gradual increase of the spectral density at high wavenumbers (*i.e.*, smaller spatial distances) for MAPI-$PbAc_2$ indicates that the relative roughness increases when increasing the water exposure, probably due to an increase of small grains. This is illustrated by the image of **Fig. 5.6b**, which shows the surface morphology after 150 cycles of water exposure (which corresponds to amounts of water similar to what reported by literature). The large grains initially present have broken up into smaller features, which is expected to strongly impact the electronic properties, as amply reported in literature.[8] It is also important to notice that the spectral density of the MAPI-PbI_2 material is much less sensitive to water exposure (**Fig. 5.6d**), consistent with the better preservation of the electronic properties.

The highest XRD intensity peak in both $MAPbI_3$ films is the (110) peak and it is used to measure the *a* lattice constant, which corresponds to the short lattice distance in a tetragonal geometry. The long lattice distance, the c lattice, is calculated mainly from the (222) peak. As a result, **Fig. 5.4b** and **5.4d** show the evolution of the *a* and *c* lattice distances upon water exposure in MAPI-$PbAc_2$ and MAPI-$PbAc_2$ respectively. For MAPI-$PbAc_2$, only the *a* lattice parameter is increased when exposing the sample to water. This lattice expansion could be related to a reaction between the MA^+ cation and water molecules, which has been proposed by Li *et al.*. They propose that water molecules act as n-dopants and move the perovskite Fermi level closer to the conduction band. This is discussed below on the basis of the XPS results and is consistent with the positively-charged defects reacting with water.[8] In contrast, in MAPI-PbI_2 both lattice distances remain constant up to 200 cycles of water exposure (**Fig. 5.4d)**.

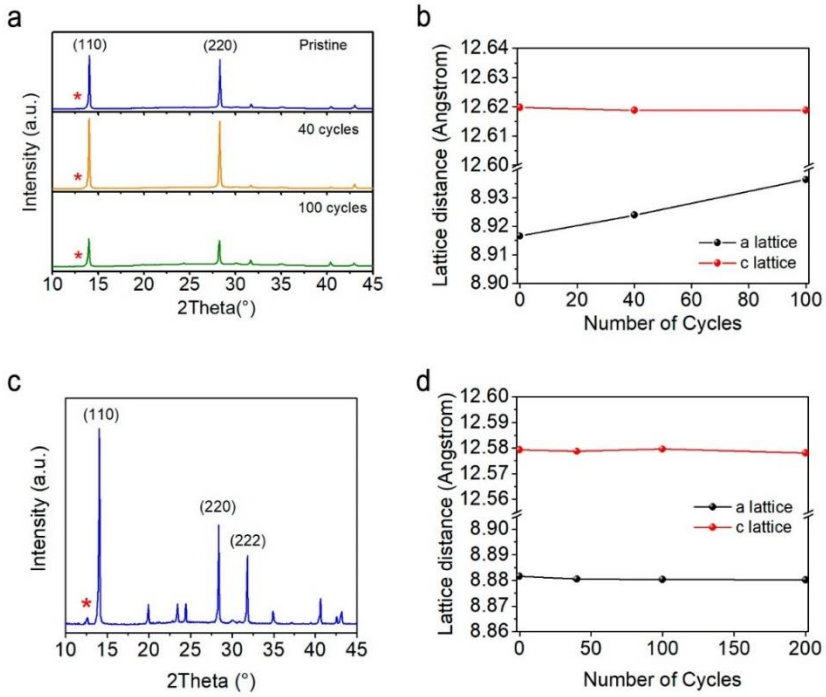

Figure 5.4. *(**a**) XRD diffractograms of the MAPI-$PbAc_2$ pristine and water-exposed (**b**) MAPI-$PbAc_2$ lattice distance displacement upon water vapor exposure, (**c**) XRD diffractogram of the MAPI-PbI_2 pristine sample and (**d**) MAPI-PbI_2 lattice distance displacement upon water vapor exposure. Lattice a (c) stands for the shorter (longer) axis in the tetragonal structure.*

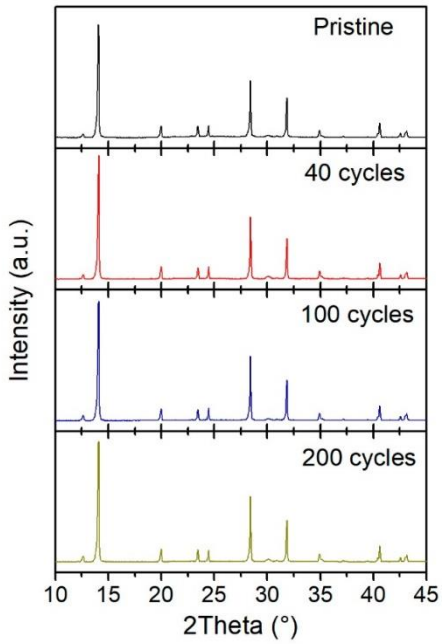

Figure 5.5. *XRD diffractograms of the MAPI-PbI_2 pristine and water-exposed samples.*

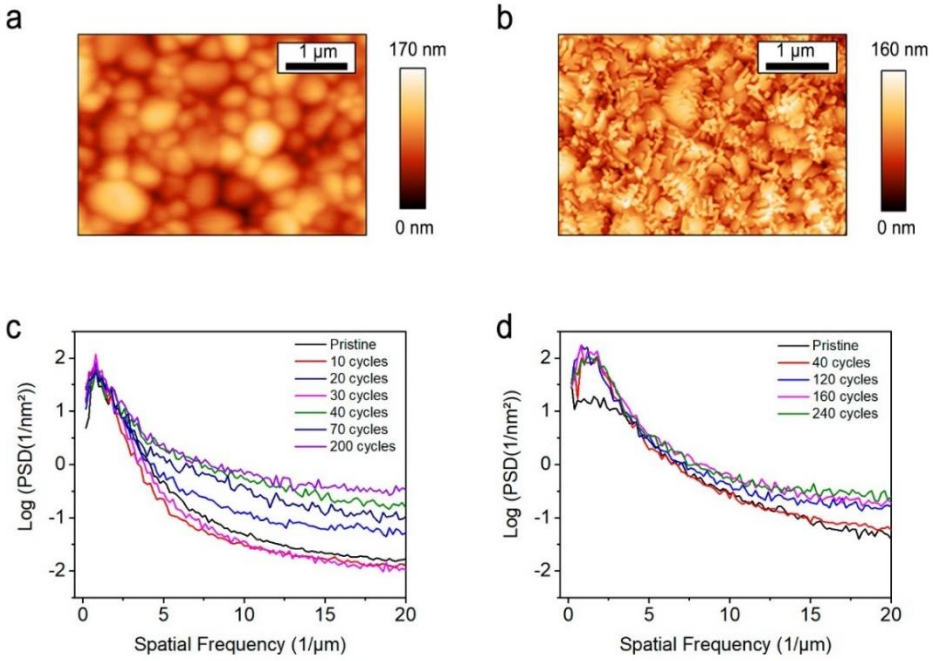

Figure 5.6. *AFM height images of a MAPI-$PbAc_2$ film upon exposure to* ***(a)*** *40 and* ***(b)*** *150 cycles of water. Power spectrum density plot of* ***(c)*** *MAPI-$PbAc_2$ and* ***(d)*** *MAPI-PbI_2 films.*

To elucidate the specific interactions of water with MAPI-$PbAc_2$ and MAPI-PbI_2, we recorded high-resolution XPS core-level spectra. The C 1s core level spectrum of MAPI-$PbAc_2$ shows two clear peaks at 285.1 eV and 286.8 eV, for C-C and C-N groups respectively, **Fig. 5.7a**.[20] Even though the peak at 285 eV has been typically attributed to C-C bonding and it is used for XPS calibration, it is most probably a bond created from small amount of hydrocarbon contamination.[21,22] However, this peak has been also assigned to CH_3I, created when MAI vapor is in contact with PbI_2.[23,24] After 40 and 100 cycles of water, the C 1s photoemission peaks and the relative carbon concentration remain unchanged, as observed in **Fig. 5.7c**, **6e**, and **4e**. Since the nitrogen content was shown to decrease after water exposure along with the increase of the oxygen content, the peak at 286.8 eV for MAPI-$PbAc_2$ can be attributed to a combination of contributions from C-N groups and C-O groups. The evolution of the oxygen and nitrogen content is consistent with the occurrence of a nucleophilic substitution reaction by which the oxygen atom of a water molecule binds to the carbon atom of methylammonium, expelling one ammonia molecule that is pumped away. Although this reaction is kinetically not favorable, we think that it is enhanced by the vacuum chamber heat (~ 55ºC). This chemical reaction is expected to deeply affect the electronic properties of the materials. Note however that the increase in the oxygen content is much stronger than the decrease in the nitrogen content (**Fig. 5.2e**), which suggests that part of the water molecules simply adsorb on MAPI-$PbAc_2$ (and could further modify its electronic properties *via* electrostatic interactions).

The C 1s core level spectrum of the MAPI-PbI_2 shows two peaks at ~ 285 eV and ~ 287 eV, similar to the MAPI-$PbAc_2$ peaks. However, not only the C 1s peaks and the relative concentration of carbon remain unaffected, but also the concentration of oxygen and nitrogen remains unchanged upon water exposure, as shown in **Fig. 5.7b**, **d**, **f** and **Fig. 5.2f**. This observation confirms that MAPI-PbI_2 is less reactive with water.[25]

The Pb 4f emission shows two distinctive peaks at 138.7 and 143.3 eV for the Pb $4f_{7/2}$ or Pb_3O_4 and Pb $4f_{5/2}$ or PbO_2 respectively, for both $MAPbI_3$ perovskite films, **Fig. 5.8c** and **f**. However, there is a slight difference between both perovskite surfaces. While for MAPI-$PbAc_2$ only the peaks attributed to Pb 4f can be found, **Fig. 5.8c**, in MAPI-PbI_2 the peak for metallic Pb can be also found (~ 142 eV), **Fig. 5.8f**. The presence of metallic lead in the perovskite surface has been previously attributed to the photolysis of the

unreacted PbX_2 materials (X being an halide) induced by the X-rays.[26] In particular, in this work, we identified unreacted PbI_2, see the peak with an asterisk symbol in **Fig. 5.4c**. Therefore, it is not surprising to find metallic Pb as previously reported.[27] Comparing again our results with the work from Ralaiarisoa *et al.*, they detected a reduction of the metallic Pb content, suggesting that this reduction introduces gap states that pin the Fermi level, however, in this study the lead content remained constant even after exposing the samples to water vapor.[12]

The constant behavior was also measured for the I 3d content, with emission peaks at 619.7 and 631.0 eV for I $3d_{5/2}$ and I $3d_{7/2}$, respectively, **Fig. 5.8a** and **d**. Finally, the binding energy of the N 1s main peak (at 402.8 eV) remains unaltered as well, **Fig. 5.8b** and **e**.

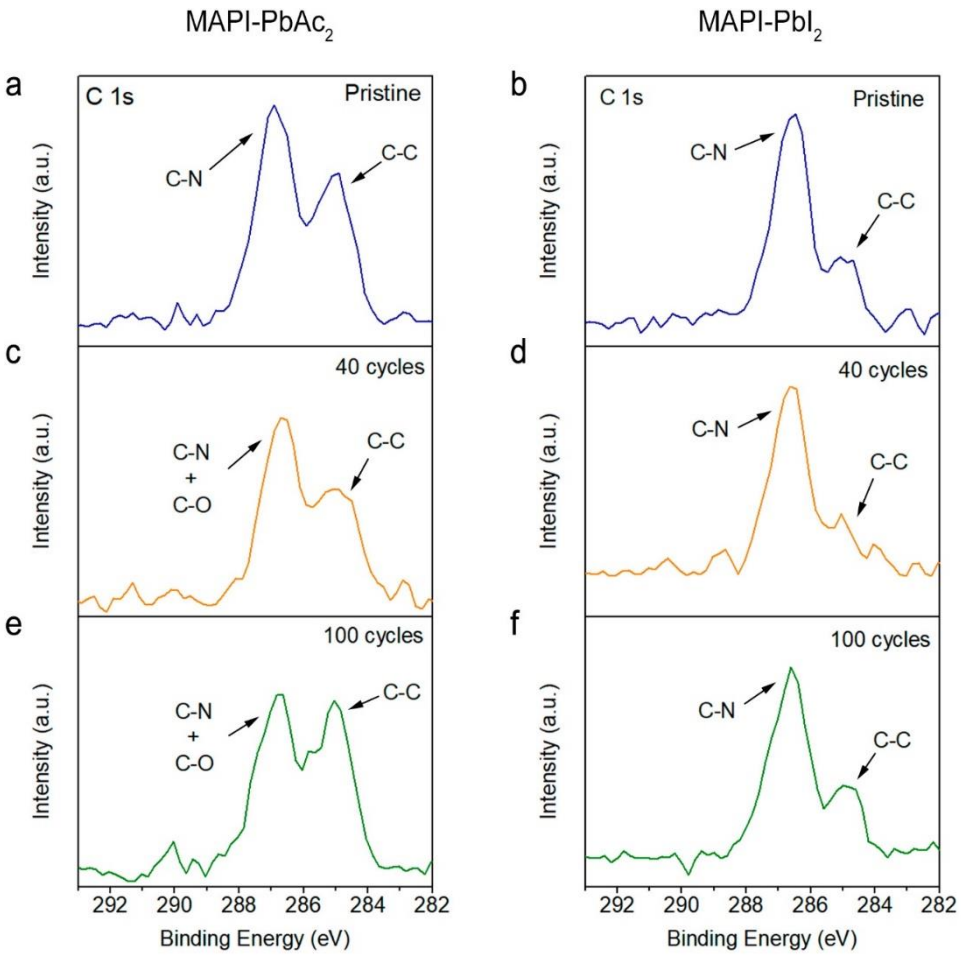

Figure 5.7. *C1s core level XPS spectra of MAPI-$PbAc_2$ (a,c,e) and MAPI-PbI_2 (b,d,f): pristine (**a**, **b**), exposed to 40 cycles (**c**, **d**) and to 100 cycles of water (**e**, **f**).*

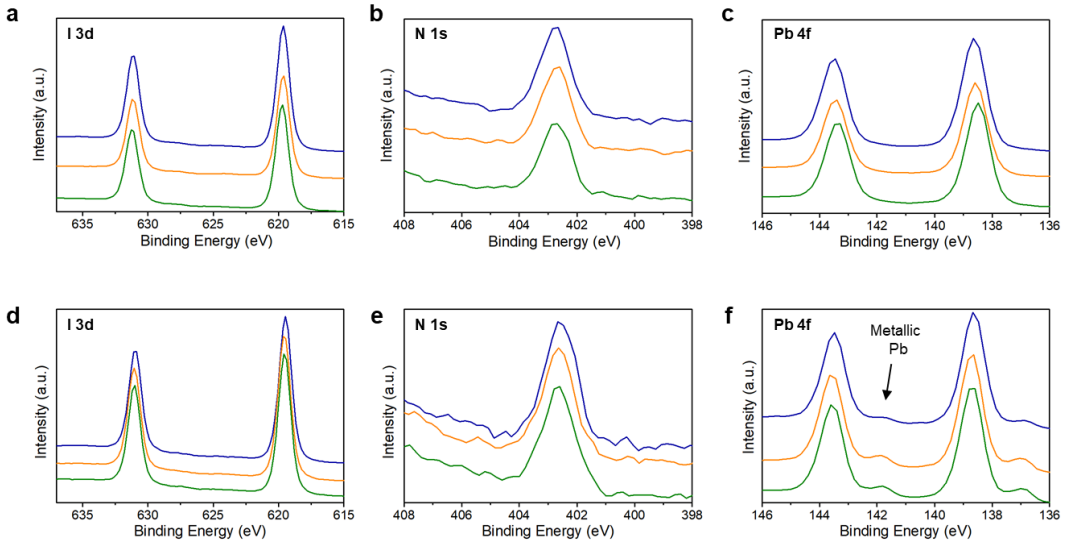

Figure 5.8. *XPS core level spectra of* ***(a)*** *(**d**) I 3d,* ***(b)*** *(**e**) N 1s and* ***(c)*** *(**f**) Pb 4f for pristine and water-exposed MAPI-PbAc₂ samples.* ***(a-c)*** *Correspond to MAPI-PbAc₂ and* ***(d-f)*** *to MAPI-PbI₂. Blue curves represent the pristine film, orange represents the film exposed to 40 cycles and green represents an exposure to 100 water cycles.*

5.5 Conclusions

In this chapter, a relationship between electronic structures at the $MAPbI_3$ surface and local stability upon low water exposure has been proposed. In MAPI-$PbAc_2$, the WF decreases after water exposure. This effect was shown to correspond to a drift of the Fermi energy towards mid-gap, indicating the creation of deeper trap states turning the perovskite into a semi-insulator, consistently with the collapse of the current signal. The XPS measurements indicate that the methylammonium groups are likely to react with water molecules releasing NH_3 and creating C-O bonds. Also, a higher stability against moisture was observed for MAPI-PbI_2. This improved stability was attributed to the different nature of defects, acceptors compared to donors in MAPI-PbI_2 and MAPI-$PbAc_2$ respectively. By using a vacuum chamber, we had a precise control on the exposure to very small amounts of water, which allowed us to study the early degradation mechanisms in perovskites. We observed that strong interaction with water molecules can occur very quickly in p-type perovskites like MAPI-$PbAc_2$. This rapid interaction with water alters the electronic and transport properties even prior to any morphological or stoichiometric changes.

References

1. Green, M. A., Ho-Baillie, A. & Snaith, H. J. The emergence of perovskite solar cells. *Nature Photonics* **8**, 506–514 (2014).

2. Brenner, T. M., Egger, D. A., Kronik, L., Hodes, G. & Cahen, D. Hybrid organic—inorganic perovskites: low-cost semiconductors with intriguing charge-transport properties. *Nature Reviews Materials* **1**, 1–16 (2016).

3. Gao, P., Grätzel, M. & Nazeeruddin, M. K. Organohalide lead perovskites for photovoltaic applications. *Energy Environ. Sci.* **7**, 2448–2463 (2014).

4. Sessolo, M. & Bolink, H. J. Solar cells. Perovskite solar cells join the major league. *Science* **350**, 917 (2015).

5. Reyna, Y. *et al.* Performance and stability of mixed FAPbI3(0.85)MAPbBr3(0.15) halide perovskite solar cells under outdoor conditions and the effect of low light irradiation. *Nano Energy* **30**, 570–579 (2016).

6. Wang, R. *et al.* A Review of Perovskites Solar Cell Stability. *Advanced Functional Materials* **29**, 1808843 (2019).

7. Garrett, J. L. *et al.* Real-Time Nanoscale Open-Circuit Voltage Dynamics of Perovskite Solar Cells. *Nano Lett.* **17**, 2554–2560 (2017).

8. Li, Y. *et al.* Degradation by Exposure of Coevaporated CH3NH3PbI3 Thin Films. *J. Phys. Chem. C* **119**, 23996–24002 (2015).

9. Koocher, N. Z., Saldana-Greco, D., Wang, F., Liu, S. & Rappe, A. M. Polarization Dependence of Water Adsorption to CH3NH3PbI3 (001) Surfaces. *J. Phys. Chem. Lett.* **6**, 4371–4378 (2015).

10. Mosconi, E., Azpiroz, J. M. & De Angelis, F. Ab Initio Molecular Dynamics Simulations of Methylammonium Lead Iodide Perovskite Degradation by Water. *Chem. Mater.* **27**, 4885–4892 (2015).

11. Quarti, C., De Angelis, F. & Beljonne, D. Influence of Surface Termination on the Energy Level Alignment at the CH3NH3PbI3 Perovskite/C60 Interface. *Chem. Mater.* **29**, 958–968 (2017).

12. Ralaiarisoa, M., Salzmann, I., Zu, F.-S. & Koch, N. Effect of Water, Oxygen, and Air Exposure on CH3NH3PbI3–xClx Perovskite Surface Electronic Properties. *Advanced Electronic Materials* **4**, 1800307 (2018).

13. Yin, W.-J., Shi, T. & Yan, Y. Unusual defect physics in CH3NH3PbI3 perovskite solar cell absorber. *Appl. Phys. Lett.* **104**, 063903 (2014).

14. Yin, W.-J., Shi, T. & Yan, Y. Unique properties of halide perovskites as possible origins of the superior solar cell performance. *Adv. Mater. Weinheim* **26**, 4653–4658 (2014).

15. Wei, S.-H. Overcoming the doping bottleneck in semiconductors. *Computational Materials Science* **30**, 337–348 (2004).

16. Leguy, A. M. A. *et al.* Reversible Hydration of CH3NH3PbI3 in Films, Single Crystals, and Solar Cells. *Chem. Mater.* **27**, 3397–3407 (2015).

17. Grünewald, H. Handbook of Chemistry and Physics. Von R. C. Weast. The Chemical Rubber Co., Cleveland, Ohio/USA 1972. 52. Aufl., XXVII, 2313 S., geb. DM 99.80. *Angewandte Chemie* **84**, 445–446 (1972).

18. Lee, M. M., Teuscher, J., Miyasaka, T., Murakami, T. N. & Snaith, H. J. Efficient hybrid solar cells based on meso-superstructured organometal halide perovskites. *Science* **338**, 643–647 (2012).

19. Docampo, P. *et al.* Influence of the orientation of methylammonium lead iodide perovskite crystals on solar cell performance. *APL Materials* **2**, 081508 (2014).

20. Beamson, G. High Resolution XPS of Organic Polymers. *The Scienta ESCA 300 Database* (1992).

21. Ng, T.-W., Chan, C.-Y., Lo, M.-F., Guan, Z. Q. & Lee, C.-S. Formation chemistry of perovskites with mixed iodide/chloride content and the implications on charge transport properties. *J. Mater. Chem. A* **3**, 9081–9085 (2015).

22. Abdelhady, A. L. *et al.* Heterovalent Dopant Incorporation for Bandgap and Type Engineering of Perovskite Crystals. *J. Phys. Chem. Lett.* **7**, 295–301 (2016).

23. Liu, L., McLeod, J. A., Wang, R., Shen, P. & Duhm, S. Tracking the formation of methylammonium lead triiodide perovskite. *Appl. Phys. Lett.* **107**, 061904 (2015).

24. Ke, J. C.-R. *et al.* In situ investigation of degradation at organometal halide perovskite surfaces by X-ray photoelectron spectroscopy at realistic water vapour pressure. *Chem. Commun.* **53**, 5231–5234 (2017).

25. Hoehn, R. D., Francisco, J. S., Kais, S. & Kachmar, A. Role of Water on the Rotational Dynamics of the Organic Methylammonium Cation: A First Principles Analysis. *Sci Rep* **9**, 1–9 (2019).

26. Plekhanov, V. G. Lead halides: electronic properties and applications. *Progress in Materials Science* **49**, 787–886 (2004).

27. McGettrick, J. D. *et al.* Sources of Pb(0) artefacts during XPS analysis of lead halide perovskites. *Materials Letters* **251**, 98–101 (2019).

Chapter 6

Conclusions and Outlook

6.1 Conclusions

In this thesis, the main objective is to track the surface properties of perovskites at the nanoscale by a characterization process including scanning probe microscopies and surface analysis. These surface properties play an important role for obtaining efficient and stable perovskite solar cells. However, since the properties of the surface are significantly related to the synthesis route and the environment conditions, it is important to fine-tune each synthesis step. Therefore, in this work, we combined several characterization techniques in order to give some insights about the resulting surface properties with respect to two different synthesis routes. This chapter summarizes the main conclusions of this work, and then provides some suggestions for future research towards perovskite solar cells with a better understanding of the surface properties.

First, the $CH_3NH_3PbI_3$ perovskite was studied at the nanoscale using AFM techniques such as KPFM and C-AFM. The analysis focused on two different synthesis routes for $CH_3NH_3PbI_3$ so-called MAPI-$PbAc_2$ and MAPI-PbI_2. These synthesis routes lead not only to a different perovskite bulk character but also to different surface properties. The MAPI-$PbAc_2$ perovskite route leads to a p-type perovskite while MAPI-PbI_2 results in an n-type perovskite. KPFM maps revealed an heterogeneous MAPI-$PbAc_2$ surface in terms of work function (WF). We approximated the WF map to be composed mainly of two domains. Among the possible origins of the WF contrast, we considered two: either surface terminations or surface point defects. However, the effective barriers measured for the two domains, together with their respective WF allowed us to determine a similar valence band (VB) for each domain. Given the fact that PbI- and MAI-terminated surfaces differ in their energy levels and also their bandgap by ~ 1 eV, we suggest point defects to be responsible for the WF difference. We also measured a lower WF at the surface compared to the bulk of the perovskite, meaning that among the possible point defects, donor sites are probably the ones responsible for the anisotropy. MAPI-PbI_2 perovskite was also analysed by KPFM and, putting aside the fact that there were unreacted PbI_2 species, no major WF contrast was observed over the surface. Here, with an average WF of 4.4 eV and an n-type perovskite, the possible traps to be considered are acceptor ones.

We further characterized the perovskite electronic surface properties using the SMM. After the removal of the topography crosstalk signal on the S_{11} signal, we were able to

detect a significant contrast in S_{11} over the surface. To study it further, the S_{11} was converted to capacitance variation by using a calibration method based on an interferometer. Capacitance variation also showed heterogeneous properties over the MAPI-$PbAc_2$ surface, similar to what was observed by KPFM and C-AFM in Chapter 3. Next, the average capacitance in both perovskite surfaces (MAPI-$PbAc_2$ and MAPI-PbI_2) was tested upon bias voltage. The result was a big hysteresis effect especially for MAPI-PbI_2 surfaces, probably due to a higher ion motion induced by the characteristic I_i surface defects that can be found in n-type perovskites such as MAPI-PbI_2.

Finally, with the main purpose to test the stability of these two perovskite films, they were exposed to water in a perfectly controlled system. The exposure of a very small amount of water on MAPI-$PbAc_2$ resulted in both domains (before mentioned) changing their WF towards lower values. The fact that both domains shift their WF in an even trend further excludes the hypothesis of surface terminations as the origin behind the WF difference as they are expected to interact differently to water. Another important observation is that no current could be detected anymore from the first water exposure, meaning that the perovskite turns into a semi-insulator. After repeatedly exposing the MAPI-$PbAc_2$ surface to increasing amounts of water, the WF value reached a plateau around mid-gap. This effect suggests that donor surface defects are interacting with water. XPS measurements confirmed the presence of oxygen on the MAPI-$PbAc_2$ surface. Same as for MAPI-$PbAc_2$, the MAPI-PbI2 surface was also exposed to water vapour. However, this time the electronically uniform MAPI-PbI2 surface kept its average WF for much higher exposures than MAPI-$PbAc_2$. This may be an indication of acceptor sites being less reactive than donor sites upon water interactions.

6.2 Outlook

As it is the case with research studies, ideas are developed in a given time, which is usually not enough to bring them fully to completion. Here there are some outlooks for future pathways of research that could also further improve the work done in this thesis.

So far, we have determined how synthesis routes, and more specifically, how the p and n semiconducting character can affect the stability of perovskite films. This study leaves room for a wider local stability study in which the much sought after device stability

along with the solar cell performance could be addressed. Ideally, this would be achieved with both, the techniques performed in this thesis and DFT calculations. First, an evaluation of the thermodynamic driving force or affinity, $\Delta G = \sum_i \nu_i \mu_i$, between the possible point defects in the perovskite surface and water may be carried out, where ν and μ are, respectively, the stoichiometric coefficients and chemical potentials for the species involved. Then, tracking the local WF shift such as presented in **Chapter 5** may indicate what kind of defect is present in the surface. Also, an evaluation of the current and work function properties upon light exposure (with C-AFM and KPFM respectively) may help to further understand the behaviour of these surfaces.

Once the exact type of point defect is determined, a passivation technique can be developed. Typically, experimental passivation techniques and determination of the exact defect present at the surface are developed separately. For instance, Yuan *et al.* introduced the perovskite into a $Pb(NO_3)_2$ solution, it allows to reduce the expected surface defects such as V_I and I_i with Pb^{2+} ions.[1]

Regarding the SMM measurements, there is still range to improve the calibration procedure presented in Chapter 4. Although the calibration method that does not require any additional calibration sample, a deeper analysis would be needed in order to find how to extract real capacitive values. Nonetheless, the heterogeneous contrast in capacitance is still valid and it would suggest that point defects are present, as it has been demonstrated by KPFM and C-AFM. A way to corroborate this assumption would be to correlate SMM with KPFM or C-AFM by either installing a camera with a higher resolution in the AFM system using the SMM or using the IEMN-made SMM, which is paired with an SEM.

References

1. Yuan, J., Zhang, L., Bi, C., Wang, M. & Tian, J. Surface Trap States Passivation for High-Performance Inorganic Perovskite Solar Cells. *Solar RRL* **2**, 1800188 (2018).